The Structure of Particle Gels as Studied with Confocal Microscopy and Computer Simulations

Martin T. A. Bos

Promotoren: dr. B. H. Bijsterbosch
emeritus hoogleraar in de fysische- en kolloïdchemie

dr. ir. P. Walstra
emeritus hoogleraar in de zuivelkunde

Co-promotor: dr. J. H. J. van Opheusden
universitair docent bij het departement voor
agro-, milieu- en systeemtechnologie.

Martin T. A. Bos

The Structure of Particle Gels as Studied with Confocal Microscopy and Computer Simulations

Proefschrift
ter verkrijging van de graad van doctor
op gezag van de rector magnificus
van de Landbouwuniversiteit Wageningen,
dr. C. M. Karssen,
in het openbaar te verdedigen
op vrijdag 5 september 1997
des namiddags om half twee in de Aula.

Stellingen

behorende bij het proefschrift
"The Structure of Particle Gels as Studied with Confocal Microscopy and Computer Simulations"
M. T. A. Bos

1. Met het aannemen van DLCA-modellen als de standaard voor colloïdale aggregatie wordt aan het doel van zulke modellen totaal voorbijgegaan.
   dit proefschrift, Hoofdstuk 2

2. Een fractale struktuurbeschrijving van deeltjesgelen is onvolledig indien men in de beschrijving volstaat met de fractale dimensionaliteit.
   dit proefschrift, Hoofdstuk 4 en 5

3. Zelfs als eigenschappen van een deeltjesgel zich niet louter met de fractale dimensionaliteit laten beschrijven kan een fractale struktuurbeschrijving nog steeds waarde hebben.
   dit proefschrift, Hoofdstuk 4 en 5

4. Verdichting kan gepaard gaan met een afname van de fractale dimensionaliteit.
   dit proefschrift, Hoofdstuk 5

5. Gelering bij hoge volumefractie ($\phi > 0.2$) kan gepaard gaan met gaten van vele malen de deeltjesgrootte zolang er voldoende reorganisatie optreedt.
   B.H. Bijsterbosch, M.T.A. Bos, E. Dickinson, J.H.J. van Opheusden, P. Walstra, Faraday Discuss. ***101*** *51-64, 1995*

6. Het DLCA-model geeft hoogstens argumenten dat aggregatie uiteindelijk leidt tot een gepercoleerd netwerk; spinodale ontmenging geeft hoogstens argumenten dat aggregatie uiteindelijk leidt tot verdichting. Een deeltjesgel is het resultaat van deze tegenstrijdige argumenten.
   dit proefschrift, Hoofdstuk 2

7. Deeltjesgelen zoals gesimuleerd met Brownse Dynamica geven anomale, ofwel stijgende multifractale spectra. Dit resultaat is geen gevolg van een programmeerfout en toont aan dat de theorie die beweert dat multifractale spectra altijd dalend zijn, onjuist is.
   J.H.J. van Opheusden, M.T.A. Bos, G. van der Kaaden, Physica A 227 183-196, 1996

8. Voor het bereiken van een zo hoog mogelijke resolutie in scanning-microscopie zijn opnamecapaciteit en signaal-ruisverhouding doorslaggevend, niet de golflengte van het licht of de apertuur van het objectief.
   dit proefschrift, Hoofdstuk 3

9. De veronderstelling dat elke goede jurist de wet van buiten kent is equivalent aan de veronderstelling dat elke goede chemicus het "CRC Handbook of Chemistry and Physics" moeiteloos opdreunt.

10. Straatmuzikanten spelen veelal muziek uit de zestiger jaren omdat er aan publiek dat deze tijd bewust heeft meegemaakt het meeste te verdienen valt.

11. Het opstaan tijdens applaus bij concert- en theaterbezoek is geen blijk van erkenning dat het een uitzonderlijk mooie uitvoering was, maar van de wens zich niet door anderen het uitzicht te laten benemen.

12. In veel industrieel onderzoek loopt empirie vooruit op inzicht; het feit dat empirisch onderzoek beter te plannen is, speelt daarin een belangrijke rol.

13. Omdat het wettelijk niet is toegestaan om een octrooi naderhand te generaliseren, zal het door de werkgever verstrekken van een bonus per toegekend octrooi een inefficiënte strategie blijken.

Contents

1. General Introduction

1.1 Gels

Gels are perhaps best introduced by probing them with one's own hands; simple hair setting gel will serve as an excellent study material for this. The way a gel reacts to manual or mechanical probing shows that it is neither completely liquid (but can nevertheless flow), nor completely solid (but is nevertheless elastic up to a certain yield stress). Indeed, the rheological definition of a gel is straightforward: it is a material that exhibits a yield stress, viscoelastic properties and has a moderate modulus (*i.e.* $< 10^6$ Pa)[1].

The practical importance of materials that are neither liquid nor solid can be seen from its use in foods. Here it can be very desirable to exploit both liquid-like and solid-like properties in one single product. Jelly, for instance, which is a sweet dessert made from sweetened water and pectin, gives the consumer an impression of eating something substantial even though it consists for more than 95% by weight of water. Unlike water, it can be cut into slices and chewed; yet one need not apply much pressure before it yields, hence it can be swallowed easily.

The reason for the peculiar rheology of gels lies in their structure. Gels consist of interconnected material, *i.e.* a network of material, dispersed in a fluid. Elasticity of the material causes elasticity of the gel as a whole. The network consists of cross-linked subunits, which can be torn apart by applying a large enough strain. Above a certain stress applied to the gel, disruption of cross-links will destroy the network, causing the gel to flow. In the case of jelly, the subunits are polymeric pectin molecules, which become cross-linked upon cooling by the formation of microcrystalline regions. Because the network is made from cross-linked polymers, jelly is called a polymer gel. Polymer molecules in a good solvent can have a very large spatial extent, *i.e.* the size of a dissolved molecule can exceed the size of a crystalline molecule by one order of magnitude or more. For this reason, the formation of a network, and therefore a gel, is possible even when very little dry material is used. Many food gels are made from polymeric material in a similar way as jelly. Examples of food polymer gels are agar gels (used in setting soup) and gelatin gels (used in puddings).

1.2 Particle gels

As described above, an essential element of gel structure is a network consisting of cross-linked subunits. In particle gels these subunits are particles, cross-linked through interparticle bonds. An example of a particle gel is fat, which can be obtained by cooling a mixture of triglyceride oils. Fat essentially consists of a network of triglyceride crystals dispersed in liquid triglyceride oil. Sintering of adjacent crystals gives the network its strength, with leads to fat plasticity. Another important example of a particle gel is a milk or caseinate gel. Milk contains casein micelles, which are spherical particles of about 120 nm average diameter, sterically stabilised by κ-casein molecules. When rennet is added to milk, a proteolytic enzyme removes the stabilising layer, causing the casein micelles to aggregate, *i.e.* stick and form clusters. The result of this, shown in Figure 1.1, is a network of cross-linked strands.

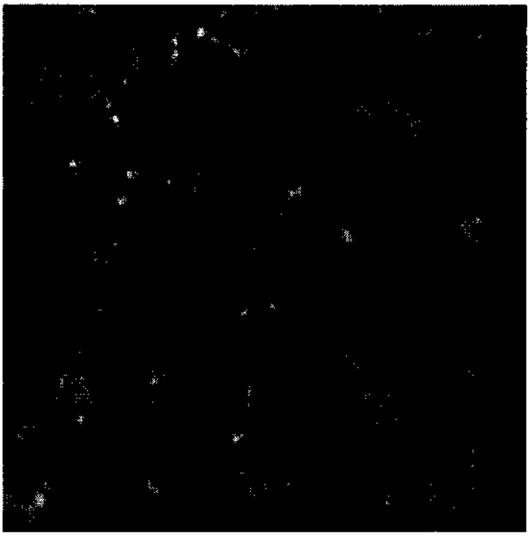

Figure 1.1: Micrograph of a casein gel; 42 by 42 μm.

The facts that both the casein micelles and the cross-links between them are deformable, and that bonds between casein particles can be broken, lead to viscoelasticity and a finite yield stress, *i.e.* gel-like behaviour.

1.3 Aggregation and gelation

In a stable colloidal suspension, the effective interaction between particles is repulsive, so there will be neither cross-links between particles nor a connected network. Upon destabilisation, particles will start to form bonds, but this will not always lead to the formation of a particle gel. Instead of a gel, aggregation often produces a compact structure which either creams or precipitates. To answer the question "will an aggregating suspension of particles form a particle gel or not; and if so, what will be the gel structure?", we need to understand the aggregation process and the cross-linking of particles to form a connected network. Because the aggregation is a non-equilibrium process, it can be appreciated that this is a difficult problem.

The introduction of fractal aggregation models[2, 3]. has given research on particle gelation a formidable impulse. It has been recognised by Bremer[4] that these aggregation models must eventually result in a connected network of particles, *i.e.* a gel, regardless of particle volume fraction or interaction details. This has led to *fractal scaling laws*, which have proven quite useful in explaining properties of gels, like viscoelasticity.

In this study we will use the understanding as presented in Bremer's thesis to revisit the question mentioned above. This discussion is initiated in Chapter 2, which may be regarded as the scientific introduction to this thesis. In Chapter 2 we attempt to form a connection between equilibrium thermodynamics and fractal aggregation models. We will use two techniques: microscopy to study the structure of particle gels, and computer simulation to investigate particle gelation models. Both techniques are used to visualise particle gels and to quantify their structure. The type of microscopy is confocal scanning microscopy, which is especially suited for a three dimensional study. Computer simulations are used as a tool for identifying aggregation mechanisms; here the visualisation in itself is straightforward.

In terms of practical relevance, the structure of a particle gel translates into porosity and into viscoelastic properties of the gel. A clearer connection between aggregation models and gel structure will contribute to more control over products, from which many applications, most notably foods, can benefit.

1.4. Contents of this thesis

Chapter 2 of this thesis introduces aggregation and gelation of particles as well as fractal aggregation models. Chapters 3 and 4 introduce and apply confocal scanning microscopy as a tool for studying the structure of particle gels made from three different model colloids. In Chapters 5 and 6 Brownian Dynamics Simulations are used as a tool for forming a better connection between aggregation and gel structure. Finally, chapter 7 summarises and generalises the conclusions of all previous chapters.

Literature

[1] P. Walstra, in *Food Chemistry*, edited by O. R. Fennema (Marcel Dekker, Inc, New York, 1996), p. 95.

[2] F. Family and D. P. Landau, *Kinetics of aggregation and gelation* (North-Holland, Amsterdam, 1984).

[3] T. Vicsek, *Fractal growth phenomena* (World Scientific, Singapore, 1992).

[4] L. G. B. Bremer, (Wageningen Agricultural University, The Netherlands, 1992).

2. Theory of aggregation and gelation

2.1 Aggregation and phase separation

2.1.1 Introduction

Monodisperse colloidal suspensions can be regarded as idealised models for molecular systems. Depending on their interactions they can undergo phase transitions like the gas-liquid transition[1], or they can crystallize[2]. To be more precise, for colloidal systems one can find phase diagrams which, similar to phase diagrams for molecular systems, describe their thermodynamic state as a function of density (or volume fraction) and temperature. Although it is difficult to condense all colloidal interactions into a single parameter named "temperature", this has in some cases shown to be possible[3,4]. An example of a part of the phase diagram of a simple molecular substance is given in figure 2.1, using arbitrary units for both the temperature T, and the volume fraction φ (or rather the density ρ).

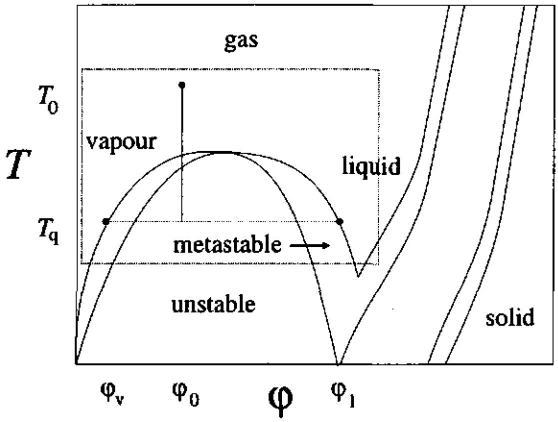

Figure 2.1: Equilibrium phase diagram.

In figure 2.1, we concentrate on the liquid-vapour coexistence region, because it suffices to explain the salient behaviour. The curves shown are boundaries between the stable and the unstable regions, the outer one is the binodal, the inner one the spinodal curve. Above the binodal we have a stable fluid phase. Upon cooling a system of a certain volume fraction, the metastable or unstable region is reached. In the metastable region, the system may stay in a homogeneous supersaturated vapour state for a relatively long time, until it nucleates into liquid droplets dispersed in a gaseous surrounding. If we cool rapidly enough to move below the spinodal curve the unstable region is reached, and phase separation starts spontaneously, as the formation of dense droplets is not hindered by a free energy barrier. The minimum free energy state of the system at volume fraction φ_0 quenched at a low temperature T_q will be a macroscopic phase separation of two states: a liquid state at volume fraction φ_l in thermodynamic equilibrium with its vapour of volume fraction φ_v. This is indicated by the horizontal dashed line in the figure. During phase separation, particles within dense regions of volume fraction φ_l are nearer to each other than before, and can therefore aggregate easily.

For a colloidal suspension we can also use the phase diagram as a guideline for aggregation. It is important to realise, however, that the equilibrium phase diagram does not tell us how, nor in how much time this minimum in the free energy will be achieved. Microscopically, condensation must be achieved by aggregation of molecules or particles. Especially in the case of colloidal suspensions, where the dynamics of particles are governed by irregular Brownian motion and short-ranged interparticle forces, we can expect the condensation to be a non-trivial dynamic process. If φ_0 is much smaller than φ_l, particles must travel large distances before "liquid droplets" can be formed.

2.1.2 Aggregation: microscopic dynamics

A system which is thermodynamically unstable will tend to show growing spatial density fluctuations[5]. For an unstable colloidal system with attractive interactions, particles will move into interaction range due to inertial or Brownian motion, and form clusters connected through bonds. Both the bonding and the unbonding probabilities depend on the particle interactions and volume fraction. During the aggregation process, the distribution of cluster sizes will gradually shift towards larger clusters.

A problem in reaching the global minimum in the free energy is that the growth of clusters through diffusion tends to produce tenuous structures. Indeed, if the bonding is irreversible, models exist predicting that growing clusters are fractals, *i.e.* the clusters become ever more tenuous as they grow. Therefore the way by which clusters grow locally opposes the global tendency to form compact zones of volume fraction φ_l. This means that the global minimum in free energy will not be reached unless tenuous clusters reorganise to form more bonds and hence more compact clusters. Note that for strictly irreversible bonding the inherent history dependence of the aggregation process prevents description of the system in terms of thermodynamics, and the concept of a phase diagram becomes quite useless. We will in the second part of this chapter describe how one can treat such systems.

2.1.3 Cluster reorganisation

Strong bonds clearly obstruct reorganisation of tenuous (*i.e.* open) clusters. Even though the system can gain energy by the formation of more bonds, the breaking of bonds can require a greater activation energy than the system will be able to produce within reasonable time. For condensation of argon, the interactions between the atoms are reversible enough to allow for enough cluster reorganisation. For many colloidal systems, however, bond formation leads to the forming of strong cohesive or even covalent bonds. With the breaking of these bonds, large amounts of energy are involved. Only external forces like gravity or shear can continuously provide the system with this energy. If such forces are not present, the system will attain a frozen-in non-equilibrium structure that changes only very slowly.

2.1.4 Particle gels

In colloidal systems where, upon destabilisation, bond formation is irreversible and external forces are absent, particle gels are formed. The structure of such particle gels is a space-spanning network made of cross-linked tenuous clusters. In this network, which itself can be thought of as a single percolating cluster, the identity of the earlier clusters is lost. The scenario described above leading to a frozen-in non-equilibrium structure may very well be the way by which these gels are formed: a logical consequence of aggregation irreversibly obstructed by the formation of tenuous clusters. This is a possible basis for a thermodynamical understanding of particle gelation.

To understand the formation of a frozen-in non-equilibrium structure we need to know more about the geometry of clusters. The geometry of larger clusters has been succesfully described using fractal models. The following section will explain these models.

2.2 Fractal geometry of clusters

2.2.1 Fractal objects

We give an example of a fractal object in figure 2.2.

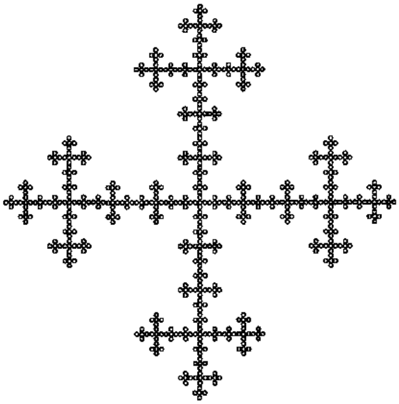

Figure 2.2: Fractal object.

The object in figure 2.2 is called a deterministic fractal object, because it is generated following a well-defined iterative algorithm. This algorithm is shown in figure 2.3:

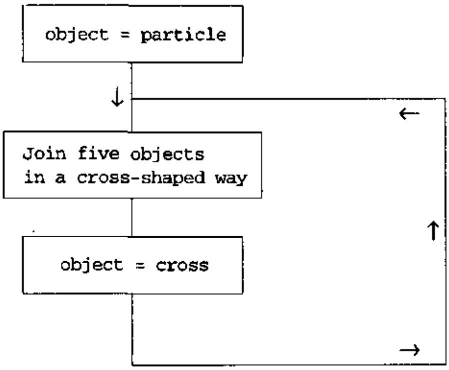

Figure 2.3. Fractal algorithm.

Evidently, an object generated by following this algorithm for a number of iterations has a self-similar structure. We can now study the number of particles N in the object as a function of the object dimensionless size L (expressed as the number of particles along the main axes of the cross). We find that for the j-th iteration:

$$\left.\begin{array}{l} L = 3^j \\ N = 5^j \end{array}\right\} \Rightarrow N = L^{[\ln(5)/\ln(3)]} = L^{d_\mathrm{f}} \tag{1}$$

Equation (1) predicts universal scaling regardless of j . The constant scaling exponent d_f (value ≈ 1.465) is a fingerprint of the type of recurrence present in the algorithm in figure 2.3. For close-packed objects built from particles, N scales as L to the power 2 (in two dimensions) or 3 (in three dimensions). The object in figure 2.2 has a non-integer scaling exponent, which is for this reason called the fractal dimensionality.The object itself is called a fractal.

For the object in figure 2.2 we can define a dimensionless particle number density ρ_p :

$$\rho_\mathrm{p} \equiv \frac{N}{L^2} = L^{d_\mathrm{f}-2} \tag{2}$$

Because d_f is smaller than 2, ρ_p decreases as a function of L, which can also be seen in figure 2.2. Generally we can say that the larger the size of a fractal object, the more tenuous it is, provided the fractal dimensionality is less than the number of dimensions the object is embedded in.

Many iterative algorithms like figure 2.3 have been proposed to construct deterministic fractal objects; the related fractal dimensionalities are either calculated as in (1), or measured as the slope of a double logarithmic plot of N versus L. Iterative algorithms can also introduce randomness, when, for instance, the joining depends on a random number. In this case the object is called a stochastic fractal.

2.2.2 Diffusion limited aggregation

A special iterative algorithm that is of interest to aggregation phenomena is the Diffusion Limited Aggregation[6] (DLA) algorithm, which is given in figure 2.4:

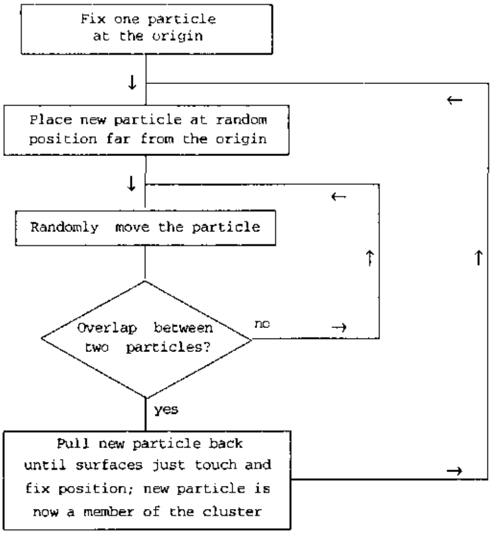

Figure 2.4. DLA-algorithm.

A lattice version of the DLA-algorithm has been implemented on a computer to generate clusters of more than 10^6 particles. An example of such a DLA-cluster in two dimensions is given in figure 2.5.

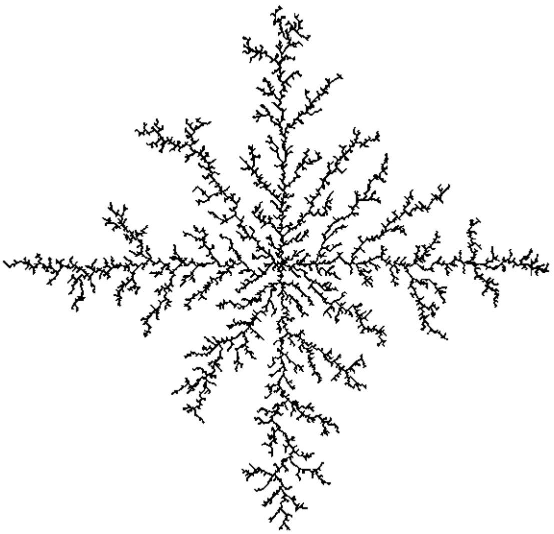

Figure 2.5: DLA-cluster, generated on a square lattice.

Analysis has shown[6] that DLA-clusters are stochastic fractal objects with a fractal dimensionality of 1.7 in two dimensions and 2.4 in three dimensions. The fact that the very tenuous cluster shown in Figure 2.5 can be quite well defined using a fractal model is encouraging. The question which arises is: can colloidal aggregation be modelled with algorithms comparable to DLA with a corresponding fractal dimensionality?

2.2.3 Diffusion limited cluster aggregation

For modelling colloidal aggregation, the DLA-algorithm is unrealistic because of the notion of a seed particle and the sequential addition of new particles. A more realistic algorithm was introduced by Meakin and Kolb in 1983[7,8]. This algorithm, depicted in figure 2.6, is called Diffusion Limited Cluster Aggregation (DLCA).

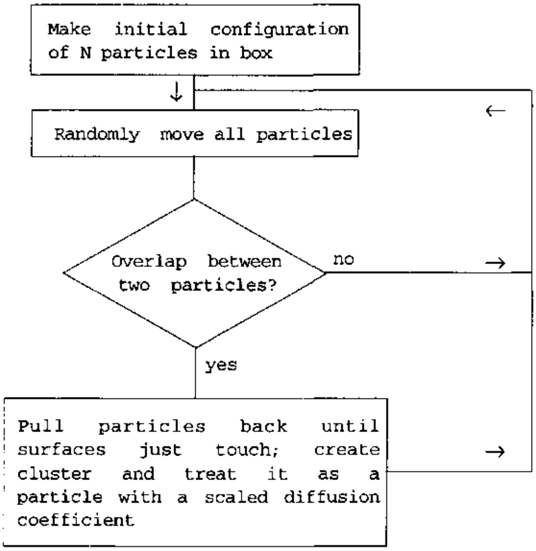

Figure 2.6: DLCA-algorithm.

Simulation results show that the DLCA-algorithm yields clusters which are fractal objects, with a fractal dimensionality of 1.4 in two dimensions and 1.8 in three dimensions.

An important aspect of the DLCA-algorithm is the treatment of clusters as scaled particles, with a scaled diffusion coefficient. The cluster diffusion coefficient D_c is calculated by using a scaling law:

$$D_c \propto N^{\nu} \tag{3}$$

with $0 < \nu < 1$. It was found[6] that the fractal dimensionality does not depend on the diffusion scaling exponent ν. This suggests that the results of the DLCA-algorithm are insensitive to aggregation details, and that therefore the DLCA-dimensionality can be regarded a universal physical constant. Assuming this to be the case, it is expected that for an aggregating colloid the DLCA-algorithm is generic enough to predict the fractal structure of clusters, and that discrepancies between theory and experiment do not really change the fractal properties. In other words, the same universality observed in DLCA-calculations is also expected for an aggregating colloid.

The DLCA-algorithm has become widely used as a model for colloidal aggregation. It has been used in particular by Walstra[9], Bremer[10,11] and Rouw[3] as a model for particle gelation. Bremer has recognised that DLCA must eventually lead to the formation of one very large cluster containing all the particles in the system. This can be understood as follows. For a growing DLCA-cluster, Equation (2) holds, only there is a lower bound to ρ_p. This bound is determined by the number density for the whole system ρ_o. When all DLCA-clusters have a ρ_p equal to ρ_o, the volume of the system is completely filled with clusters. When then ρ_p for clusters has to become less than ρ_o, clusters must overlap. The DLCA-algorithm only allows for a limited degree of interpenetration of clusters: when two interpenetrating clusters overlap, they simply form a bond to become a new cluster. Summarising, DLCA-clusters grow individually until their ρ_p becomes ρ_o, after which they all connect to one cluster containing all particles. This one cluster is not a fractal object; it is a close packing of many fractal sub-clusters with (average) size L given by (2) with ρ_o substituted for ρ_p. According to this model, there will not be a nonzero number density for which gelation becomes impossible: L simply increases as ρ_o decreases.

The DLCA algorithm provides a suitable and simple model to describe the early stages of particle aggregation and consecutive gelation. It leads to an open, fractal structure with a fractal dimensionality that should be in the range of 1.7 to 1.9 approximately. Slightly different values can also be found, depending on the initial volume fraction. After all DLCA is a model for which only in the limit of large cluster size and dilute initial systems the standard type of fractal scaling is found. Small clusters or overlapping clusters close to gelation can and probably will yield different values. On the other hand the occurrence of a fractal structure with a dimensionality in the right ball-park does not imply that the particles have aggregated according to a mechanism similar to DLCA. Other mechanisms (e.g. spinodal decomposition) and hence other models may also yield such structures. The main point we want to stress is that one needs specific dynamical models to describe the early stages of the phase separation process of the thermodynamically unstable suspension, and we simply use DLCA as an example of such a model for the discussion, but one has to keep an open mind for other models by which colloidal aggregation can be modelled.

2.2.4 Scaling in diffusion-limited clusteraggregation

The aim of this study is to determine, describe and understand the formation and the structure of particle gels. The DLCA-model helps us to understand the formation of a particle gel consisting of tenuous fractal clusters. For clusters of various size and mass we expect, analogous to (1), the following scaling:

$$n(r) = n_0 \cdot \left(\frac{r}{a}\right)^{d_f} \tag{4}$$

In Equation (4) n is the number of particles contained in a cluster of radius r. The radius of the particles is a, n_0 is a dimensionless proportionality constant (generally of order unity - the actual value of n_0 depends on the definition of r used) and d_f the fractal dimensionality. Equation (4) can be used to describe clusters produced by any aggregation mechanism; its use is by no means limited to the DLCA-algorithm. For spherical, close packed clusters d_f equals 3 and n_0 equals φ_{cp}, the volume fraction of close packing.

For spherical objects the choice of r may be obvious, for anisometric clusters various definitions of the radius can be used, and the choice is reflected in the value of n_0. If we take for instance a needle-shaped cluster ($d_f = 1$) consisting of one row of particles, and define r as its gyration radius, then n_0 equals $\sqrt{12}$. If we define r simply half its length, then n_0 equals 1/2. For the fractal of figure 2.2, using $L/2$ for r, n_0 equals 1/2. The value of n_0 is very important in understanding measured data on cluster sizes; we will address this point later.

The scaling relation as defined in equation (4) is valid for a set of clusters of various size and mass. If one can measure these quantities for a large number of clusters a simple log-log fit of the data will directly yield the parameters as defined. In practice these figures are hard to obtain; apart from computer simulations it is generally impossible. Moreover in the gelled system one studies a single cluster only, in which, although it is built of fractal subclusters, the identity of these clusters has been lost. The point now is that one may determine the fractal properties of a cluster alternatively by a version of the so-called sandbox method[12]. In this method one considers the number of particles $n(r)$ in a sphere of radius r around any particle of the cluster. Simple linear regression on $\log(n)$ versus $\log(r)$ yields the parameters one seeks. Particles near tips in relatively void regions will have low values of n_0, while particles in dense parts of the cluster can give values up to the close packing limit. By pre-averaging of the $n(r)$ over all particles one finds average values for the fit parameters. In fact this averaging process amounts to calculating the scaling of integrated pair correlation function. Later we will directly use the scaling of the pair correlation function, which in many cases can relatively easily be determined experimentally, to find the fractal dimensionality of real gels. (Note that in some versions of the sandbox method one takes the centre of mass of the cluster as the origin for calculating $n(r)$. Though this may yield values for the dimensionality and the intercept by fitting to a linear regime, these values depend strongly on the specific shape of the cluster. Moreover they cannot directly be related to the scaling of the pair correlation function.) For the computer simulations we will use the sandbox method to determine the momentaneous structure of the developing system. Now assume we have a system which is aggregating into clusters that scale exactly as equation (4), with $n_0 = 0.4$ and $d_f = 1.8$ according to the DLCA model we have defined before.

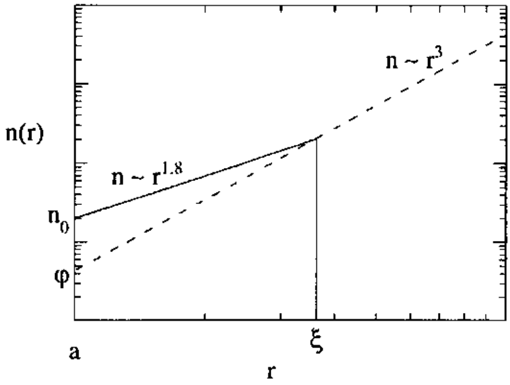

Figure 2.7: Fractal scaling in DLCA

In our fractal aggregation model (FAM) at a certain time t during the aggregation process the function $n(r)$ calculated according to the sandbox method for a destabilised system at volume fraction φ is given in figure 2.7. For low values of r we see a fractal regime which ends at the size of the average cluster in the system (we have neglected effects of monomers, which have zero close neighbours and hence suppress n_0). At high values of r we have the homogenous regime, where the number of neighbouring particles simply scales with the volume of the surrounding sphere, the prefactor then becomes the volume fraction.

$$n(r) = \varphi \cdot \left(\frac{r}{a}\right)^3 \tag{5}$$

In between these two regimes there will be a cross-over, which depends on the details of the diffusion and aggregation process; this cross-over is omitted from figure 2.7 for the sake of simplicity. If all clusters have equal size, and are equally spaced, there would be a horizontal line in the cross-over regime. In a more random system, with clusters of various sizes and shape, the cross-over would be more gradual. Because of the finite time the homogeneous regime is always reached at some finite r.

When the clusters grow further, the value of r/a at which the fractal regime crosses over to the homogenous regime increases, but that growth is limited. Once the average volume fraction inside the clusters reaches that of the overall system, the individual clusters cannot grow further. They start overlapping, and form a gel. When the fractal regime reaches the homogeneous regime this situation happens. If the fractal regime extends all the way to the homogeneous regime, the cross-over regime is reduced to the intersection point of the two lines (as it is drawn in figure 2.7). This point, or rather the radius corresponding to it, is called the correlation length ξ of the gel. It is an indication of the average size of the aggregates close to gelation. In actual or simulated systems gelation will occur at a somewhat earlier stage, and there will be a finite cross-over regime left. Nevertheless the correlation length can be defined for such systems by linear extrapolation of the fractal and homogeneous scaling regime to the intersection point.

The above is an illustrative exercise to investigate the scaling of a system aggregating as described. In reality diffusion and detailed interaction effects will play a role in, for instance, the scaling in the cross-over regime. Another difference with DLCA is that the bond between two particles of different clusters that unites them into a single one in general is not as rigid as assumed in figure 2.6, nor need the bonding process be so irreversible. Bond reversibility and flexibility are two phenomena by means of which the system can further diminish its free energy. We will now look into these in some more detail.

2.2.5 Aggregation and reorganisation

The aggregation as given by DLA and DLCA-algorithms is purely irreversible. Once two particles have formed a bond, this bond is permanent. This means that when small clusters aggregate to form a larger cluster, the (fractal) geometry of the smaller clusters is maintained. We have seen earlier that irreversibility can hinder phase separation of thermodynamically unstable systems (section 2.1.3). On the other hand the DLCA model, which is based on strictly irreversible reactions, will not apply exactly if there is even a small amount of reversibility, and other types of structure will be the result.

The effect of reversibility on the geometry of clusters has been tested in a number of computer simulations that are derived from the DLCA-algorithm. It has been shown[13-15] that reversible bonding results in a fractal dimensionality larger than the DLCA-dimensionality, and increasing with time. The reverse is found in a simulation where DLCA-aggregates are reformed and compactified after they are formed[16]: here a decreasing d_f is found. A different approach is a modified DLCA-type scheme, in which upon collision a bond is formed with probability p. It is found that when p is taken very small, the clusters are still fractal objects with $d_f = 2.1$ independent of the diffusion scaling exponent or time. This limit is called Reaction Limited Cluster Aggregation (RLCA). For larger p, d_f remains equal to the DLCA-dimensionality. It should be noted that once a bond is formed in RLCA, it will never break.

It appears that if the DLCA-algorithm is complicated by introducing reversibility or reorganisation, universal fractal scaling with a constant d_f does not hold anymore. In the literature, the effects of reversibility or reorganisation on the value of d_f are not yet fully understood. Furthermore, in studying this non-universal scaling the attention is focused on the value of d_f, whereas the value of n_0, which forms the connection between scaling and absolute values, is often assumed to be merely an unimportant constant of order unity. When universal fractal scaling does not hold, this need not be the case.

Let us have a closer look of the effect of reorganisation on our fractal aggregation model. The introduction of a different phenomenon also introduces a different time scale. It now becomes necessary to specify which is the faster process. We consider the case where the binding takes place irreversibly but the bonds formed are highly flexible. For low volume fraction this means that trimers after formation will reorganise into compact triangles before they bind to a different cluster. Thus compact small clusters are formed. At some point the flexibility of the single bond will not allow for a full reorganisation into a compact object, for instance the formation of multiple bonds between two compact clusters may stop the process. At that point we regain a FAM, but now with much larger objects. If we wait until the system has gelled, the sandbox plot will look like figure 2.8.

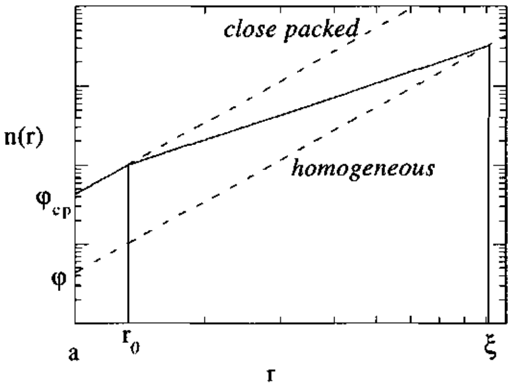

Figure 2.8: Bounds in DLCA.

In figure 2.8 there are three regimes, one compact homogenous regime at small r at volume fraction φ_{cp}, a fractal scaling regime starting at the size r_0 of the average compact cluster from which the gel is build and ending at the (now much larger) correlation length, and a homogeneous random regime with volume fraction φ at high r. Again in real systems and simulations all cross-overs will be gradual, both in the regimes found and in the aggregation and reorganisation mechanism. Important is that at short range, due to the bond flexibility, the system adapts to the dense phase one would expect to find from thermodynamic arguments.

Instead of making specific assumptions on the values of d_f and n_0, it is also possible to simply measure both parameters from a fit of the fractal scaling region in $n(r)$; figures 2.7 and 2.8 illustrate how this should be done. In the above we have introduced the parameter r_0; clearly, for a reorganising system r_0 can become more than just one particle radius. We can determine r_0 from d_f and n_0 following the construction of figure 2.8:

$$r_0 = a \cdot \left(\frac{n_0}{\varphi_{cp}} \right)^{1/(3-d_f)} \tag{6}$$

An alternative formulation of the scaling relation (4) now becomes:

$$n(r) = \varphi_{cp} \left(\frac{r_0}{a} \right)^3 \left(\frac{r}{r_0} \right)^{d_f} \tag{7}$$

Especially for reversible or reorganising systems, r_0 will be an interesting parameter to study. If the system shows substantial compactification due to some reorganisation process, we may expect values of r_0 larger than the primary particle radius a.

2.3 Conclusions

For the modelling of aggregation and gelation of colloidal particles, we have seen two approaches: one based on thermodynamics and one on DLCA. The former is appropriate for reversible aggregation, the latter for irreversible aggregation. For all types of colloidal aggregation which are in between these two extremes, an understanding based on both approaches is needed.

For the modelling of particle gelation we have chosen DLCA as a starting point. Simultaneously we can regard the gelling system as an unstable colloid with two separated phases as a minimum in free energy. It is clear that if the clusters contain some internal flexibility, the well-defined tenuous cluster geometry of DLCA will not remain intact. By compactification at small length scales the system has the opportunity to increase r_0, but this increase is strongly constrained by the connectedness of the clusters.

When a gel is formed we expect that aspects of the equilibrium phase diagram can still be found up to a length r_0. Considering a gel as a frozen non-equilibrium state, the increase of r_0 can still go on after gelation, depending on flexibility and reversibility of bonds. Therefore by a complicated pathway, the equilibrium state may be reached after all.

The points mentioned is this chapter form the basis by which we will study and interpret structural data on particle gels.

Literature

[1] M. H. G. M. Penders, Ph.D. Thesis, University of Utrecht, The Netherlands, 1991.

[2] C. Smits, Ph.D. Thesis, University of Utrecht, The Netherlands, 1991.

[3] P. W. Rouw, Ph.D. Thesis, University of Utrecht , The Netherlands, 1988.

[4] P. W. Rouw and C. G. de Kruif, *Phys. Rev. A* **39,** 5399 (1989).

[5] J. W. Cahn, *J. Chem. Phys.* **42,** 93 (1965).

[6] T. Vicsek, *Fractal growth phenomena*, second ed. (World Scientific, Singapore, 1992).

[7] M. Kolb, R. Botet, and R. Jullien, *Phys. Rev. Lett.* **51,** 1123 (1983).

[8] P. Meakin, *Phys. Rev. Lett.* **51,** 1119 (1983).

[9] P. Walstra, H. J. M. v. Dijk, and T. J. Geurts, *Neth. Milk Dairy J.* **39,** 209 (1985).

[10] L. G. B. Bremer, Ph.D. Thesis, Wageningen Agricultural University, The Netherlands, 1992.

[11] L. G. B. Bremer, B. H. Bijsterbosch, P. Walstra, and T. van Vliet, *Adv. Coll. Interf. Sci.* **46,** 117 (1993).

[12] S. Haw, *Physica A* **208,** 8 (1994).

[13] M. Kolb, *J. Phys. A: Math. Gen.* **19,** L263 (1986).

[14] W. Y. Shih, I. A. Aksay, and R. Kikuchi, *Phys. Rev. A* **36,** 5015 (1987).

[15] A. H. L. West, J. R. Melrose, and R. C. Ball, *Phys. Rev. E* **49,** 4237 (1994).

[16] H. F. van Garderen, W. H. Dokter, T. P. M. Beelen, R. A. van Santen, E. Pantos, M. A. J. Michels, and P. A. J. Hilbers, *J. Chem. Phys.* **102,** 480 (1995).

3. Theory of confocal scanning microscopy

3.1 Confocal microscopy

3.1.1 Introduction

The use of microscopy is limited by its resolving power. In colloid chemistry, where one mostly works with particles of sub-micron size, electron microscopy is widely used. Electron micrographs are used quantitatively, for instance, in the case of particle sizing, and qualitatively in many other cases. An important drawback of electron microscopy is that only solid samples can be studied. For colloids this implies that the continuous phase must either be evaporated or frozen. Both are rigorous treatments, and the resulting micrographs may not be fully representative of the structure before treatment. Light microscopy can be used to study colloids under more gentle conditions. The resolution however, limited by the wavelength of the light and the aperture of the optical system, is much less than in electron microscopy. Both light and electron microscopy often yield transmission micrographs, which are projections: the axial (*i.e.* perpendicular to the plane of view) position of the visible objects is unknown.

In this study confocal scanning light microscopy is used, a technique that allows liquid samples to be studied without rigorous sample preparation. The greatest advantage of confocal scanning microscopy is that it enables three-dimensional reconstruction from a series of two-dimensional micrographs. The success of this reconstruction depends on the resolution of the microscope. In this chapter we will give a short description of confocal scanning microscopy, including relevant operational parameters, after which we will derive a quantitative relation describing image formation and resolution using three dimensional point spread functions. Finally, we will describe methods based upon Fourier Transformation that can be used to enhance the resolution, especially the axial resolution, of a confocal microscope, without amplifying noise. In the next chapter we will apply the method described here to various samples of particle gels.

3.1.2 Experimental setup

Confocal microscopy uses laser light as a source. Most common is fluorescence confocal scanning microscopy, where the sample is labelled with a fluorochrome and the emitted light is detected. A laser beam is pointed at a very small aperture, the source pinhole, which in good approximation constitutes a point source. A lens focuses it on a point F in the sample. This lens is aligned in such a way that the image of F, F', coincides with another aperture (hence the name confocal), the detector pinhole, where a photomultiplier tube measures the intensity. The setup is illustrated in Figure 3.1.

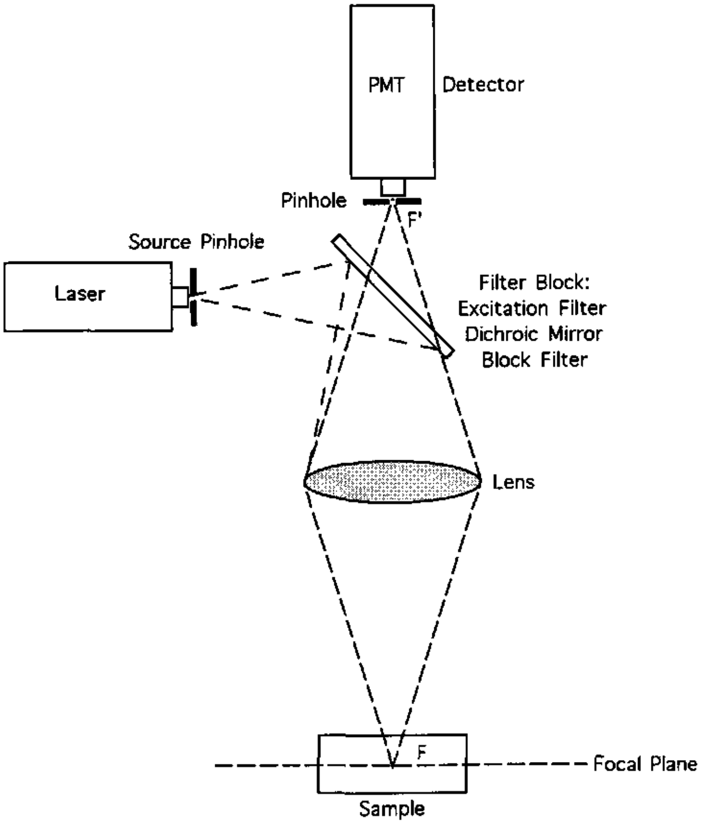

Figure 3.1: Schematic picture of a confocal microscope.

The effect of this alignment is that the light emitted from any other position than F is not focused on the detector pinhole, and will reach the photomultiplier tube with considerable less intensity. To ensure that only the light emitted by the fluorochrome reaches the detector pinhole, a filter block is used, which contains a dichroic mirror and two block filters. The dichroic mirror is used as a beam-splitter; in combination with the filters it reflects the light with excitation wavelength λ_{ex} from the source pinhole onto the lens and into the sample, but transmits the emitted light with wavelength

λ_{em}. For common fluorochromes like rhodamine B and fluorescein, ready-to-use filter blocks can be plugged into the microscope.

A confocal micrograph can be obtained by moving either the object or the laser beam, thus producing a scanning micrograph. In most confocal microscopes, including the one used in this study, the laser beam scans the plane of view at a fixed axial position using scanning mirrors; one scan can be considered an optical section. Scans are stored on a computer as a digitized matrix of intensities; one element of this matrix is called a picture element or pixel. By recording scans at various depths in the sample, the three-dimensional structure of the sample can be imaged. Confocal microscopy as described here is generally referred to as CSLM (confocal scanning laser microscopy), although LSCM is also used in the literature.

3.1.3 Microscope parameters

Parameters that are important for the resolution are the wavelengths λ_{ex} and λ_{em}, the magnifying power and the numerical aperture (NA) of the lens. Also important is the pixel size, as this sets a lower limit to the resolution. The pixel size is determined by the scanned area and the number of pixels used for storage.

Other parameters are: pinhole sizes, illumination intensity and photomultiplier tube settings. We assume the detector pinhole small enough to be approximated by a point. The size of the detector pinhole can be increased to obtain a stronger signal, but the integration over the pinhole area would very much complicate the relation between the signal measured at the detector and the intensities in the sample. In the case of a weak signal, the illumination intensity can be increased, at the risk of photobleaching of the fluorochrome. In digitization of the matrix of intensities, only a limited number of levels are used (normally 256). The photomultiplier tube settings (*i.e.* baseline signal and amplification) are adjusted in such a way that all available levels are used as efficiently as possible.

3.2 Image formation in confocal scanning microscopy

3.2.1 Introduction

Small objects can be imaged under a microscope regardless of their size. An object much smaller than the wavelength used would still give rise to a spot on a micrograph, only the size of this spot is no longer a correct measure of the size of the particle. As it appears, the particle becomes smeared over an area which can be considerably larger than its size. The distance of smearing is a measure of the resolving power of the microscope: a microscope with high resolving power smears a small object only over a small distance, so that two objects close together can still be recognized as distinct objects. When lenses are used, the resolving power depends strongly on the numerical aperture.

The aim of this section is to find a quantitative description of smearing. We will see that this is possible with the use of Fourier methods; appendices A1 and A2 give a brief reference to these, adapted to their use in this specific situation.

3.2.2 Image formation in fluorescence microscopy

In describing the interaction between matter and radiation inside a microscope, we will use position vectors $\boldsymbol{r}$ for the distribution of matter through space, and wave vectors $\boldsymbol{k}$ for the description of the incident and emitted light. The wave vector $\boldsymbol{k}$ points in the direction of propagation; its components k_x, k_y and k_z are expressed in reciprocal metres. The "reciprocal length" $|\boldsymbol{k}|$ of a wave vector describing a ray of light is $2\pi/\lambda$, with λ the wavelength of the light. The space spanned by all possible wave vectors is called $\boldsymbol{k}$-space, or reciprocal space[1].

We consider a fluorescent sample illuminated by a single monochromatic ray of light with wave vector $\boldsymbol{k}_i$. The light is re-emitted by a fluorochrome molecule at position $\boldsymbol{r}$ as a single monochromatic ray of light with wave vector $\boldsymbol{k}_d$. Monochromatic light means that $|\boldsymbol{k}| = k_0$ is fixed. The field at the detector is build up from the interference of fluorescent light from various molecules. The phase differences are included in the field

$$U(\boldsymbol{k}_\mathrm{i},\boldsymbol{k}_\mathrm{d},\boldsymbol{r}) = U_0 \cdot e^{i(\boldsymbol{k}_\mathrm{i}-\boldsymbol{k}_\mathrm{d})\cdot(\boldsymbol{r}-\boldsymbol{f})} \tag{1}$$

where $\boldsymbol{f}$ is the present focal point in the sample (F in Figure 3.1). Arbitrarily, we have set the phase of a fluorochrome molecule at $\boldsymbol{f}$ to zero. The factor U_0 in (1) contains the amplitude of the radiation, the distance between the object and the detector, and parameters depending specifically on the interaction process. We assume U_0 to be identical for all fluorochrome molecules in the sample. In (1), the field is given in complex notation; this is allowed provided that measurable quantities derived from (1), like the detected intensity, are real numbers. The intensity, as measured with a photomultiplier tube, is proportional to $|U|^2$. Equation (1) does not contain a time-dependence: as all fields (or rather intensities) are studied in a microscope over time scales much longer than the ratio (wavelength / light speed), we will restrict ourselves to the position and wave vector dependencies in the field.

In a confocal microscope, a cone of light focused on the point F in the sample causes illumination from many different angles $\boldsymbol{k}_i$ depending on the aperture angle of the lens used. Also, many detected rays with wave vectors $\boldsymbol{k}_d$ come together in the point F'. Equation (1) contains the contribution of one incident ray of light, one fluorochrome molecule, and one detected ray of light. To obtain the field in F', the contributions of all fluorochrome molecules, all $\boldsymbol{k}_i$ and all $\boldsymbol{k}_d$ must be summed. We can write this summation as an integration by introducing three distribution functions.

The first function describes the spatial distribution of fluorochrome molecules. This function $a(\boldsymbol{r})$ equals 1 if there is a fluorochrome molecule at position $\boldsymbol{r}$, and 0 otherwise. One can consider $a(\boldsymbol{r})$ as a "black-and-white picture" of the structure.

The second function describes the distribution of plane waves with which the sample is illuminated. For a ray with wave vector $\boldsymbol{k}$, the distribution function $W_I(\boldsymbol{k})$ equals 1 if the wave vector $\boldsymbol{k}$ is part of the illumination cone, and 0 otherwise. For monochromatic radiation, $W_I(\boldsymbol{k})$ can be equal to 1 only for wave vectors with $|\boldsymbol{k}| = k_0$; therefore all non-zero points of $W_I(\boldsymbol{k})$ lie on a sphere in $\boldsymbol{k}$-space with radius k_0.

Assuming an aberration-free lens, $W_I(\boldsymbol{k})$ is only determined by k_0 and the aperture angle α, as indicated in Figure 3.2, with the positive z-axis directed from the light source to F. Indicated is a sphere with centre F and radius $(1/k_0)$ and two vectors $\boldsymbol{v}$ pointing in the propagation direction of the rays by which the sample is illuminated, with length $(1/k_0)$. All illumination vectors $\boldsymbol{v}$ together form a spherical cap (drawn bold) bounded by the illuminating cone with top angle (2α), with α the aperture angle of the lens. In the $\boldsymbol{k}$-space, all nonzero points of $W_I(\boldsymbol{k})$ form the equivalent of this spherical cap.

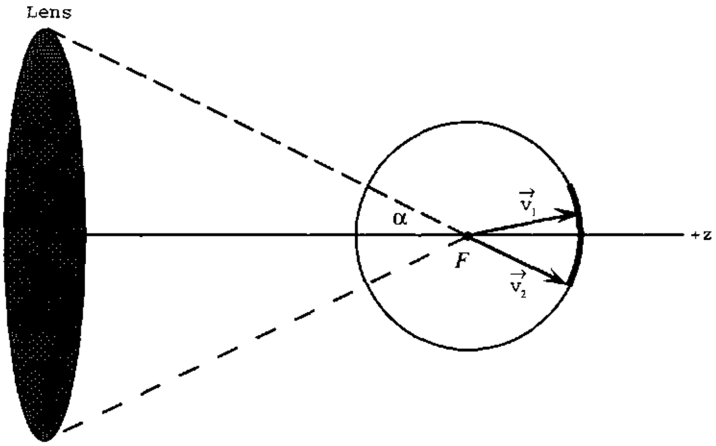

Figure 3.2: Construction of the distribution function $W_I(\boldsymbol{k})$.

The last function $W_{\mathrm{D}}(\boldsymbol{k})$, the distribution function for detected wave vectors, is defined analogously to $W_{\mathrm{I}}(\boldsymbol{k})$.

Using the three distribution functions, the field in *F*', which we denote by $U(\boldsymbol{f})$, can be written as a triple integral: once over Euclidean space (all fluorochrome molecules) and twice over $\boldsymbol{k}$-space (illuminating and detected radiation):

$$U(\boldsymbol{f}) = U_0 \cdot \int\int\int a(\boldsymbol{r}) \cdot W_{\mathrm{I}}(\boldsymbol{k}_{\mathrm{i}}) \cdot W_{\mathrm{D}}(\boldsymbol{k}_{\mathrm{d}}) \cdot e^{i(\boldsymbol{k}_{\mathrm{i}}-\boldsymbol{k}_{\mathrm{d}})\cdot(\boldsymbol{r}-\boldsymbol{f})} \mathrm{d}\boldsymbol{r}\mathrm{d}\boldsymbol{k}_{\mathrm{i}}\mathrm{d}\boldsymbol{k}_{\mathrm{d}} \tag{2}$$

During a scan in the CSLM, the point ***f*** is moved through the sample. The structure itself, or $a(\boldsymbol{r})$ in (2), is fixed. At a given ***f***, the measured intensity is given by:

$$I(\boldsymbol{f}) = U^*(\boldsymbol{f}) \cdot U(\boldsymbol{f}) \tag{3}$$

where U^* denotes the complex conjugate of *U*. Substitution of (3) yields a sixfold integral:

$$\begin{aligned} I(\boldsymbol{f}) = & \left[U_0^* \cdot \int\int\int a^*(\boldsymbol{r}') \cdot W_{\mathrm{I}}^*(\boldsymbol{k}_{\mathrm{i}}') \cdot W_{\mathrm{D}}^*(\boldsymbol{k}_{\mathrm{d}}') \cdot e^{-i(\boldsymbol{k}_{\mathrm{i}}'-\boldsymbol{k}_{\mathrm{d}}')\cdot(\boldsymbol{r}'-\boldsymbol{f})} \mathrm{d}\boldsymbol{r}'\mathrm{d}\boldsymbol{k}_{\mathrm{i}}'\mathrm{d}\boldsymbol{k}_{\mathrm{d}}' \right] \\ & \cdot \left[U_0 \cdot \int\int\int a(\boldsymbol{r}) \cdot W_{\mathrm{I}}(\boldsymbol{k}_{\mathrm{i}}) \cdot W_{\mathrm{D}}(\boldsymbol{k}_{\mathrm{d}}) \cdot e^{i(\boldsymbol{k}_{\mathrm{i}}-\boldsymbol{k}_{\mathrm{d}})\cdot(\boldsymbol{r}-\boldsymbol{f})} \mathrm{d}\boldsymbol{r}\mathrm{d}\boldsymbol{k}_{\mathrm{i}}\mathrm{d}\boldsymbol{k}_{\mathrm{d}} \right] \end{aligned} \tag{4}$$

Equation (4) may appear complex, but we will restructure it in a form which not only makes it more readable, but also more clearly displays the relevant physical phenomena.

As the functions *a* and *W* are real functions, $a^* = a$ and $W^* = W$. A further simplification comes from the fluorescence process. As the fluorescence decay time (typically of the order of 10^{-8} s) is much larger than the ratio (wavelength / light speed) and varying throughout the sample, the radiation from different fluorochrome molecules will be completely incoherent. The consequence of this is that in (4), contributions to $I(\boldsymbol{f})$ from points ***r*** and ***r***' must be added as intensities, rather than amplitudes, unless ***r*** = ***r***'. This reduces (4) to:

$$\begin{aligned} I(\boldsymbol{f}) = & U_0^* \cdot U_0 \cdot \int a^2(\boldsymbol{r})\mathrm{d}\boldsymbol{r} \\ & \cdot \int\int W_{\mathrm{I}}(\boldsymbol{k}_{\mathrm{i}}) \cdot W_{\mathrm{I}}(\boldsymbol{k}_{\mathrm{i}}') \cdot e^{i(\boldsymbol{k}_{\mathrm{i}}-\boldsymbol{k}_{\mathrm{i}}')\cdot(\boldsymbol{r}-\boldsymbol{f})} \mathrm{d}\boldsymbol{k}_{\mathrm{i}}\mathrm{d}\boldsymbol{k}_{\mathrm{i}}' \\ & \cdot \int\int W_{\mathrm{D}}(\boldsymbol{k}_{\mathrm{d}}) \cdot W_{\mathrm{D}}(\boldsymbol{k}_{\mathrm{d}}') \cdot e^{i(\boldsymbol{k}_{\mathrm{d}}'-\boldsymbol{k}_{\mathrm{d}})\cdot(\boldsymbol{r}-\boldsymbol{f})} \mathrm{d}\boldsymbol{k}_{\mathrm{d}}\mathrm{d}\boldsymbol{k}_{\mathrm{d}}' \end{aligned} \tag{5}$$

We now define the function $T(\boldsymbol{k})$, which is an autocorrelation function of *W*:

$$T(\boldsymbol{k}) \equiv \int W(\boldsymbol{u}) \cdot W(\boldsymbol{u}-\boldsymbol{k})\mathrm{d}\boldsymbol{u} \tag{6}$$

By using (6) the double integrals over the $\boldsymbol{k}$-space in (5) can be simplified. When we use the substitutions $\boldsymbol{u} = \boldsymbol{k}'$ and $\boldsymbol{v} = \boldsymbol{k}' - \boldsymbol{k}$ we arrive at:

$$\begin{aligned} \int\int W(\boldsymbol{k}) \cdot W(\boldsymbol{k}') \cdot e^{i(\boldsymbol{k}-\boldsymbol{k}')\cdot(\boldsymbol{r}-\boldsymbol{f})}\mathrm{d}\boldsymbol{k}\mathrm{d}\boldsymbol{k}' &= -\int\int W(\boldsymbol{u}-\boldsymbol{v}) \cdot W(\boldsymbol{u}) \cdot e^{i\boldsymbol{v}\cdot(\boldsymbol{f}-\boldsymbol{r})}\mathrm{d}\boldsymbol{u}\mathrm{d}\boldsymbol{v} \\ &= -\int T(\boldsymbol{v}) \cdot e^{i\boldsymbol{v}\cdot(\boldsymbol{f}-\boldsymbol{r})}\mathrm{d}\boldsymbol{v} = -(2\pi)^{-1}\check{T}(\boldsymbol{r}-\boldsymbol{f}) \end{aligned} \tag{7}$$

with $\check{T}(\boldsymbol{k})$ the inverse Fourier transform of $T(\boldsymbol{k})$.

Using the above substitution on W_D and the substitutions $\boldsymbol{u} = \boldsymbol{k}$ and $\boldsymbol{v} = \boldsymbol{k} - \boldsymbol{k}'$ on W_I we obtain:

$$I(\boldsymbol{f}) = |U_0|^2 \cdot (2\pi)^{-2} \cdot \int a^2(\boldsymbol{r}) \cdot \check{T}_\mathrm{I}(\boldsymbol{r}-\boldsymbol{f}) \cdot \check{T}_\mathrm{D}(\boldsymbol{f}-\boldsymbol{r})\mathrm{d}\boldsymbol{r} = |U_0|^2 \cdot (2\pi)^{-2} \cdot [a^2 \otimes (\check{T}_\mathrm{I} \cdot \check{T}_\mathrm{D})](\boldsymbol{f}) \tag{8}$$

In (8), the symbol $\otimes$ is shorthand for convolution or smearing, which is explained in some more detail in Appendices A1 and A2. The implication of (8) is that in fluorescence-CSLM the field measured in F' is a spatially smeared version of the true structure a (because a only takes on the values 1 or 0, $a^2 = a$). The degree of smearing in (8) is given quantitatively by inverse Fourier transforms of $T(\boldsymbol{k})$ (defined in (6)) for the incident and detected light. The knowledge of $T_\mathrm{I}(\boldsymbol{k})$ and $T_\mathrm{D}(\boldsymbol{k})$ is the basis to a quantitative understanding of resolution, and to all image restoration techniques.

3.2.3 Degree of smearing: point spread function

To find an expression for $T_\mathrm{I}(\boldsymbol{k})$ we have to calculate the autocorrelation of $W_\mathrm{I}(\boldsymbol{k})$ as defined in (6). As we have seen in Figure 3.2, $W_\mathrm{I}(\boldsymbol{k})$ is a spherical cap with top angle 2α and radius $k_{0,\mathrm{I}} = 2\pi/\lambda_\mathrm{I}$, with λ_I the wavelength of the incident light. The autocorrelation of $W_\mathrm{I}(\boldsymbol{k})$ can be calculated analytically, as explained in Appendix A.3. The resulting $T_\mathrm{I}(\boldsymbol{k})$ is:

$$T_\mathrm{I}(\boldsymbol{k}) = T_\mathrm{I}(k,\theta) = 2 \cdot k_{0,\mathrm{I}} \cdot K \cdot \arccos\left(\frac{k \cdot \cos(\theta) + 2 \cdot k_{0,\mathrm{I}} \cdot \cos(\alpha)}{2 \cdot k_{0,\mathrm{I}} \cdot K \cdot \sin(\theta)}\right); \quad k > 0 \tag{9}$$

with

$$K = \sqrt{1 - \frac{(k/k_{0,\mathrm{I}})^2}{4}} \tag{10}$$

In (9), $\boldsymbol{k}$ is represented in polar coordinates k and θ, with $k = |\boldsymbol{k}|$ and θ the angle with the k_z-axis, which is directed from the light source to the sample. When the spherical caps coincide, $T_\mathrm{I}(\boldsymbol{k})$ becomes the surface area of either spherical cap:

$$T_\mathrm{I}(\boldsymbol{0}) = 2\pi \cdot (1 - \cos(\alpha)) \tag{11}$$

This results in a discontinuity in the θ-coordinate of $T_\mathrm{I}(\boldsymbol{k})$ for $\boldsymbol{k} = \boldsymbol{0}$. The inverse Fourier transform of $T_\mathrm{I}(\boldsymbol{k})$, however, remains a continuous function.

Figure 3.3 gives an example of $T_\mathrm{I}(\boldsymbol{k})$ for a 1.4 NA lens with $\lambda_\mathrm{I} = 540$ nm. Shown are cross-sections of $T_\mathrm{I}(\boldsymbol{k})$ in the $(k_z = 0)$-plane and the $(k_y = 0)$-plane respectively. Greyscales are used to indicate the value of $T_\mathrm{I}(\boldsymbol{k})$ with white as maximum and black as zero level. The halfwidth of the function in Figure 3.3a is 0.6 nm^{-1}.

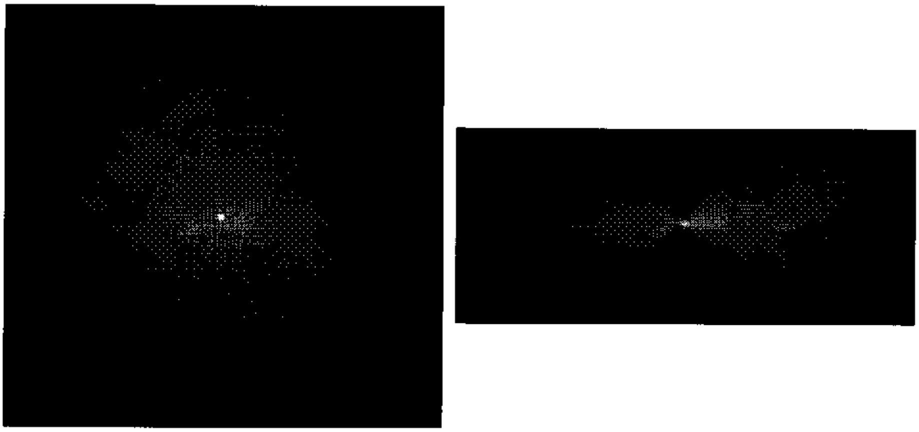

(a) $T_\mathrm{I}(\boldsymbol{k})$ in $k_z = 0$-plane (b) $T_\mathrm{I}(\boldsymbol{k})$ in $k_y = 0$-plane

Figure 3.3: $T_\mathrm{I}(\boldsymbol{k})$ for NA = 1.4 and $\lambda_\mathrm{I} = 540$ nm.

As the spherical caps W_I and W_D only differ in radius, the function $T_\mathrm{D}(\boldsymbol{k})$ is also calculated using (9) and (10), only with $k_{0,\mathrm{D}}$ used instead of $k_{0,\mathrm{I}}$. The combination $h(\boldsymbol{r}) \equiv \check{T}_\mathrm{I}(\boldsymbol{r}) \cdot \check{T}_\mathrm{D}(\boldsymbol{r})$ is called the point spread function^2 or PSF for fluorescence CSLM: when an infinitesimal object is studied with fluorescence CSLM, the measured three dimensional intensity pattern is proportional to $h(\boldsymbol{r})$. The PSF for a 1.4 NA lens using rhodamine B as fluorochrome excited at the maximum excitation line (λ_{ex} = 540 nm; λ_{em} = 625 nm) was calculated using (9); the result is given in Figure 3.4. Shown are cross-sections of the PSF in the image plane and a plane perpendicular to the image plane. Greyscales are used to indicate the value of the PSF with white as maximum and black as zero level. In Figure 3.4b, the halfwidth is 130 nm in the x-direction and 360 nm in the z-direction.

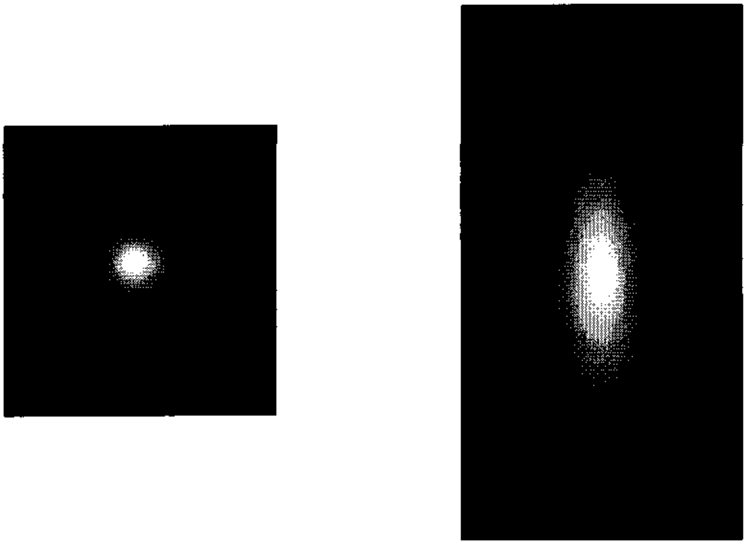

(a) PSF in image plane (b) PSF $\perp$ image plane

Figure 3.4: Point Spread Function for rhodamine; NA = 1.4.

An important feature of the PSF for confocal scanning microscopy is its anisotropy: the axial (*i.e.* perpendicular to the image plane) smearing extends over a larger distance than the smearing in the image plane; in other words the axial resolving power is less than the lateral resolution. Any finite resolution micrograph is a smeared version of the structure which is studied; the three dimensional PSF tells us quantitatively over what distance the structure becomes smeared.

3.3 Deconvolution

3.3.1 Introduction

The resolution of the CSLM micrographs, especially in the axial direction, can be greatly improved when the smearing process is inverted by digital image processing. This inversion process is called deconvolution of the PSF. Deconvolution is usually done with the help of Fourier methods: The Fourier convolution theorem states that if a measured function g is a convolution of the uncorrupted signal s and a PSF h, s can be regained in Fourier space by a simple division (see A2).

$$g = s \otimes h \quad \Leftrightarrow \quad \hat{s} = \frac{\hat{g}}{\hat{h}} \tag{12}$$

The circumflex accent indicates the Fourier transform of a function. This deconvolution scheme, which is called inverse filtering, is easily implemented for a measured dataset g provided h is known. The necessary Fourier transforms can be calculated using fast Fourier-transform methods.

3.3.2 Constrained deconvolution

The Fourier transform $\hat{s}(\boldsymbol{k})$ of a smooth, square integrable function will allways become 0 for large $|\boldsymbol{k}|$. Normally, $\hat{g}$ in (12) becomes 0 at smaller $|\boldsymbol{k}|$ than $\hat{h}$, so the ratio in (12) will always converge. Problems arise, however, when $\hat{g}$ is subject to noise. Uncorrelated ("white") noise, which has a constant spectrum, will always lead to a nonzero tail in $\hat{g}$, which becomes amplified beyond proportion when $\hat{h}$ becomes 0 at large $|\boldsymbol{k}|$. As a consequence, the deconvolved micrograph severely suffers from noise. An improved deconvolution scheme[3] is called constrained deconvolution which allows for a discrepancy between g and $s \otimes h$ caused by noise:

$$\int (g(\boldsymbol{r}) - [s \otimes h](\boldsymbol{r}))^2 \mathrm{d}\boldsymbol{r} = \varepsilon \tag{13}$$

with ε defined as the total amount of noise in one micrograph. In most cases ε is not known. Even when ε is known exactly, an infinite set of functions s satisfies Equation (13); a deconvolution scheme based upon (13) must therefore be closed with an additional constraint. A standard assumption, though not necessarily correct, is that s, the uncorrupted signal, must be relatively free of noise. Noise is normally characterized by short wavelength fluctuations; we will design a short wavelength fluctuation response function L for s, and define ε' to be the total amount of short wavelength fluctuations in one micrograph.

$$\varepsilon' \equiv \int ([s \otimes L](\boldsymbol{r}))^2 \mathrm{d}\boldsymbol{r} \tag{14}$$

A good choice for L is to make the convolution $s \otimes L$ an approximation of $\nabla^2 s$, so noise suppression will not directly affect intensity gradients. For digitized pictures this can be achieved by giving L the form illustrated in Figure 3.5 (in one dimension). The distance Δ is chosen equal to the pixel size. This choice for L is called the Laplace filter.

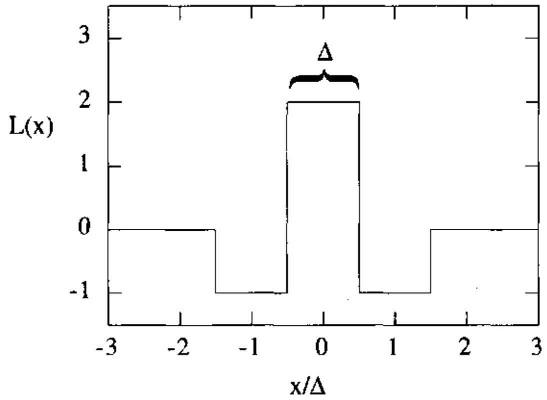

Figure 3.5: Laplace filter.

The deconvolution scheme now becomes: find a minimum in $\varepsilon' + \mu \cdot \varepsilon$ with μ a positive number regulating the relative importance of ε and ε' in the minimalisation procedure. In this minimalisation s is varied; ε and ε' are functionals of s. The Euler-Lagrange equation for the minimalisation is:

$$\frac{\delta}{\delta s}\left([s \otimes L]^2 + \mu[g - (s \otimes h)]^2\right) = 0 \tag{15}$$

Differentiation with respect to the function s yields:

$$(s \otimes L \otimes L) + \mu[(g \otimes h) - (s \otimes h \otimes h)] = 0 \tag{16}$$

Fourier transformation of (16) gives an expression for $\hat{s}$:

$$\hat{s} = \frac{\hat{g} \cdot \hat{h}}{\kappa \cdot \hat{L} \cdot \hat{L} + \hat{h} \cdot \hat{h}} \tag{17}$$

with $\kappa = 1/\mu$. We can see that for $\kappa = 0$ the inverse filtering scheme is recovered. For increasing κ, $\hat{s}$ will decay faster from $\hat{s}(0)$ to 0. For very large κ, only $\hat{s}(0)$ will be nonzero; the corresponding s

is a constant. We see that, as could be expected, κ sets the smoothness for s obtained by deconvolution. A general prescription for κ cannot be given; the strategy we will use is to choose κ close to 0, but large enough to avoid the noise amplification in inverse filtering.

For the Laplace-filter, $\int L(\boldsymbol{r})\mathrm{d}\boldsymbol{r} = \hat{L}(0) = 0$. Therefore in (17), regardless of κ:

$$\hat{s}(0) = \frac{\hat{g}(0)}{\hat{h}(0)} \tag{18}$$

Hence, in deconvolution, the total intensity in the picture is diminished by a factor equal to the integrated PSF. This diminishing does not depend on noise.

Equation (17) can be directly applied to digitized pictures using discrete Fourier transforms. After deconvolution using (17), the resolution in the restored micrograph will now be determined by κ-smoothness and round-off errors. Because the actual PSF cannot be known exactly, there will in practice always be some residual smearing after deconvolution with the approximate PSF.

3.4 Analysis of CSLM micrographs

3.4.1 Density autocorrelation function

For a CSLM micrograph, a straightforward way to generalise the structure is a calculation of the fluorochrome density autocorrelation function (DACF) $c(\boldsymbol{r})$, which is defined as:

$$c(\boldsymbol{r}) = \frac{\langle \rho(\boldsymbol{r}')\rho(\boldsymbol{r}'+\boldsymbol{r})\rangle_{\boldsymbol{r}'}}{\langle \rho(\boldsymbol{r}')\rangle_{\boldsymbol{r}'}^2} \tag{19}$$

where $\rho(\boldsymbol{r}')$ is the fluorochrome density at position $\boldsymbol{r}'$, and $<...>_{\boldsymbol{r}'}$ denotes an average over all positions $\boldsymbol{r}'$ in the micrograph. $\langle \rho(\boldsymbol{r}')\rangle_{\boldsymbol{r}'}$, or simply $<\rho>$, is the average density. In the analysis of CSLM images, measured intensities are treated as fluorochrome densities. Moreover, we assume that the density of fluorochrome is simply proportional to the density of colloid material. $c(0)$ is given by:

$$c(0) = \frac{\langle [\rho(\boldsymbol{r}')]^2\rangle_{\boldsymbol{r}'}}{\langle \rho(\boldsymbol{r}')\rangle_{\boldsymbol{r}'}^2} = \frac{<\rho^2>}{<\rho>^2} \tag{20}$$

For all density distributions other than uniform, $<\rho^2>$ is larger than $<\rho>^2$.

When we study the correlation between $\rho(\boldsymbol{r}')$ and $\rho(\boldsymbol{r}'+\boldsymbol{r})$, it will be maximal for $r=0$. In a disordered system, $\rho(\boldsymbol{r}')$ and $\rho(\boldsymbol{r}'+\boldsymbol{r})$ will become more uncorrelated the larger $|\boldsymbol{r}|$ becomes. In the limit for infinite $|\boldsymbol{r}|$ they will be completely uncorrelated:

$$\lim_{|\boldsymbol{r}|\to\infty} c(\boldsymbol{r}) = \frac{\langle \rho(\boldsymbol{r}')\rangle_{\boldsymbol{r}'} \cdot \langle \rho(\boldsymbol{r})\rangle_{\boldsymbol{r}}}{\langle \rho(\boldsymbol{r}')\rangle_{\boldsymbol{r}'}^{2}} = \frac{<\rho>^2}{<\rho>^2} = 1 \tag{21}$$

By definition, for an isotropic structure, $c(\boldsymbol{r})$ becomes $c(r)$.

3.4.2 DACF and pair correlation function

In interpreting the structure of a colloid, we are interested in the distribution of particles through space rather than in the distribution of densities through space. The former is described by the pair correlation function $g(\boldsymbol{r})$. The connection between $c(\boldsymbol{r})$ and $g(\boldsymbol{r})$ for a noise-free micrograph of a homodisperse colloid containing N particles in a volume V, as explained in Appendix A4, is given by:

$$c(\boldsymbol{r}) = \frac{V}{N} \cdot P(\boldsymbol{r}) + [g \otimes P](\boldsymbol{r}) \tag{22}$$

The implication of (22) is that for large $\boldsymbol{r}$, $c(\boldsymbol{r})$ is a smeared version of $g(\boldsymbol{r})$. The smearing function $P(\boldsymbol{r})$ is the DACF of an isolated single particle. For the local density $p(\boldsymbol{r})$ within a single particle (with its centre of mass placed on the origin) it is:

$$P(\boldsymbol{r}) = m_{\mathrm{p}}^{-2} \cdot [p \otimes p](\boldsymbol{r}) \tag{23}$$

where $m_{\mathrm{p}} = \int p(\boldsymbol{r})\mathrm{d}\boldsymbol{r}$ is the mass of one particle. The integral $\int P(\boldsymbol{r})\mathrm{d}\boldsymbol{r}$ equals 1. Note that the total smearing range is proportional to twice the size of a single particle. Alternatively one could use the mass distribution within the particle to describe the fluorochrome density distribution inside particles.

The discrepancy between $c(\boldsymbol{r})$ and $g(\boldsymbol{r})$ is important in interpreting CSLM micrographs of colloids. The smearing of $g(\boldsymbol{r})$ makes it impossible to interpret the DACF on small length scales, and on length scales where there are strong oscillations in $g(\boldsymbol{r})$. Note that the finite size and the finite resolution have the same effect on $g(\boldsymbol{r})$, and both could in principal be removed by deconvolution techniques.

When the colloidal particles are small with respect to the pixel size, the smearing with $P(\boldsymbol{r})$ becomes unimportant. Here, the DACF can be considered a multiple pair correlation function: two particles at position ***r'*** and three particles at position ***r'+r*** contribute six particle pairs at separation vector ***r*** to the average in (19). On length scales much longer than one pixel, the DACF is equal to $g(\boldsymbol{r})$.

For an increasing pixel size, however, the structural information on which the deconvolution must be based also decreases, which leads to improper deconvolution with residual smearing. The best, but not the most economic option would be to choose the smallest possible pixel size and only interpret the DACF at large $\boldsymbol{r}$. This means that the amount of data that can be handled by both the microscope and the deconvolution software should be substantial.

3.4.3 Fractal scaling in the DACF

In the case of a fractal structure, the DACF exhibits fractal scaling. We will start by deriving an expression for scaling in $g(r)$. As seen in Chapter 2 (equation 7), for fractal scaling in a colloid, the number of particles within range of another particle $n(r)$ obeys the following scaling region:

$$n(r) = 4\pi \frac{N}{V} \int_0^r l^2 g(l) \mathrm{d}l = \varphi_{\mathrm{cp}} \left(\frac{r_0}{a} \right)^3 \left(\frac{r}{r_0} \right)^{d_\mathrm{f}} \tag{25}$$

with φ_{cp} the volume fraction of close packing, r_0 the fractal lower cutoff, a the particle radius and d_f the fractal dimensionality. From (25) we can derive the scaling in $g(r)$ in the fractal region:

$$g(r) = \frac{d_\mathrm{f} \varphi_{\mathrm{cp}}}{3\varphi_0} \cdot \left(\frac{r}{r_0} \right)^{d_\mathrm{f}-3} \tag{26}$$

in which φ_0 is the overall volume fraction of particles in the system. We see that in the fractal scaling region, $g(r)$ is a decreasing function ($d_\mathrm{f} < 3$), from which d_f can be calculated by applying a double logarithmic fit. When the measured DACF is a substantially smeared version of $g(r)$, as will be the case without deconvolution, applying a logarithmic fit to $c(r)$ instead can yield an incorrect value for d_f.

In the logarithmic fit, also the fractal lower cutoff r_0 can be determined. Using a pixel size λ_{pix}, the fractal scaling in $c(r/\lambda_{\mathrm{pix}})$ is given by:

$$c(r/\lambda_{\mathrm{pix}}) = \frac{d_\mathrm{f} \varphi_{\mathrm{cp}}}{3\varphi_0} \cdot \left(\frac{r_0}{\lambda_{\mathrm{pix}}} \right)^{3-d_\mathrm{f}} \cdot \left(\frac{r}{\lambda_{\mathrm{pix}}} \right)^{d_\mathrm{f}-3} \tag{27}$$

From (27) we see that in a logarithmic fit, once d_f is determined from the slope, r_0 can be determined from the intercept, given φ_{cp} and φ_0.

3.5 Discussion and conclusions

In this chapter the basis is presented for the use of confocal scanning microscopy as a tool to study the structure of particle gels, and particularly the fractal scaling in particle gels. However promising the "direct measurement of structure" may seem, or however informative the micrographs may appear to the eye, a good quantitative structural analysis of a colloid is only possible if the main three problems are understood and overcome:

1. Smearing of the structure with an anisotropic PSF in the microscope;

2. Noise effects in the deconvolution;

3. A discrepancy between the DACF and $g(\boldsymbol{r})$.

It is described above how this can be done in principle. It should be noted that the optical treatment contains a number of ideality assumptions. Firstly it is assumed that the optical system used shows no aberration. Chromatic aberrations can in principle be treated in the calculation of the PSF[2], but this makes an analytical derivation impossible. Experimental determination of the PSF suggests the presence of aberrations[4]. Measuring the PSF by deconvolution, however, is not easy: the measurements must be done very carefully and noise effects influence the measured PSF just as in the deconvolution in this chapter. In our work, we have chosen not to measure the PSF, but assume that a proper deconvolution can be executed using a simple model with as only parameters the NA of the lens, the wavelengths used, and a smoothness parameter κ. In [4], the authors mention a strong sensitivity of deconvolved pictures to small errors in the PSF. This sensitivity causes noise ("ringing artefacts") in the pictures. These artefacts were not observed in our deconvolutions.

Secondly, we assume infinitesimally small pinholes, which is in practice untrue. It is relatively simple to incorporate a finite-sized pinhole in the calculation of the PSF. For a correctly aligned CSLM (*i.e.* with minimal pinhole size), however, a finite-sized pinhole does not affect the resolution strongly[2]. The wavelengths used and the NA of the lens are far more important parameters.

The limitation of constrained deconvolution is determined by the value of κ in (17). Iterative procedures to find the optimal κ have been suggested[3]. We have followed a different scheme, based upon the insensitivity of the observable we analysed (the DACF) for the choice of the smoothness parameter.

The discrepancy between the DACF and $g(\boldsymbol{r})$ could in principle be solved by deconvolution of $P(\boldsymbol{r})$ in (22). We expect this deconvolution to be delicate in practice, especially when the smearing distance is of pixel order, which will often be the case. Iterative reconstruction algorithms will probably be a solution to this. This point merits further study.

Altogether, we have come to an important understanding of ways of improvement of quantitative confocal scanning microscopy. The treatment of the three problems mentioned requires extensive, but not impossible numerical calculations. Extrapolating the growth of computational strength available to the average researcher, however, these calculations will probably become much more accessible within a few years.

APPENDICES

A1 Convolution

The convolution g between two functions s and h in one dimension is defined as:

$$g(t) = \int s(t')h(t-t')\mathrm{d}t' \equiv [s \otimes h](t) \tag{28}$$

For convolutions we use the shorthand symbol $\otimes$. It can be imagined that a one-dimensional signal $s(t)$ (Figure 3.6a) is measured with an imperfect detector yielding a smeared version $g(t)$ (Figure 3.6c) of the original. This smearing can be described quantitatively using (28) and a detector response function $h(t)$. The response function which results in Figure 3.6c is a Gaussian, drawn in Figure 3.6b.

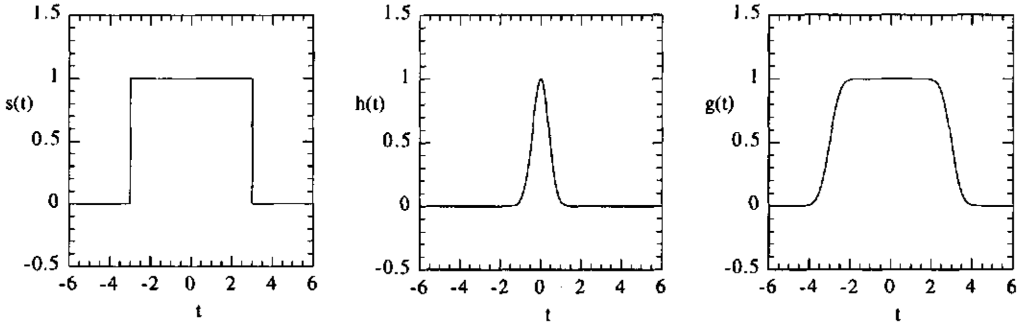

(a) True signal (b) Response function (c) Convolution

Figure 3.6. Example of convolution.

In many cases a measured signal can be described as a convolution between the true signal and a measurement response function. In this example the halfwidth of the response function is a measure of the degree of smearing. A special limiting case is the response function that would cause no smearing at all; this is called the Dirac delta function. The Dirac delta function in Figure 3.6 would be a Gaussian with zero halfwidth and, as a consequence, the value infinity at its maximum. It is clear that detectors with a response like this are unrealisable in practice.

A2 Fourier convolution theorem; deconvolution

For many experimental situations, it is possible to obtain an expression for the detector response function based on knowledge of the detector. To correct for detector imperfections, it would be desirable (see Figure 3.6) to calculate the true signal $s(t)$ from the measured signal $g(t)$ on the basis of a known $h(t)$ using (28). This process is called deconvolution. In practice, deconvolution is performed by using numerical techniques. An efficient way of deconvolution makes use of the Fourier convolution theorem. The Fourier transform of a function $g(t)$ is defined as:

$$\hat{g}(q) \equiv \int g(t) \cdot e^{2\pi iqt} \mathrm{d}t \tag{29}$$

Without any loss of information, the function $g(t)$ can be calculated from $\hat{g}(q)$ by an inverse Fourier transform:

$$g(t) = \int \hat{g}(q) \cdot e^{-2\pi iqt} \mathrm{d}q \tag{30}$$

The Fourier convolution theorem states that:

$$g(t) = [s \otimes h](t) \quad \Leftrightarrow \quad \hat{g}(q) = \hat{s}(q) \cdot \hat{h}(q) \tag{31}$$

Making use of the fact that in Fourier-space a convolution becomes a multiplication, the function s can now be regained from h and g by an inverse Fourier transform:

$$s(t) = \int \hat{s}(q) \cdot e^{-2\pi iqt} \mathrm{d}q = \int \frac{\hat{g}(q)}{\hat{h}(q)} \cdot e^{-2\pi iqt} \mathrm{d}q \tag{32}$$

Therefore, for a complete deconvolution we need two Fourier transforms, one division and one inverse Fourier transform. Fourier deconvolution can be implemented numerically in a very efficient way using Fast Fourier Transformation (FFT).

Two integrals similar to (28), which may be encountered in problems related to convolution or smearing, are given in Equation (33) with appropriate Fourier convolution theorems:

$$g(t) = \int s(t')h(t+t')\mathrm{d}t' \quad \Leftrightarrow \quad \hat{g}(q) = \hat{s}(-q) \cdot \hat{h}(q) \tag{33a}$$

$$g(t) = \int s(t')h(t'-t)\mathrm{d}t' \quad \Leftrightarrow \quad \hat{g}(q) = -\,\hat{s}(q) \cdot \hat{h}(-q) \tag{33b}$$

The integral in (33a) is called the correlation between $s(t)$ and $h(t)$.

A3. Convolution between two spherical segments

The construction leading to Equation (9) is illustrated in Figure 3.7:

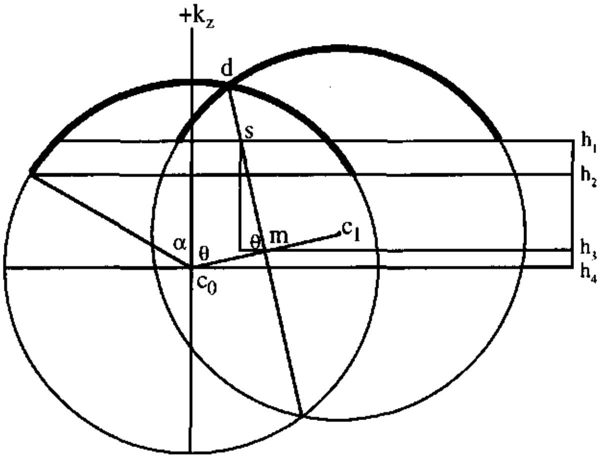

Figure 3.7: Geometrical construction to Equation (9).

Figure 3.7 indicates two spheres each with radius k_0 whose centres c_0 and c_1, both in the drawing plane, lie a distance k apart. The k_z-axis lies also in the drawing plane; c_0 is the origin of the $k_x k_y k_z$-axis system. The spherical caps which form W are drawn bold (see Figure 3.2); α is the lens aperture angle. The intersection of the complete spherical surfaces as a function of k is a circle with radius equal to the distance *md*, with:

$$md = \sqrt{k_0^2 - \frac{k^2}{4}} = k_0 \cdot \sqrt{1 - \frac{k^2}{4k_0^2}} = k_0 \cdot K \tag{34}$$

In Figure 3.7, the plane containing the intersection circle is directed perpendicular to the paper, and parallel to the line *md*. The intersection of the spherical caps is a segment of the complete intersection circle; the function $T(\boldsymbol{k})$ is equal to the arc length of this segment:

$$T(\boldsymbol{k}) = 2 \cdot md \cdot \arccos\left(\frac{ms}{md}\right) \tag{35}$$

For the distance *ms* we find:

$$ms = \frac{h_1 h_3}{\sin(\theta)} = \frac{k_0 \cdot \cos(\alpha) + (1/2) \cdot k \cdot \cos(\theta)}{\sin(\theta)} \tag{36}$$

yielding:

$$T(\boldsymbol{k}) = 2 \cdot k_0 \cdot K \cdot \arccos\left(\frac{2 \cdot k_0 \cdot \cos(\alpha) + k \cdot \cos(\theta)}{2 \cdot k_0 \cdot K \cdot \sin(\theta)}\right) \tag{37}$$

A4 Pair correlation function and density autocorrelation function

For N point particles in a volume V, the local number density $n(\boldsymbol{r})$ can be expressed using Dirac delta functions:

$$n(\boldsymbol{r}) = \sum_{i=1}^{N} \delta(\boldsymbol{r} - \boldsymbol{r}_i) \tag{38}$$

where $\boldsymbol{r}_i$ is the coordinate vector of the i-th particle. By definition, integration of number density over volume gives the total number of particles:

$$\int_V n(\boldsymbol{r}) \mathrm{d}\boldsymbol{r} = \sum_{i=1}^{N} \left[\int_V \delta(\boldsymbol{r} - \boldsymbol{r}_i) \mathrm{d}\boldsymbol{r} \right] = N \tag{39}$$

The number density autocorrelation function $n_2(\boldsymbol{r})$ is defined as follows:

$$\begin{aligned} n_2(\boldsymbol{r}) &\equiv \frac{< n(\boldsymbol{r}')n(\boldsymbol{r}' + \boldsymbol{r}) >_{\boldsymbol{r}'}}{< n >^2} = V^{-1} \cdot < n >^{-2} \cdot \int_V n(\boldsymbol{r}')n(\boldsymbol{r}' + \boldsymbol{r}) \mathrm{d}\boldsymbol{r}' \\ &= V^{-1} \cdot < n >^{-2} \cdot \sum_{p,q=1}^{N} \delta(\boldsymbol{r} - \boldsymbol{r}_{pq}) \end{aligned} \tag{40}$$

with average number density $< n > = N / V$ and particle separation $\boldsymbol{r}_{pq} \equiv \boldsymbol{r}_p - \boldsymbol{r}_q$.

The function $n_2(\boldsymbol{r})$ contains apart from the spatial number density correlation between particles a trivial part where p and q refer to the same particle ($r_{pq} = 0$). This distinction is made in Equation (41):

$$\begin{aligned} n_2(\boldsymbol{r}) &= V^{-1} \cdot < n >^{-2} \cdot \sum_{p=q} \delta(\boldsymbol{r} - \boldsymbol{r}_{pq}) + V^{-1} \cdot < n >^{-2} \cdot \sum_{p \neq q} \delta(\boldsymbol{r} - \boldsymbol{r}_{pq}) \\ &= < n >^{-1} \cdot \delta(\boldsymbol{r}) + V^{-1} \cdot < n >^{-2} \cdot \sum_{p \neq q} \delta(\boldsymbol{r} - \boldsymbol{r}_{pq}) \qquad (41) \\ &= < n >^{-1} \cdot \delta(\boldsymbol{r}) + g(\boldsymbol{r}) \end{aligned}$$

where the pair correlation function $g(\boldsymbol{r})$ is defined as the non-trivial part of $n_2(\boldsymbol{r})$. The pair correlation function plays a very important role as a structure describing function in theories and simulations on colloidal structure[5-7].

Now we consider the particles to have a finite size and mass, represented by $p(\boldsymbol{r})$, which is the mass density at position $\boldsymbol{r}$ for one particle with its centre of mass placed on the origin. The mass m_{p} of one particle is equal to $\int p(\boldsymbol{r})\mathrm{d}\boldsymbol{r}$. For the whole system, the density $\rho(\boldsymbol{r})$ is given by

$$\rho(\boldsymbol{r}) = [n \otimes p](\boldsymbol{r}) = \sum_{i=1}^{N} p(\boldsymbol{r} - \boldsymbol{r}_i) \qquad (42)$$

Combination of the definitions given in equations (38) and (42), and rearrangement of the functions appearing in the three integrations (one average and two convolutions) one may show that the density autocorrelation function of the full system can be written as:

$$c(\boldsymbol{r}) \equiv \frac{< \rho(\boldsymbol{r}')\rho(\boldsymbol{r}' + \boldsymbol{r}) >_{\boldsymbol{r}'}}{< \rho >^2} = [n_2 \otimes P](\boldsymbol{r}) \qquad (43)$$

with $P(\boldsymbol{r})$ the density autocorrelation function of the mass distribution within a single particle.

$$P(\boldsymbol{r}) = m_{\mathrm{p}}^{-2} \cdot \int p(\boldsymbol{r}')p(\boldsymbol{r}' + \boldsymbol{r})\mathrm{d}\boldsymbol{r}' \qquad (44)$$

Applying the distinction of (41) in $n_2(\boldsymbol{r})$, Equation (43) can be rewritten as:

$$c(\boldsymbol{r}) = < n >^{-1} \cdot P(\boldsymbol{r}) + [g \otimes P](\boldsymbol{r}) \qquad (45)$$

Equation (45) tells us that for large $\boldsymbol{r}$, the density autocorrelation function is a smeared version of the pair correlation function. For $\boldsymbol{r}$ close to 0, $c(\boldsymbol{r})$is dominated by $P(\boldsymbol{r})$, or the density autocorrelation function within a single particle. Note that the finite size of the particles has the same effect on the experimental results as the distortion of the picture due to finite optical resolution. Mathematically the function $P(\boldsymbol{r})$ acts in the same way as the point spread function, though the physical origin is completely different.

Literature

[1] J. W. Goodman, *Introduction to Fourier Optics* (McGraw-Hill, San Francisco, 1968).

[2] T. Wilson, *Confocal Microscopy* (Academic Press, London, 1990).

[3] A. Rosenfeld and A. Kak, *Digital Picture Processing* (Academic Press, Orlando, 1982).

[4] H. T. M. van der Voort and K. C. Strasters, J. Microsc. **178**, 165 (1995).

[5] M. S. Wertheim, J. Chem. Phys **55**, 4291 (1971).

[6] T. Vicsek, *Fractal growth phenomena* (World Scientific, Singapore, 1992).

[7] M. P. Allen and D. J. Tildesley, *Computer simulation of liquids* (Oxford University Press, Oxford, 1993).

4. Confocal microscopy applied to colloidal model systems.

4.1 Introduction

In very few studies confocal microscopy is used quantitatively other than for particle sizing. An excellent example of CSLM (confocal scanning laser microscopy) in colloid chemistry is given by the work of Van Blaaderen et al.[1]; here CSLM is used for the determination of colloidal crystal morphology (FCC or BCC) and for the study of colloidal glasses. The researchers use a system of fluorescently labelled silica particles dispersed in chloroform, which may be considered as the ideal model system for CSLM. In this system the particles and the solvent are both isorefractive (identical refractive index) and isopycnic (identical densities), which means that the laser light can penetrate the sample freely and that sedimentation will be negligible.

In water dispersed colloids, this is usually quite different. Most dispersible solids and liquids have a refractive index considerably higher than that of water, leading to multiple scattering[2]. An example of this is common milk, which multiply scatters back almost all incident radiation. Studying such a turbid system with CSLM is pointless; all relations between incident and detected radiation as described in Chapter 3 will be destroyed by the multiple scattering. Designing a water dispersed model colloid suitable for CSLM is a difficult task; this seriously limits the use of CSLM in colloid chemistry. Still, in this thesis a few model systems are used successfully. Two of these are new and may in the future become important in quantitative optical studies of water dispersed colloids.

This chapter starts with a description of the three model systems used. Next we will describe the preparation of the gels. The image analysis procedure will then be described in detail. The object of this study is to determine fractal properties of the gels; the results of these measurements will be presented and discussed.

4.2 Model systems

4.2.1 Casein micelles

Milk contains proteinaceous particles with an average radius of 60 nm, called casein micelles. These consist predominantly of casein, *i.e.* a mixture of α_{S1}-, α_{S2}-, β- and κ-caseins, calcium phosphate and water. Their voluminosity (total micellar volume per gram dry material) is rather high, between 1.8 and 4.5 ml/g. Casein micelles are sterically stabilized by protruding peptide chains, which are part of the κ-casein. Contributing to their stability, the micelles are negatively charged at physiological pH. The casein micelles in milk can be made to aggregate by adding rennet. Rennet contains the proteolytic enzyme chymosine, that specifically splits the κ-casein, removing the stabilizing peptide chains. Another way of destabilizing the casein micelles in milk is acidification: at pH 4.6 the charge on the micelles becomes zero and the peptide chains collapse.

Being a complex mixture, milk is less suitable as a colloidal model system for aggregation. A solution of sodium caseinate in water at pH 5.2, however, contains roughly the same particles as milk but is less complex. This system has been used in this work and is referred to as "casein micelles". Casein micelles are a convenient model system for CSLM: as the micelles are no compact protein particles, refractive index and density do not differ much from that of the solvent, which results in mild scattering and virtually no sedimentation. A drawback for fundamental research is that the micelles contain a mixture of the different caseins and the solvent, of which the composition can change with temperature, pH and ionic strength, resulting in a varying voluminosity, and hence a varying particle radius[4]. Another drawback is the polydispersity of the system. Nevertheless, the practical relevance of this colloid strongly favours its use in the study of aggregation and gelation.

4.2.2 PFAT Latex particles

A model colloid consisting of perfluoro-alkoxy teflon (PFAT) latex is the result of the search for solid particles with a refractive index nearly matching that of water. The only solid materials suitable for our experiments satisfying this requirement are polymerised perfluorinated carbon compounds. Water dispersed colloids of these materials are prepared by emulsion polymerisation. Unlike the preparation of polystyrene latex, these are extremely hazardous preparations requiring very high pressure and temperature.

Standard teflon or PTFE (poly-tetrafluoroethylene) has a refractive index of 1.31, but is highly crystalline. For this reason, PTFE particles dispersed in water show strong multiple scattering. The crystallinity is reduced to less than 1 percent in PFAT, where the PTFE main chain is substituted with a perfluorinated ether. The PFAT particles have a refractive index of 1.38. This means that by adding fructose (or other inert solutes) to water refractive index matching can be obtained. PFAT dispersions up to a volume fraction of 0.3 can be made transparent.

The dispersions used are charge stabilised with sulfonate groups which stem from the polymerisation initiator potassium persulphate. To enable aggregation, we adsorb the polyelectrolyte PMA-Pe (partially esterified polymetacrylic acid) on the particle surface, which gives a steric stabilisation roughly comparable to κ-casein. At low pH, the adsorbed PMA-Pe undergoes a conformation transition, leading to attractive interactions between particles. Details of the adsorption will be given in section 4.2.4.

The PFAT latex dispersions used are monodisperse with a radius of 80 nm; in this sense it is a much better defined model colloid than casein micelles. A drawback is the density of the particles, which is 1.8 kg/l. Where for small particles the effect of sedimentation is negligible compared to that of Brownian motion, for large aggregates this is certainly not the case. We will address this problem in section 4.2.6.

Unlike silica in chloroform, PFAT latex is a refractive index matched colloid that has hardly been used in colloid science. Piazza and Degiorgio[6] have used partly crystalline PFAT particles for measuring rotational diffusion coefficients; Maste[7] has used PFAT particles for measuring Fourier infrared spectra. The unique optical properties of PFAT latex make it a model colloid that can in future become very important for colloidal research with optical methods. In the experiments with PFAT latex, we have received important help from Dr. D. Lévy from Du Pont de Nemours SA, Le Grand-Saconnex, Switzerland. Dr. Lévy has generously sent us samples of PTFE and PFAT latex. For this help we are greatly indebted.

4.2.3 Glycerol tricapryline emulsion droplets

Both the casein micelles and the PFAT particles are far smaller than the wavelengths of visible light. To facilitate the use of light microscopy in determining the fine structure of particle gels a third model system is used: oil emulsion droplets dispersed in water. This emulsion is made with a Foss Electric 12705 lab homogeniser, the average particle radius is ca. 2 μm. Again, we have selected an oil with a refractive index as close as possible to that of water: glycerol tricapryline (refractive index 1.45; density 0.95 g/ml). The refractive index matching is not very close; a fairly large concentration of fructose is used to obtain samples suitable for microscopy. The emulsion droplets are sterically stabilised with PMA-Pe. At large enough concentration (10 mg per ml oil) this adequately prevents droplet coalescence. At low pH, the emulsion droplets aggregate; an example of emulsion droplets forming a cluster is shown in Figure 4.1 on the next page.

In the system used, the density of the oil phase implies emulsion creaming. For particles of 2 μm diameter, this will not be negligible against Brownian motion. Indeed, aggregation of particles this large cannot easily be compared to aggregation of the smaller particles. Here cluster formation is more the result of velocity gradients induced by rocking the sample. Still, Bibette[8] found very ramified fractal clusters using silicon oil emulsion droplets dispersed in water. We will study this model system and see whether fundamental differences are found with aggregation of smaller particles.

This model colloid can be easily prepared and is suitable (in terms of particle size) for light microscopy; drawbacks are its polydispersity, possible coalescence of droplets and creaming.

However, this system makes it possible to locate the particles on a micrograph, which should make the interpretation of the micrographs easier. Also, like the casein micelles, the system in all its complexity is relevant to many industrial products.

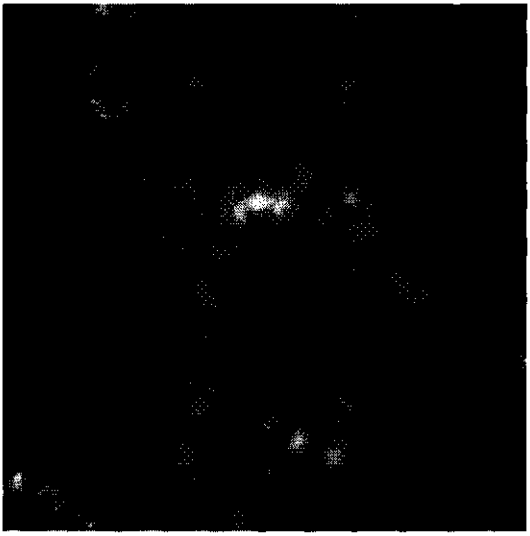

Figure 4.1: CSLM micrograph (29 by 29 μm)
of cluster from emulsion droplets.

4.2.4 Preparation of the dispersions

A suspension of casein micelles was simply made by dissolving the caseinate (provided by the Netherlands Institute of Dairy Research NIZO) in a 0.1 M NaCl solution. A batch of volume fraction $\varphi = 0.1$ (assuming a voluminosity of 2.7 ml/gram casein[4]) was prepared and diluted to desired volume fractions.

The PFAT-latex suspension as provided by Du Pont contained salts and small amounts of perfluorinated surfactants. To remove these products the suspension was cleaned by microfiltration. An Amicon microfiltration apparatus with a Millipore VC filter (pore diameter 50 nm) was filled with the suspension and filtered under an overpressure of 0.5 atm while continuously refreshing the solvent with demineralized water. In this procedure the solvent volume was replaced about 25 times. The resulting suspension was stable due to charged sulphonate groups on the particle surface.

After cleaning, a solution of PMA-Pe (Rohagit S[9]) at dissociation grade 0.5 was added to the suspension. In all samples the concentration of polymer was 10 mg per ml particles[10]; for $\varphi = 0.05$ this amounts to 0.5 mg per ml. For comparison, the bulk gelation concentration for PMA-Pe at low pH is of order 0.1 g per ml[9], so the formation of a PMA-Pe polymer gel is highly unlikely. The result was a suspension that remained stable over months.

Both before and after the adsorption, the hydrodynamic radius was determined using dynamic light scattering. Before adsorption it was found to be 82 nm; after adsorption 87 nm was found. The small value of the second order cumulant[11] indicated a monodisperse distribution.

The oil in water emulsions were prepared by adding a solution of PMA-Pe at dissociation grade 0.5 to glycerol tricapryline, and homogenising the mixture for 30 minutes in a Foss Electric 12705 lab homogeniser ($\varphi = 0.1$). In all samples the concentration of polymer was 10 mg per ml oil.

4.2.5 Labelling of the dispersions

The dispersions were labelled with rhodamineB, which has an excitation maximum of 540 nm and an emission maximum of 625 nm. Rhodamine solutions of 4 mg per ml were prepared freshly and were filtered through a 1 μm membrane to remove rhodamine crystals. For all model systems, a $\varphi = 0.1$ stock suspension was labelled with one droplet of rhodamine solution, colouring the sample a pale shade of pink.

4.2.6 Use of a rotating wheel to prevent sedimentation

All suspensions show sedimentation or creaming due to differences in density between particles and solvent. For stable suspensions, this effect became visible after hours for the emulsions, one day for PFAT latex and several days for casein. For aggregating suspensions, however, sedimentation or creaming has a significant effect on the resulting structure. When we think of gelation in terms of a competition between percolation and phase separation, then gravity will shift the balance towards the latter, as it promotes the formation of a phase rich in particles. This can be clearly seen when an emulsion is destabilised: after a few minutes, a thick cream layer has formed above a clear solution.

The formation of a sediment or a cream layer can be prevented by vertically rotating the sample. (see Appendix A.1) A rotating wheel of which the angular velocity can be varied is used to rotate the aggregating suspensions. Care is taken that no air is contained in the rotating sample; a rotating air bubble would lead to stirring and disruption of the gel structure. This kind of compensation for gravity is not the final solution to the problem, but at least it results in homogeneous gels for PFAT latex suspensions and emulsions at low volume fractions, which without rotation would either sediment or cream.

4.2.7 Preparation of the gels

For all systems, we used GDL (Glucono-δ-lactone) to induce aggregation. GDL dissolves readily in water, and slowly hydrolyses to form gluconic acid. This form of homogeneous acidification is preferable to a simple addition of acid, where the addition causes concentration gradients and stirring causes structure disturbances. A drawback of this type of acidification is that the gelation becomes chemically limited by the hydrolysis kinetics of GDL.

All gels were prepared as follows. Stable suspensions at $\varphi = 0.1$ were first labelled with rhodamine, after which the samples were left for an hour in order to allow the rhodamine to adsorb on the particle surface. Then the samples were diluted to the required volume fraction, after which a calculated amount of GDL was added.

For casein, two GDL concentrations were used: 0.25 and 1.0 g GDL per g sodium caseinate. For a suspension of casein micelles with $\varphi = 0.1$, the lower concentration caused gelation within 30 minutes; the higher concentration caused visible gelation in 10 minutes.

For PFAT latex and the emulsions, the number of carboxyl groups in PMA-Pe and GDL were equivalent at 13.8 g GDL per g PMA-Pe; the two concentrations used for aggregation were 50 and 100 g GDL per g PMA-Pe. For the lower concentrations of GDL, pH values of around 4 were measured after 24 hours; for the larger concentrations of GDL, pH values amounted to around 3.

Upon addition of GDL, the suspension was quickly placed in a hollow objective glass, and sealed with a cover slide. The slide was then placed in the rotating wheel, allowing the sample to gel for approximately 1 hour. All experiments were conducted in the room where the microscope was situated. This room was kept at a constant temperature of 20° C.

4.2.8 Microscope setup

The microscope used was a BioRad MRC 600 with an ILT Argon / Krypton laser as light source. The sample was illuminated at the 568 nm laser line; to filter out stray light in the detector a block filter was used for wavelengths smaller than 585 nm (BioRad YHS filter block). The illumination wavelength does not correspond with the maximum of the excitation spectrum, which is at 540 nm; nevertheless enough fluorochrome molecules are excited to analyse a CSLM picture at the current filter settings. In the deconvolution procedure we shall use the wavelengths 568 nm for illumination and 625 nm for detection, which is the emission maximum of rhodamine B.

A Nikon Plan-Apo 60x 1.4 NA oil-immersion objective was used for the imaging. In all cases the data set analysed consisted of 32 layers of 512 by 512 pixels; this limitation is given by the memory capacity of the most powerful computer available for the deconvolution. A scanned area of 512 by 512 pixels is generally not enough to obtain both a good resolution down to particle level and a sufficient sampling of large scale inhomogeneities in the gel, especially at the lower volume fractions. As we are mainly interested in scaling at length scales larger than the particle size, we have chosen to select for each gel an area larger than the largest inhomogeneities in the gel, as estimated visually.

The axial step size, which was 100 nm in all cases, was corrected for the refractive index difference between the solvent and the immersion oil[12].

In all measurements, the pinhole was used at its minimal size. The photomultiplier tube settings were adjusted in such a way that all available levels of intensity (256) were used as efficiently as possible, but without overflow. This was optimised for every micrograph.

For each gel two micrographs from different regions were recorded.

4.3 Image analysis

4.3.1 Introduction

We will estimate the fractal properties of the gel from the micrographs by using the density autocorrelation function (DACF). To reduce the effect of finite resolution imaging, we deconvolve measured data sets of 32 layers, using a calculated point spread function (PSF).

4.3.2 Deconvolution

An example which illustrates the effect of deconvolution is given in Figure 4.2, which shows the 16th layer of a series of 32 scanned layers (with axial stepsize 100 nm) for a gelled PFAT latex system of $\varphi = 0.05$, representing 21 by 21 μm.

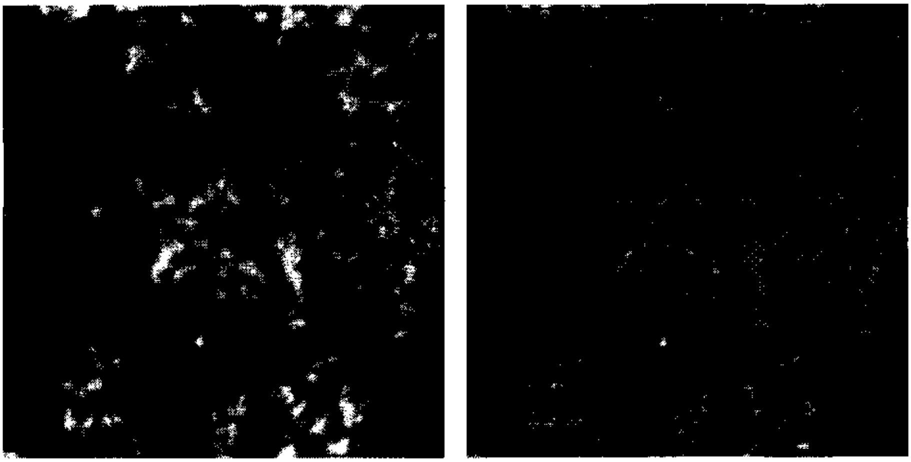

(a) Original micrograph (b) After deconvolution

Figure 4.2: Deconvolution example.

One can see that the deconvolved micrograph contains much more detail than the original. The result shows what can be expected from an optical slice: not all connections present in the 3D network are present in the 2D slice. Nevertheless the objects in Figure 4.2 form a connected network; their position remains fixed in time. Near the edge of the deconvolved micrograph we see an oscillating pattern. This pattern is a known edge effect in deconvolution. For a proper reconstruction of intensities near the edge, intensities from beyond the edge are needed wich are simply not available.

Fourier deconvolution procedures imply that the micrograph is assumed to be periodic; hence near the left edge reconstruction is incorrectly based on intensities from near the right edge[13]. Theoretically, the range of this effect is half the nonzero part of the PSF. In Figure 4.2 we find an edge of 300 nm, which indeed corresponds to half the nonzero part of the PSF used in the deconvolution. For further calculations, this edge is simply omitted.

In the axial direction, the range of the PSF is larger. Here half the nonzero part of the PSF is about 1 μm, which amounts to 10 scanned layers. As a consequence, 20 of the 32 layers cannot be used because of the deconvolution edge effect. It should be noted that no improvement is made when the axial stepsize is increased; when this is done one simply disregards intermediate layers, and the information needed for reconstruction diminishes for the whole picture instead of just near the edges. In this chapter we maintain an axial stepsize of 100 nm, which is the smallest value that could be realised experimentally. Given the current limitation in storage and calculational power, this means that only a single 2D micrograph can be reconstructed for further analysis. Still, there is no theoretical limitation to a full 3D reconstruction; this will become possible using the same program as soon as the practical limitations are overcome.

4.3.3 κ-Parameter

The deconvolution procedure contains a parameter κ, which indicates the degree of noise suppression for the deconvolved micrograph. The effect of κ is best visualised at larger volume fractions. Figure 4.3 shows the 16th layer of a series of 32 scanned layers for a gelled PFAT latex system of φ=0.1, representing 20.4 by 20.4 μm, deconvolved for different values of κ.

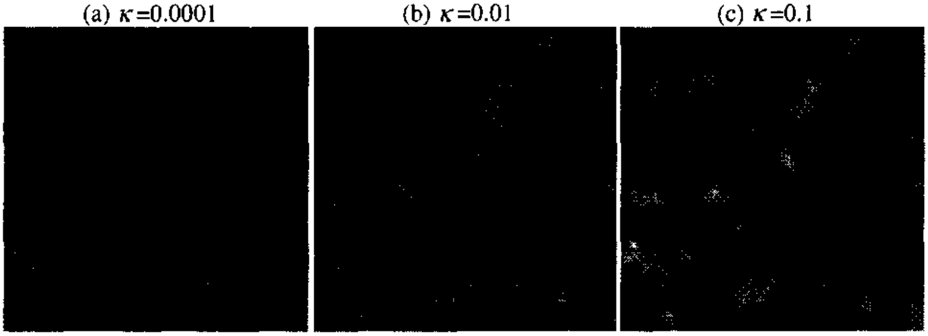
(a) κ=0.0001 (b) κ=0.01 (c) κ=0.1

(*cont.*)

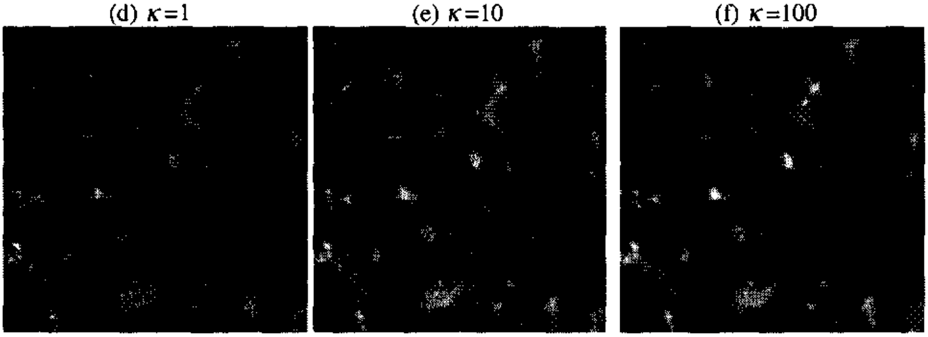
(d) κ=1 (e) κ=10 (f) κ=100

Figure 4.3: Effect of the κ-parameter on the deconvolution

It can be seen that larger values for κ give the micrograph a more smooth appearance, whereas smaller values of κ give the micrograph a grainy appearance. This is in agreement with the trend described in Chapter 3.3.2.

We now come to the point of selecting the optimal value for κ. We will base this choice on the experimental result for the DACF. To do so we start by studying the intensity distribution within one deconvolved micrograph. The purpose of this approach is to further investigate the relation between intensity and the local density of colloidal particles.

4.3.4 Intensity distribution: background removal

The intensity histogram of the micrograph from the previous series deconvolved with κ=10 is given in Figure 4.4. To calculate this histogram, all intensities present in the micrograph were truncated into 512 levels of equal bandwidth. In Figure 4.4, *Count*(*Int*) is the number of times that a pixel with an intensity in the level around *Int* occurs in the micrograph.

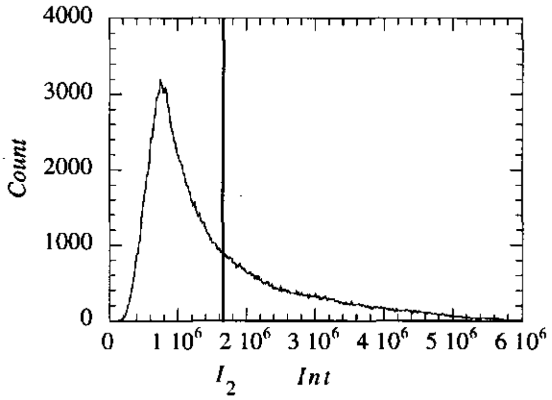

Figure 4.4: Intensity histogram

A striking feature is the dominating peak at low intensities. To find out what structural elements contribute to this peak, we have thresholded the micrograph of Figure 4.3(e) at an intensity I_2 of twice the peak maximum, indicated in Figure 4.4 by a vertical line: all intensities larger than I_2 are made white, all intensities smaller than I_2 are made black. The result is given in Figure 4.5:

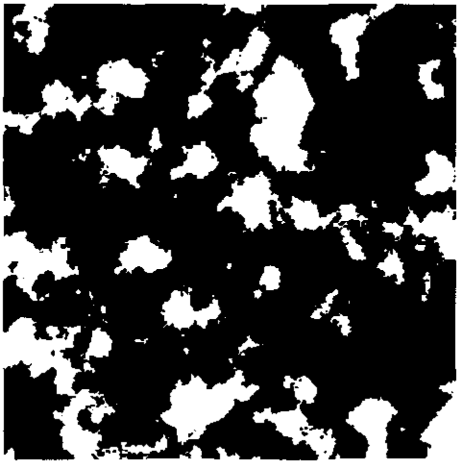

Figure 4.5: Micrograph of Figure 4.3(e) thresholded at I_2

If we compare Figure 4.5 with Figure 4.3, we can see that the peak at low intensities corresponds with empty regions in the micrographs. In contrast, clusters and strands of the gel are represented by intensities larger than I_2.

For a gel at low volume fraction, it can be expected that the empty regions will dominate the intensity histogram. To analyse the distribution of intensities originating from clusters and strands, it is clearer to study the intensity-weighted histogram ($Count \cdot Int$), which gives the contribution of an intensity Int to the total intensity in the micrograph. This histogram is given in Figure 4.6:

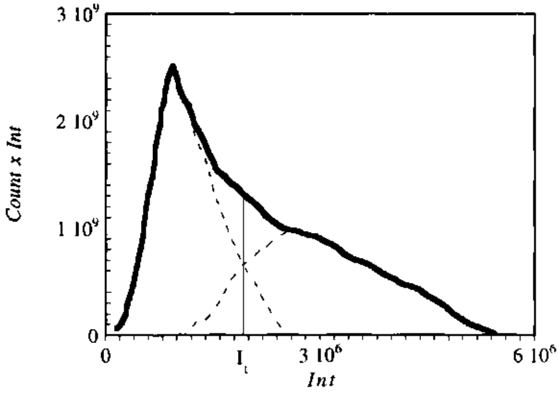

Figure 4.6: Intensity-weighted histogram

In the analysis in chapter 3.4.1 we assumed a simple proportionality between the observed intensity and the colloid density. In this histogram we see that a large fraction of the total intensity, and hence the total mass, comes from the low density regions. One reason may be that there is still a large fraction of all particles in the sol phase, not associated with the dense network of the gel phase. The intensity over an individual 80nm particle in the sol phase would, however, be substantially larger than the peak intensity in figure 4.6.

Our conclusion is that the peak represents intensity contributions from other sources than particles in the image plane. This intensity, which we shall denote as background intensity, can be the result of rhodamine that did not adsorb to particles; it can also be the result of a Fourier artefact in the deconvolution procedure. In the deconvolution, numerical errors are most likely in regions where the intensity does not vary with position (*e.g.* empty regions). This results in a systematic error in the zero level intensity, which can be perceived as background intensity. This error occurs locally for the empty regions and would not be present in regions where the intensity does vary with position (*e.g.* a cluster)[14]. For both explanations, subtracting a background intensity from the whole micrograph would be incorrect. Finally the intensity could originate from particles outside the image plane, which has not been completely removed by the deconvolution. The conclusion about this background is corroborated by the fact that the total mass in the dense regions, assuming close packed structure at maximal intensity pixels, independently reproduces the volume fraction of the full sample within reasonable error (see section 4.3.6).

A closer look at the intensity histogram of figure 4.6 allows us to distinguish two peaks, a high and narrow one at low intensities, which we identify with the background contribution, and a broad and weaker one at higher intensities, which is the signal from the clusters and strands that make up the gel. In figure 4.6 we have sketched these two contributions (the two dotted lines). In some of the micrographs, especially those for the lower volume fractions, the distinction can be made more reliably. In general the background contribution is not very well separated from the signal. Even if the curves could be identified uniquely, there would be the problem of how to handle pixels in the overlap region. Therefore we simply estimate at which intensity the curves intersect, and use this intensity I_t as a threshold for background removal; intensities below the threshold are set to zero.

The result of the background removal is given in Figure 4.7. We can see that the operation does not significantly erode the clearest objects in the original.

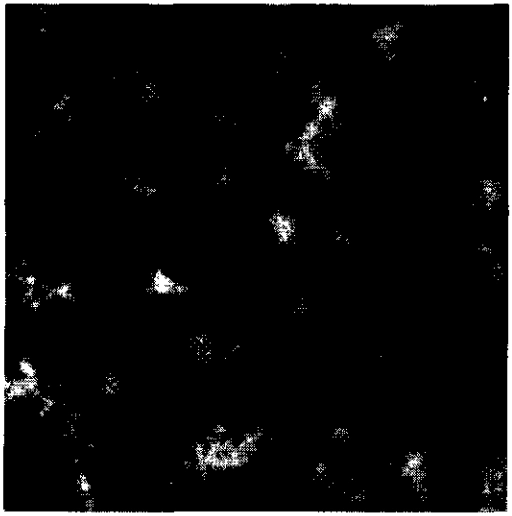

Figure 4.7: Micrograph of Figure 4.3(e)
after background removal.

The removal of background intensity is important for the calculation of the DACF. Without this correction the DACF is influenced by spatial correlations in the background level, as these are weighted equally strong as spatial correlations attributed by clusters and strands. The effect of this would be more unwanted smearing in $g(r)$.

4.3.5 Influence of the deconvolution parameter κ on the DACF

After removal of background intensity, we calculate the DACF $c(\boldsymbol{r})$ for the 16th layer of deconvolved data sets. This calculation is done using two-dimensional discrete Fourier transforms. Figure 4.8 shows a contour plot of $c(\boldsymbol{r})$ decaying from $c(0) = 3.1$ to 1 with contour intervals of 0.1 for κ=10.

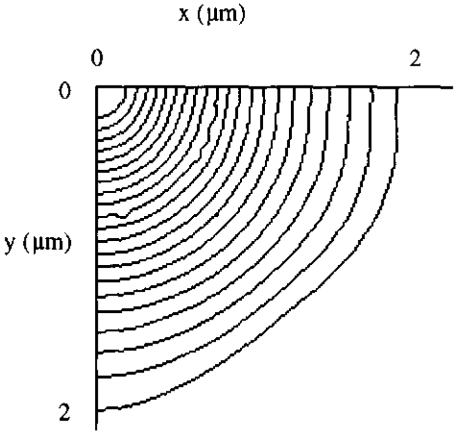

Figure 4.8: contour plot of $c(\boldsymbol{r})$.

The result shows that $c(\boldsymbol{r})$ is nearly isotropic; we approach $c(r)$ by averaging horizontal and vertical directions in $c(\boldsymbol{r})$. The result for the test series using 4 different values for κ is given in Figure 4.9. Figure 4.9 shows a decaying function in which a region of power law scaling can be identified around $r = 1\ \mu\text{m}$. The scaling region is small and not very clear, so scaling results can only be interpreted semi-quantitatively. At smaller distances the slope of $c(r)$ is rather flat, indicating a lower bound on the scaling region: the fractal structure as determined from the micrograph consists of large dense building blocks. A larger value for κ results in a steeper slope (*i.e.* a lower fractal dimensionality); the scaling region remains more constant between κ=1 and κ=10.

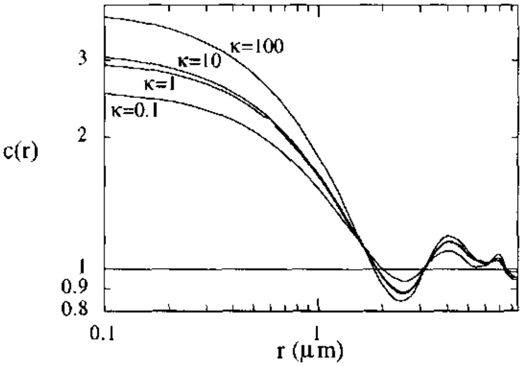

Figure 4.9: DACF for various values for κ.

For κ=100, a lower dimensionality is found, but the deviation from power law scaling occurs at larger r, indicating more smearing at small length scales. As explained in Chapter 3, too large a value for κ will have this effect; an explanation for the lower dimensionality could be that deconvolution at large κ reduces contrast, after which contributions from less concentrated regions are more likely to be removed along with the background. The net result of this would be a "sharpening" of local concentrated points in the micrograph, which causes lower fractal dimensionalities.

For κ=0.1, a higher dimensionality is found. At small κ, the background peak in the intensity histogram broadens (*i.e.* larger background intensities are found) due to deconvolution errors; it will therefore be increasingly difficult to remove both background and noise. As both are homogeneously distributed through the micrograph, the result will be an overestimation of the fractal dimensionality.

At large length scales, $c(r)$ fluctuates around the value 1. These fluctuations are caused by statistical error: the larger r, the less pixels contribute to the average in $c(r)$.

The intermediate values for κ give approximately the same scaling behaviour, which suggests that here the scaling region is not an artefact of the deconvolution procedure, but that it really gives a structural description of the system. As the scaling region for the fractal fit is small, errors in the fractal parameters may be substantial; we will try, however, to explain the results from the analysis and see in what way they can shed light on gel structure and underlying mechanisms.

By fitting the fractal scaling region (see Chapter 3.4.3), we determine the parameters d_f and r_0:

$$c(r) = \frac{d_f \varphi_{cp}}{3\varphi_0} \cdot \left(\frac{r}{r_0}\right)^{d_f - 3} \tag{1}$$

In Equation (1), it is assumed that on the length scales where fractal scaling applies, the DACF and the pair correlation function $g(r)$ are equal. For φ_{cp}, the value 0.76 is used for all micrographs; for φ_0 the known suspension volume fraction is used. From d_{f} and r_0, the correlation length ξ was calculated (see Chapter 2.2.4) according to:

$$\frac{\xi}{r_0} = \left(\frac{\varphi_{\mathrm{cp}}}{\varphi_0} \right)^{1/(3-d_{\mathrm{f}})} \tag{2}$$

The resulting values of the fractal parameters for Figure 4.7 are: $d_{\mathrm{f}}=1.9$; $r_0=340$ nm; $\xi=2.6$ μm. As the diameter of the largest voids that can be discerned in Figure 4.3 is about 5 μm, the value of ξ seems reasonable. The value of r_0 is about four times the particle radius, which indicates substantial reorganisation. In the micrograph we can indeed see compact objects larger than one particle, so the result does not seem unreasonable.

4.3.6 Suspension volume fraction

As a consistency test, we will determine the volume fraction from the micrographs and compare it with the known suspension volume fraction. This is not a straightforward determination: although clearly the average intensity $< I >$ is proportional to the suspension volume fraction φ, the proportionality constant is unknown. We assume that the maximum intensity I_{max} is proportional to the volume fraction of close packing φ_{cp}, yielding:

$$\frac{\varphi}{\varphi_{\mathrm{cp}}} = \frac{< I >}{I_{\mathrm{max}}} \tag{3}$$

A practical problem of this assumption, however, is the fact that I_{max} is statistically the least reliable intensity in the whole micrograph. Also, I_{max} is likely to be underestimated because of residual smearing, which has the greatest effect on peaks with a large intensitiy over a small length scale. Nevertheless we have found that for $\varphi > 0.04$ equation (3) reproduces the value of the volume fraction within 10%. For smaller volume fractions, equation (3) yields a systematic overestimation of the volume fraction by up to a factor 2. We assume that in these cases I_{max} has become quite unreliable because of residual smearing. As mentioned in 4.2.8, the scanned area is chosen on the basis of the largest scale inhomogeneities in the gel, and the number of pixels is fixed (512 by 512 pixels). This means that for the lowest volume fractions, the resolution on particle level is the worst, and here residual smearing will indeed be a serious problem. The good reproduction at high volume fractions indicates that this problem could be solved by simply using more pixels.

4.3.7 General approach

The analysis as described here comprises three consistency tests for each micrograph, based on the histogram for I_t, on the DACF for κ and on the suspension volume fraction in general. We will give a short summary of the treatment:

1. Deconvolution using four values for κ (0.1, 1, 10 and 100);

2. For each deconvolution, background removal according to the intensity-weighted histogram;

3. Fitting of the scaling region confirmed by at least two values for κ.

Before fitting, $c(\boldsymbol{r})$ is tested for isotropy. In practice, we observed an anisotropic $c(\boldsymbol{r})$ only when the scanned area contained just one single strand.

4.4 Results and discussion

The results of the fractal analysis are compiled in the following tables.

Casein:

series	φ_0	[GDL] (g/g)*	d_f	r_0 (nm)	ξ (μm)
1	0.08	0.25	2.2	193.6	3.07
2	0.08	1.0	2.2	174.8	2.84
3	0.05	0.25	2.1	249.0	5.29
4	0.05	1.0	2.0	333.3	4.94
5	0.025	0.25	2.1	311.2	12.47
6	0.025	1.0	2.3	95.5	10.73

*gram GDL per gram casein

PFAT-latex:

series	φ_0	[GDL] (g/g)**	d_f	r_0 (nm)	ξ (μm)
1	0.08	50	2.3	144.1	3.83
2	0.08	100	2.5	46.6	3.71
3	0.04	50	2.3	195.6	16.34
4	0.04	100	2.3	157.4	11.03
5	0.025	50	2.1	255.8	11.63
6	0.025	100	2.2	188.5	12.644
7	0.01	50	2.3	37.6	25.53
8	0.01	100	2.1	79.7	11.93

**gram GDL per gram PMA-Pe

Emulsions:

series	φ_0	[GDL] (g/g)***	d_f	r_0 (μm)	ξ (μm)
1	0.1	50	2.3	0.42	8.4
2	0.1	100	2.1	1.0	9.7
3	0.05	50	2.6	0.026	16.6
4	0.05	100	2.4	0.14	15.0

***gram GDL per gram PMA-Pe

In Appendix A.2 a selection of micrographs is presented for the three model systems.

Generally we see that, as expected, a lower volume fraction results in a larger correlation length ξ. The other fractal results do not show a clear trend. Given the standard deviation in d_f, which is around 10%, on the basis of this data set we can only conclude that all dimensionalities are approximately the same, namely 2.3, a value slightly lower than the consistently found dimensionality of 2.35 by Bremer[5], but larger than DLCA or RLCA-values. Given the standard deviation, many more measurements must be done to confirm that d_f is constant, or to discover a trend in d_f.

More significant differences occur in the values of r_0. In this data set, no uniform effect of either φ_0 or GDL concentration on r_0 is found. To identify more explicit dependencies the amount of data is insufficient. We conclude that the structure of particle gels as studied with CSLM at this stage does not lead to a clear picture.

The fact that no clear picture arises can to some extent be expected: a high φ_0 and a low pH both induce aggregation, but simultaneously also hinder the progress of aggregation because of irreversible cluster formation. To study the balance between these effects many more experiments need be done. From these one may also obtain a clearer understanding between the GDL concentration and the interaction between casein micelles. In this set of experiments the GDL concentration was proportional to the amount of casein present in the system, which means that φ_0 and GDL concentration are correlated. The other extreme would be the variation of the absolute concentration GDL, but this would mean a higher final pH for gels from more concentrated suspensions, *i.e.* also a dependence. Probably, an intermediate situation would give the best tuning of the interaction. Also the time dependence of the interaction is unclear. The final gel structure is not just determined by the final pH of the system, but also by the rate at which the interaction changes from repulsive to attractive. This rate, or even the hydrolysis rate of GDL is not related in a simple fashion to the initial GDL concentration, which is the parameter varied in this set of experiments. A recent study has shown[15] that changes in temperature have a large effect on the structure of GDL-induced casein gels.

Despite the absence of a clear trend, we will make a few remarks on the values of r_0, and give some possible suggestions that may be used in further research.

A striking feature for the casein gels is the large value of r_0. This value varies from 2 to approximately 7 times the radius of a casein micelle, which suggests that in an early stage of the aggregation casein micelles must have combined to form larger compact units. This is indeed possible as the hydrolysis of GDL takes some time, allowing for a stage of moderately reversible aggregation, which results in compact clusters. We will call this early stage pre-aggregation.

For the casein gels, the value of r_0 seems to increase with decreasing volume fraction. Following the previous suggestion, this can be expected: as the amount of GDL is proportional to the amount of casein, at low volume fractions the hydrolysis takes more time, allowing for a longer pre-aggregation stage. The totally inconclusive effect of GDL concentration on r_0, however, does not help us to understand the role of GDL in the pre-aggregation stage.

For the PFAT-latex gels, r_0 is generally smaller than for casein gels, which is the more surprising regarding the larger particle size. Again r_0 seems to increase with decreasing volume fraction. The GDL concentration seems to have a more pronounced effect on r_0 for this system: for smaller GDL concentrations r_0 is larger, which is in accordance with the idea of a pre-aggregation stage.

We would suggest for further research that the hypothesis of a pre-aggregation stage be tested. For the understanding of the aggregation process it would be better if the fractal parameters could be studied as a function of time.

Generally, we find that gels with the same fractal dimensionality do not necessarily have similar structures and underlying aggregation processes. To illustrate this, Figure 4.10 shows two micrographs of casein gels at the same volume fraction (φ = 0.08) but prepared differently: Figure 4.10(a) was prepared by adding 1 g/g GDL; Figure 4.10(b) by first adding 0.1 g GDL per g casein, then waiting for 30 minutes and finally adding 0.9 g GDL per g casein.

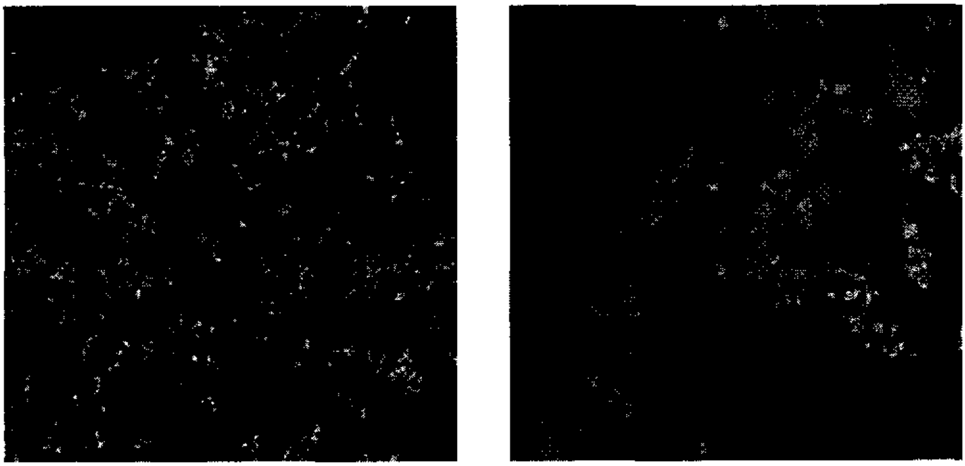

(a): Fast gelation; 28 by 28 μm

(b): Slow gelation; 70 by 70 μm

Figure 4.10: Comparison of two gels with identical d_f.

As calculated from the DACF, both gels turn out to have the same fractal dimensionality (d_f=2.1), despite the fact that they are very different. A more discriminating factor is the value of r_0, which is 175 nm in Figure 4.10(a) and 680 nm in Figure 4.10(b). We can see that in Figure 4.10(b) compact regions indeed extend over larger length scales. This can be attributed to the first addition of GDL, after which aggregation proceeds slowly and reversibly, giving time and opportunity for small length scale compactification. The micrographs show that the aggregation processes for these two systems are different; this does not follow from the fractal dimensionality only.

Even structures with the same values determined for d_f and r_0 are not necessarily identical. To illustrate this, figure 4.11 shows two micrographs of different model systems.

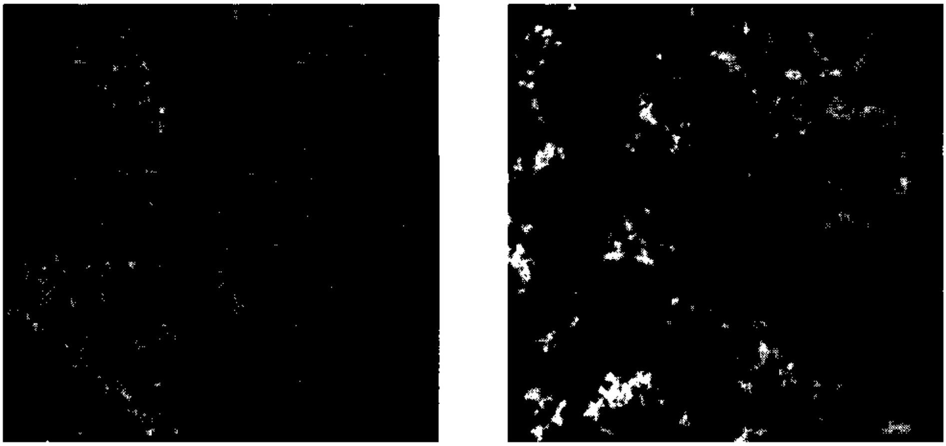

(a) Casein, series 3, 42 by 42 μm

(b) PFAT, series 5, 84 by 84 μm

Figure 4.11 Comparison of two gels with identical d_f and r_0

The two micrographs shown have the same dimensionality (d_f=2.1) and r_0 (250 nm); their volume fractions differ by a factor two ($\varphi_a = 2\varphi_b$) as do their determined correlation lengths ($\xi_b = 2\xi_a$). By showing the micrographs at different magnifications (the pixel size of 4.11(b) is twice the pixel size of 4.11(a)) their structures can be compared; if the determined values are correct we should see identical structures. On large and intermediate length scales the structures indeed seem identical: there are no large differences in branching or in the distribution of voids. On smaller length scales, however, differences can be seen: the structure of Figure 4.11(b) appears to be built from homogeneous fragments larger and more ramified than the small compact fragments of Figure 4.11(b), which suggests different aggregation mechanisms. The fact that the parameter r_0 does not discriminate between the two is caused by the assumption that the value of φ_{cp} which must be used in Equation (1) is 0.76, whereas the local volume fraction in the homogeneous regions in Figure 4.11(b) is probably less than 0.76. This leads to an underestimation of r_0. For a more reliable calculation of r_0, local measurement of φ_{cp} by separately enlarging homogeneous regions would be a significant improvement.

4.5 Conclusions

In this chapter we have attempted to find a quantitative geometrical description of particle gels from confocal micrographs, using a fractal model. Accepting the large statistical variance, it appears that all fractal dimensionalities are about equal, with values larger than the DLCA limit. The values of r_0 show that there can be significant differences between gel structures despite identical values of d_f. The dependence of r_0 on the parameters volume fraction and GDL concentration is unclear, which makes the results in this chapter inconlusive. Still, by speculating on the values of r_0 a hypothesis about a "pre-aggregation stage" is formulated which might serve as a starting point for further research. The fact that the results are inconclusive suggests that no simple model can be applied on these systems.

The analysis method followed in this chapter is thorough, but given the heavy requirements and the many artefacts this work is by no means finished. The combination of model colloid and image analysis procedure can be further optimised on many accounts. The main suggestions are a better labelling, a clearer understanding of the relation between GDL concentration and the interaction between particles and more calculational power for the deconvolution. It would be more informative if the fractal parameters could be studied as a function of time during the aggregation process. We hope that by doing this study, a number of intricacies and pitfalls have been brought to the attention of future investigators.

Literature

[1] A. van Blaaderen *et al.*, Langmuir **8**, 1514 (1992).

[2] J. Lyklema, *Fundamentals of Interface and Colloid Science* (Academic Press, London, 1991).

[3] P. Walstra and R. Jenness, *Dairy Chemistry and Physics* (Wiley, New York, 1984).

[4] S. P. F. M. Roefs, *Ph.D. Thesis*, Wageningen Agricultural University, The Netherlands, 1986.

[5] L. G. B. Bremer, *Ph.D. Thesis*, Wageningen Agricultural University, The Netherlands, 1992.

[6] R. Piazza and V. Degiorgio, Phys. Rev. Lett. **67**, 3868 (1991).

[7] M. C. L. Maste *et al.*, Biochim. Biophys. Acta **1252**, 261 (1995).

[8] J. Bibette*et al.*, Phys. Rev. Lett. **69**, 981 (1992).

[9] T. van Vliet, *Ph.D. Thesis*, Wageningen Agricultural University, The Netherlands, 1977.

[10] J. Böhm, *Ph.D. Thesis*, Wageningen Agricultural University, The Netherlands, 1974.

[11] R. Pecora, *Dynamic Light Scattering* (Plenum Press, New York, London, 1985).

[12] T. Visser, J. L. Oud, and G. J. Brakenhoff, Optik **90**, 17 (1992).

[13] W. H. Press*et al.*, *Numerical recipes in C* (University Press, Cambridge, U.K., 1992).

[14] A. Rosenfeld and A. Kak, *Digital Picture Processing* (Academic Press, Orlando, 1982).

[15] J. A. Lucey*et al.*, to be published (1996).

Appendices

A.1 Suspension rotation

If a vessel containing a colloidal particle undergoes vertical rotation, the particle experiences two forces: the gravitational force and the centripetal force. This is illustrated in Figure 4.12:

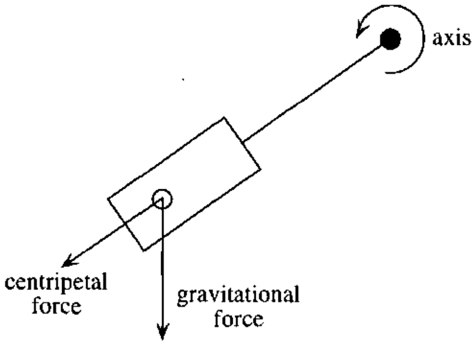

Figure 4.12: Suspension rotation.

Because of the rotation, the angle between both forces changes continuously. During one period of revolution, the path of the particle as viewed from inside the vessel is almost circular, as depicted in Figure 4.13:

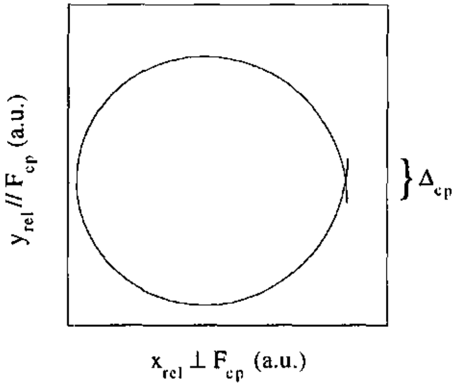

Figure 4.13: particle path.

The path from Figure 4.13 has been calculated numerically; x_{rel} and y_{rel} (y_{rel} parallel to the centripetal force F_{cp}) are the co-ordinates inside the vessel and Δ_{cp} is the net displacement caused by the centripetal force. This net displacement, which is normalised on the particle radius, is given by:

$$\Delta_{\mathrm{cp}} = \frac{\pi^2}{4050} \cdot \frac{L_{\mathrm{w}} \Delta\rho}{\eta T_{\mathrm{rev}}} \tag{1}$$

where L_{w} is the distance between the particle and the axis of the rotation wheel, $\Delta\rho$ the density difference between the particles and the solvent, η the viscosity of the solvent and T_{rev} the period of revolution. The rotational displacement Δ_{rot}, or the diameter of the circle in Figure 4.13 perpendicular to the centripetal force, is given by:

$$\Delta_{\mathrm{rot}} = 2546.43 \cdot \frac{\Delta\rho T_{\mathrm{rev}}}{\eta} \tag{2}$$

Δ_{rot} is also normalised on the particle radius. Ideal compensation of gravity is obtained when both Δ_{cp} and Δ_{rot} are negligible compared to the relative Brownian displacement during one period of revolution. This is never really obtained, but for PFAT latex particles a substantial improvement can be made by adjusting the period of revolution of the rotating wheel T_{rev}. T_{rev} must be chosen not too large (then Δ_{rot} would become too large) and not too small (then Δ_{cp} would become too large). For most cases a T_{rev} of around 10 seconds is used.

A.2 Selection of micrographs

The following page shows 6 micrographs, which illustrate the structure of colloidal gels from the three different model systems. The following legend should be used:

(a) Casein, series 1, 21 by 21 μm;

(b) Casein, series 4, 42 by 42 μm;

(c) PFAT latex, series 1, 28 by 28 μm;

(d) PFAT latex, series 4, 84 by 84 μm;

(e) Emulsion, series 2, 58 by 58 μm;

(f) Emulsion, series 4, 88 by 88 μm

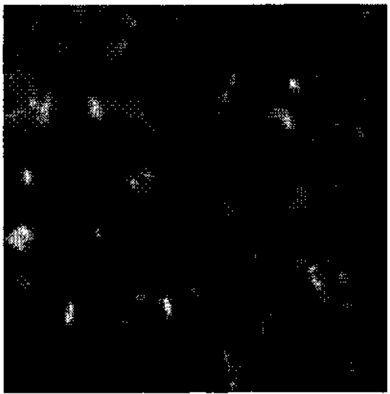
(a)

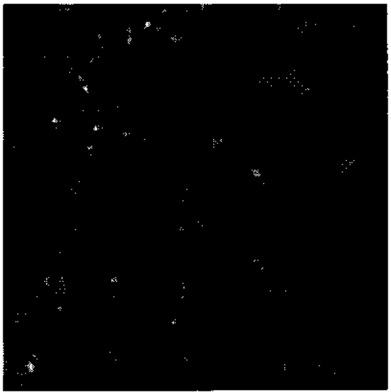
(b)

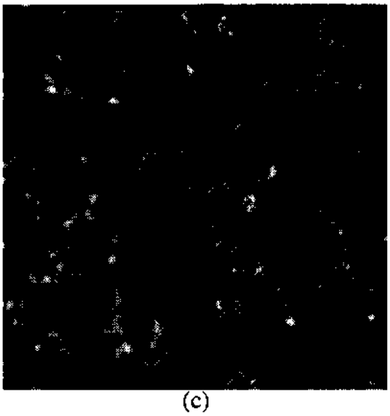
(c)

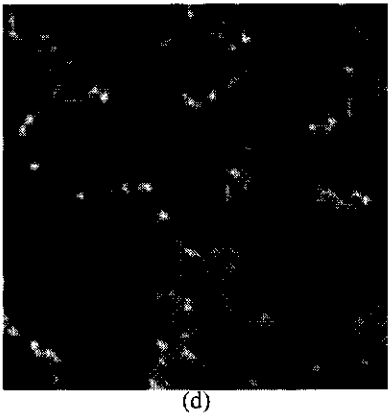
(d)

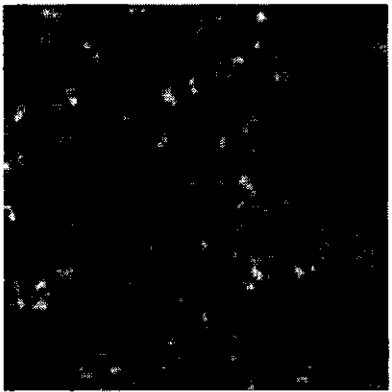
(e)

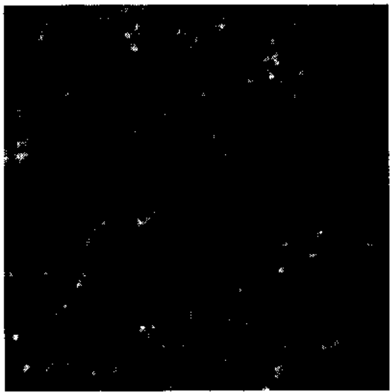
(f)

5. Brownian Dynamics simulation of Gelation and Ageing in Interacting Lennard-Jones Systems

5.1 Introduction

Lyophobic colloids can be stabilised by charging the surface of the dispersed particles. Alternatively, a layer of polymer with high affinity for the solvent can be applied to the particle surface, resulting in steric stabilisation. If the stabilisation is taken away, the colloidal particles will aggregate: particles that collide through Brownian motion will form a cluster. At first clusters are held together by relatively weak attractive forces (*e.g.* Van der Waals forces) between the particle surfaces. On a larger time scale, ageing and sintering lead to more rigid clusters.

A laboratory example of aggregation is the destabilisation of carboxyl-stabilised latex particles dispersed in water. Under alkaline conditions, the particles in this system carry charged groups. Addition of the acid Glucono-δ-lactone removes the charges, resulting in aggregation. Steric destabilisation can be found in cheese making, where rennet is added to a dispersion of casein micelles in an aqueous medium ("skim milk"). Here the enzyme removes the stabilising layer of κ-casein.

For a lyophobic colloid consisting of homodisperse solid spherical particles, the structure that minimises the free energy is a close packed cluster. On the other hand, in most systems particles are actually brought together by Brownian diffusion, resulting in ramified clusters. Therefore the development of the structure in time is determined by a competition between Brownian diffusion and reorganisation of clusters to a more close packed structure. Both processes can have different time scales depending on the system used.

In the aggregating systems mentioned above, the resulting structures are often far from close packed. Figure 5.1 gives a micrograph of an aggregated system of teflon latex particles, showing a cloudy network of cross-linked ramified clusters. Here, at a relatively low volume fraction ($\varphi = 0.05$), a percolated structure is formed that cannot reorganise easily to a close packed aggregate. If bonds between particles become rigid due to ageing and sintering, reorganisation becomes impossible, and no close packed clusters will be formed.

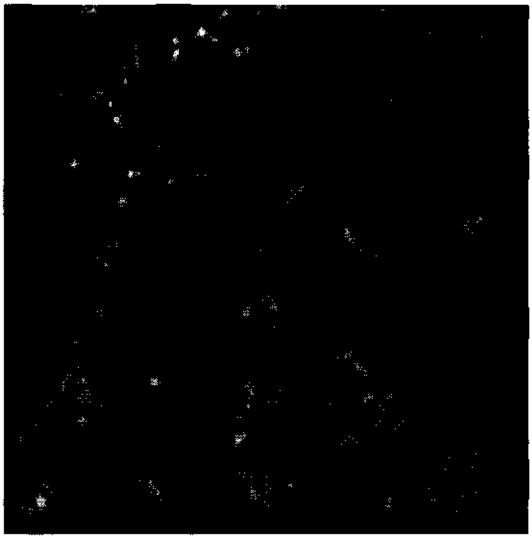

Figure 5.1: Micrograph of a casein gel; 42 by 42 μm.

An important question for many colloidal systems is which structures will be formed upon destabilisation, and what dynamics lead to them.

Destabilisation of colloids has been modelled as phase separation[1-3]. Using density functional theory, the development in time of an initially uniform density pattern can be written in the form of a diffusion equation. This diffusion equation is of no use when inhomogeneities on many length scales are to be modelled over longer time scales; a mean-field theory is inadequate for describing structures like in Figure 5.1.

Aggregation of hard-core particles to irregular structures has been studied extensively in computer simulations[4,5] (more recently[6,7]) and experiments[8-13] using fractal models to describe aggregated structures. In many simulations clusters are regarded as rigid entities, which are treated as particles with[13] a scaled diffusion and interaction behaviour. Following this scheme, aggregation by diffusion has been studied, although cluster reorganisation has been taken into account by allowing reversible aggregation[14], desorption of particles from clusters[15] or by deformations of aggregates[7]. The behavior of these systems under shear has received much attention in both theory[16], simulation[17] and experiment[18]. In this article we present the results of a Brownian Dynamics simulation of aggregating Lennard-Jones particles, in which both cluster growth and cluster reorganisation occur simultaneously, and all particles are considered explicitly. The resulting structures will be interpreted using fractal models.

5.2 Brownian Dynamics

5.2.1 The model

In the simulation we keep track of the co-ordinates of N particles in three dimensions. The Brownian Dynamics method[19] is based on the Langevin equation:

$$\boldsymbol{F}_{\text{res}} = m \cdot \frac{d^2}{dt^2} \boldsymbol{r}_i = \sum_j \boldsymbol{I}_{ij}(\boldsymbol{r}_{ij}) + \boldsymbol{R}_i + \boldsymbol{H}_i \tag{1}$$

Equation (1) gives the resulting force on particle i with mass m, where $\boldsymbol{I}$ is the force modelling interaction between particles, $\boldsymbol{R}$ the force modelling diffusion and $\boldsymbol{H}$ the force modelling hydrodynamic interactions. Equation (1) is a coupled system of differential equations that can only be solved numerically. The solution gives the particle trajectories.

We approximate hydrodynamic interactions by simple Stokesian friction (*i.e.* hydrodynamic interactions between particles are neglected):

$$\boldsymbol{H}_i = 3\pi\eta\sigma \cdot \frac{d\boldsymbol{r}_i}{dt} \tag{2}$$

with η the viscosity of the continuous phase and σ the diameter of the particles. Diffusion is modelled by a stochastic force that mimics collisions between particles and solvent molecules.

Equation (1) is solved numerically using a constant time step Δt. We choose this time step to be much larger than the relaxation time for one stochastic pulse, and neglect the inertia term, the second order term in (1). This reduces (1) to a first order differential equation:

$$\frac{d}{dt} \boldsymbol{r}_i = \frac{1}{3\pi\eta\sigma} \cdot \left[\sum_j \boldsymbol{I}_{ij} + \boldsymbol{R}_i \right] \tag{3}$$

We solve (3) using the Euler forward method[20]:

$$\Delta \boldsymbol{r}_i(t + \Delta t) = \frac{\Delta t}{6\pi\eta a} \cdot \left[\sum_j \boldsymbol{I}_{ij}(t) + \boldsymbol{R}_i(t) \right] \tag{4}$$

To avoid inaccuracy, Δt must be chosen small enough to ensure that the interaction forces do not change significantly during one integration step. Values for Δt will be given in the next section.

The stochastic displacement, which is the effect of $\boldsymbol{R}$, is tuned to obey Einstein's law for an isolated particle:

$$\Delta x_i^{\mathrm{R}}(t+\Delta t) = G_q \cdot \sqrt{\frac{2kT \cdot \Delta t}{3\pi\eta\sigma}} \tag{5}$$

G_q is a Gaussian distributed random number with unity variance. The index q indicates that different random numbers are drawn: three random numbers to calculate the stochastic displacement vector for one particle; $3N$ random numbers for the whole system in one time step. This ensures that in the absence of interactions, the displacement vectors over different particles and times are uncorrelated. In the absence of interactions, the system will asymptotically obey Einstein's law.

As the average resultant force on a particle is always zero (neglect of inertia), the energy of the particles must remain constant. This means that the energy required for the stochastic displacements is completely dissipated by friction. As both the stochastic term and the friction term in the Langevin equation describe interactions with solvent molecules, we can conclude that in the absence of interactions, also the solvent temperature T remains constant.

In the presence of interactions, the system has not only thermal but also potential energy, with total amount V_{sys}:

$$V_{\mathrm{sys}} = \sum_{i \neq j} U_{ij}(r_{ij}) \tag{6}$$

where U_{ij} is the potential energy for a particle pair as a function of their separation r_{ij}. In one interval Δt, the system will decrease V_{sys} when possible by particle displacement. Again, the decrease in V_{sys} is converted solely to friction energy, which would normally result in a rise in solvent temperature. In this simulation, however, we keep T constant, which amounts to thermostatting the sample. This is very well imaginable, as the decrease in V_{sys} is typically a slow process.

In this model interactions are described using the Lennard-Jones potential:

$$U_{ij}(r_{ij}) = 4\varepsilon \cdot \left[\left(\frac{\sigma}{r_{ij}} \right)^{12} - \left(\frac{\sigma}{r_{ij}} \right)^{6} \right] \tag{7}$$

in which ε is the attraction energy at the minimum of U_{ij} and σ is the distance at which U_{ij} changes from attractive to repulsive. The minimum in U_{ij} lies at $r_{ij} = 2^{1/6}\sigma$. The interaction force follows from the gradient of the interaction potential. Lennard-Jones particles are "soft", *i.e.* it is possible to find a pair of particles at a separation smaller than σ. We use σ as the hydrodynamic diameter in the free draining limit of (2). To increase computational speed, U_{ij} is taken zero at distances higher than $2.5\cdot\sigma$.

5.2.2 Parameters in Brownian Dynamics

In the simulation, all distances are normalised to σ and all energies to kT. Equation (5) can be written in dimensionless form:

$$\Delta\tilde{x}_i^{R}(t+\Delta t) = G_q \cdot \sqrt{\tilde{S}} \qquad (8)$$

where the tilde signifies a dimensionless quantity and $\tilde{S}$ is given by:

$$\tilde{S} \equiv \frac{2kT\cdot\Delta t}{3\pi\eta\sigma^3} \qquad (9)$$

$\sqrt{\tilde{S}}$ is the dimensionless r.m.s. particle displacement in the absence of interactions. The value of $\sqrt{\tilde{S}}$ has been 0.003 in all simulation runs; this ensures that most displacements will be small relatively to the particle size, and that interaction forces will not change too much during one integration step.

The consequences of this choice for varying particle diameters are shown in Table 5.1, for a system of polystyrene particles (density 1000 kg/m^3) dispersed in water (viscosity 10^{-3} Pas) at 298K:

Table 5.1: absolute time scales in the simulation

σ(nm)	Δt(μsec)	$\Delta t/\tau_r$
10	0.00344	618.79
10^2	3.44	6187.9
10^3	3440	61879

The third column contains the ratio of Δt and the relaxation time for one stochastic pulse:

$$\tau_{\mathrm{r}} = \frac{m}{3\pi\eta\sigma} \tag{10}$$

Table 5.1 shows that for these systems inertia effects can indeed be neglected. The only parameters left for varying are N, the number of particles in the system, $\tilde{\varepsilon}$, the well depth in (7) normalised to kT, and the volume fraction φ.

5.3 Fractal properties

Fractal structures in colloids can arise by cluster-cluster aggregation (CCA), where particles aggregate to clusters, which then aggregate similarly on a larger length scale. A system undergoing CCA consists of clusters that are fractals, and can be characterised by a fractal dimensionality d_{f} and a proportionality constant $\tilde{n}$:

$$n(r) = \tilde{n} \cdot \left(\frac{r}{\sigma}\right)^{d_{\mathrm{f}}} \tag{11}$$

where $n(r)$ is the number of particles in one cluster of radius r. The fractal dimensionality characterises the factor by which $n(r)$ increases upon an increase in cluster size. The smaller d_{f}, the more ramified clusters become as they grow. For a system of fractal aggregates, $n(r)$ can also be interpreted as the average number of particles within a test-sphere of radius r. When r is in the fractal scaling region, equation (11) holds.

CCA has been studied extensively by computer simulation[4,5]; the resulting clusters show universal fractal behaviour with a d_{f} of 1.75 at large aggregation probability (diffusion limited aggregation) or 2.0 at small aggregation probability (reaction limited aggregation).

To measure the fractal properties of our results, we study the integrated pair correlation function:

$$n_{\mathrm{c}}(r) = 4\pi\rho_0 \int_0^r l^2 g(l)\,dl \tag{12}$$

$n_{\mathrm{c}}(r)$ is the average number of particles within range r of another particle.

We measure d_{f} by identifying a linear region in a double logarithmic plot of $n_{\mathrm{c}}(r)$, and applying a least-squares fit to this region. This is equivalent to studying the scaling of the pair correlation function[4], but tends to smooth out oscillations in $g(r)$. At large length scales $n_{\mathrm{c}}(r)$ is only determined by the overall volume fraction: $g(r)$ then equals 1 and d_f becomes 3. We will call this the homogeneous scaling region.

For colloidal aggregates, the fractal scaling region will also have a lower bound r_0, typically of the order of the particle size. We can include this lower bound in the description of $n(r)$ by assuming that on length scales equal to and larger than r_0, the aggregate structure is fractal; while below r_0 the aggregate structure is closely packed. This simplification will serve as a first approximation in determining values for r_0. The first assumption can be written as:

$$\frac{n(r)}{n_0} = \left(\frac{r}{r_0}\right)^{d_f} \tag{13}$$

where a cluster of radius r_0 contains n_0 particles. The second assumption can be written as:

$$n_0 = 8\varphi_{cp} \cdot \left(\frac{r_0}{\sigma}\right)^3 \tag{14}$$

in which φ_{cp} is the volume fraction of close packing. Substitution of (11) and (14) in (13) gives an expression for $\tilde{n}$:

$$\tilde{n} = 8\varphi_{cp} \cdot \left(\frac{r_0}{\sigma}\right)^{3-d_f} \tag{15}$$

from which we see that $\tilde{n}$ is determined by both r_0 and d_f. To clarify this, we give an example of values for $\tilde{n}$ and r_0 for three deterministic fractals in two dimensions. All fractals have d_f=ln5/ln3, only the backbone is different:

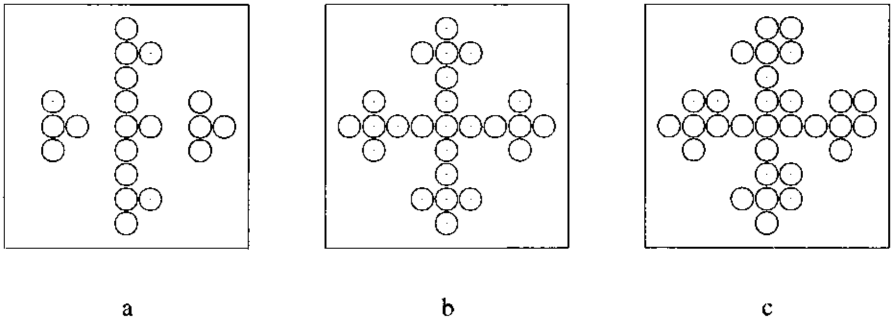
a b c

Figure 5.2: deterministic fractals

In figure 5.2 only a small part of the fractals is shown; the rest of the fractal repeats this part self-similarly. Note that Figure 5.2a constitutes a fractal object, even if it does not form a connected cluster. By writing $n(r)$ as a series, $\tilde{n}$ can be easily obtained numerically. r_0 is calculated from $\tilde{n}$ using (15), assuming φ_{cp} to be 1. The results are given in table 5.2:

Table 5.2: backbone parameters for fractals of Figure 5.2

	$\tilde{n}$	r_0 / σ
a	2.208	0.329
b	$2.761 = 2^{d_f}$	0.500
c	3.313	0.703

Here we see that our choice for φ_{cp} gives for case b the value for r_0 we would expect intuitively: the particle radius. Both $\tilde{n}$ and r_0 quantitatively reflect the differences in backbone, regardless the size of the fractal.

5.4 Results and discussion

5.4.1 Fractal results

An example of an $n_c(r)$-plot for $\varphi = 0.13$ and $\varepsilon = 2$ is given in Figure 5.3. The particle volume fraction φ is calculated using $2^{1/6}\sigma$ as the hard sphere diameter.

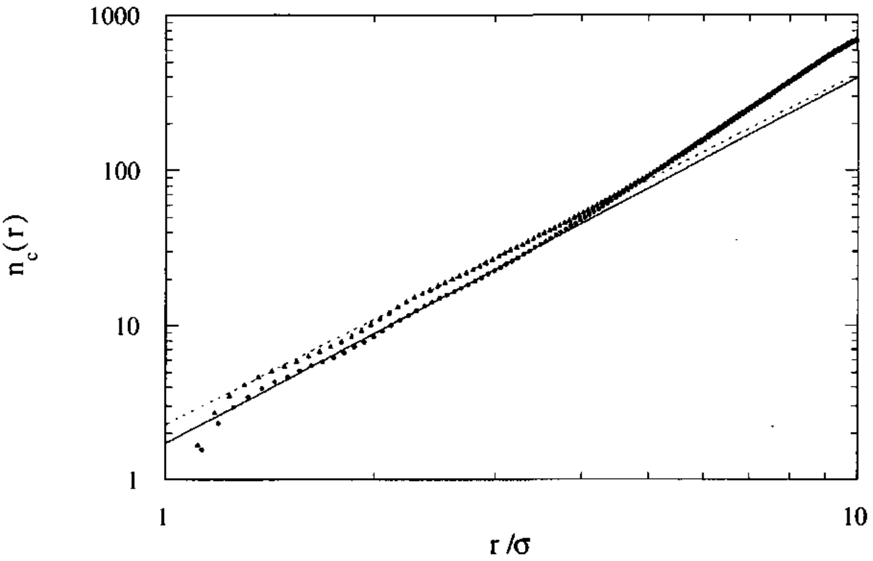

Figure 5.3: $n_c(r)$-plot of an aggregating system of 1000 particles.
Dots: after 100,000 iterations; triangles: after 350,000 iterations.

In Figure 5.3 we see that the fractal scaling region is very small. For this system the homogeneous scaling region already sets in at 4 to 5 particle diameters, which makes a least-squares fit to some extent arbitrary and the scaling results no more than semi-quantitative. The oscillations in $n_c(r)$ at small r are caused by excluded volume effects. The fractal scaling region grows in time.

From Figure 5.3 it follows that the proportionality constant $\tilde{n}$ increases with time. Equation (15) shows that we can interpret an increasing $\tilde{n}$ as an increase in size of the close packed building blocks of fractal clusters, *i.e.* compactification.

In evaluating $\tilde{n}$ for our simulation, we have to correct for using the Lennard-Jones diameter σ instead of the distance of lowest U_{ij}, $2^{1/6}\sigma$. Hence we use for φ_0 in (15) the volume fraction of f.c.c. close packed particles, 0.76, divided by $\sqrt{2}$.

In Figure 5.4 and 5.5 we show the results for d_f and r_0 for three volume fractions. In all cases the number of particles in the simulation was 1000.

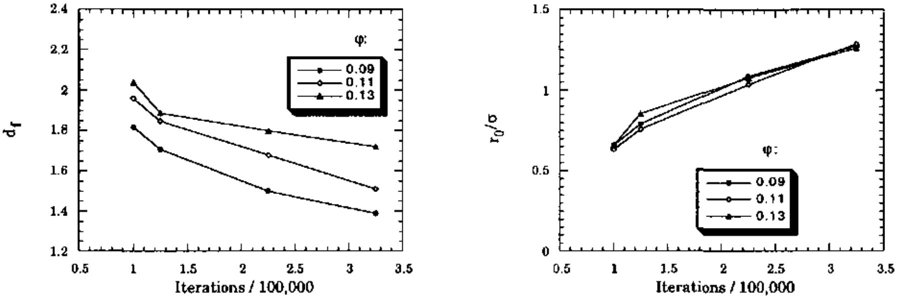

Figure 5.4: fractal parameters for $\varepsilon=4$

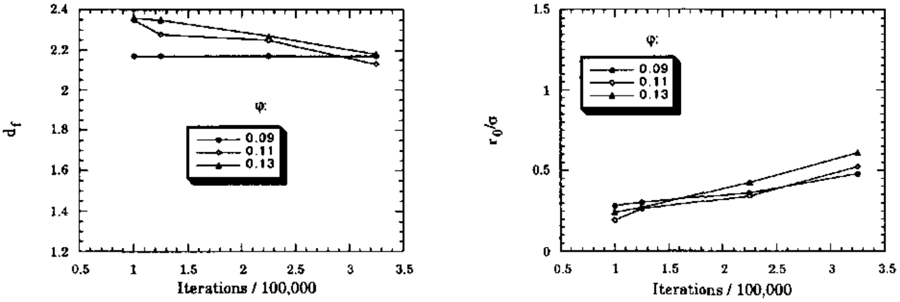

Figure 5.5: fractal parameters for $\varepsilon=2$

From Figures 5.4 and 5.5 it is clear that there is no universal fractal behaviour in the aggregated systems studied here. Generally, d_f decreases with time, indicating more string-like clusters. Also r_0 increases with time, indicating compactification.

The values of d_f and r_0 depend on both volume fraction and well depth. Compared to Figure 5.4, d_f in Figure 5.5 starts at a higher value and decreases more slowly; r_0 in Figure 5.4 starts at a higher value than in Figure 5.5 and increases faster.

5.4.2 Discussion: higher volume fractions

The simulated systems with φ higher than 0.09 form percolated clusters. An example of such a cluster is given in figure 5.6a, where only the particles belonging to the cluster are shown. Compactification in time causes percolating clusters to be transient. This is illustrated in Figure 5.6b, where compactification has caused a branch in the largest cluster to break. The largest cluster still percolates; after more iterations we find that percolating clusters break up into loose clusters. The reorganisation we see in Figure 5.6 is in accordance with a decreasing d_f and an increasing r_0.

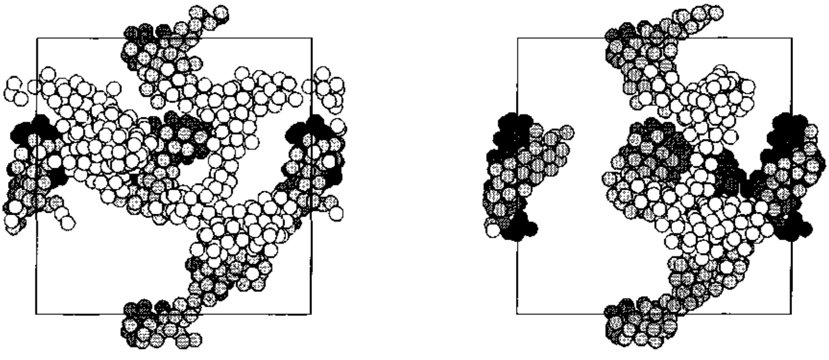
a
b

Figure 5.6: Largest cluster for $N = 1000$; φ=0.093; ε=4.

To understand the mechanism by which percolation occurs we studied a larger system (N=10,000) using the same parameters. After 25,000 iterations 80% of all the particles were already in one cluster. This cluster is drawn in Figure 5.7a. It appears that the system is separated into connected regions with high particle concentration (the cluster) and low particle concentration (voids). Figure 5.7a somewhat resembles the initial structure of phase-separating liquids[1], in which both phases form percolated networks.

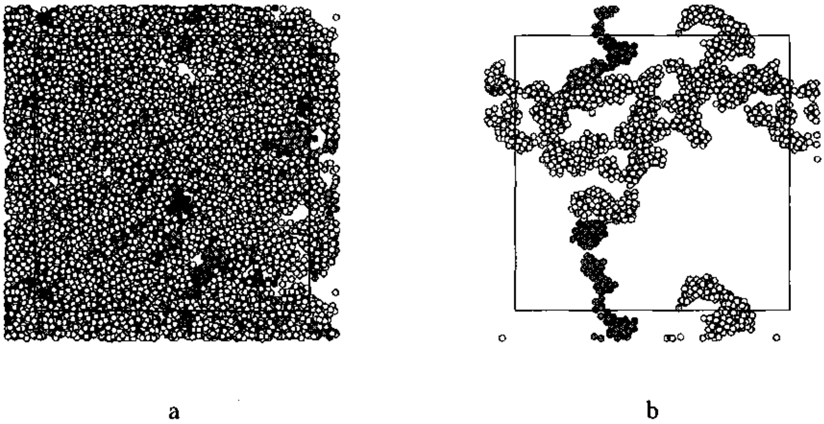

a b

Figure 5.7: Largest cluster for $N = 10{,}000$; φ=0.093; ε=4.

In the simulation, the number of particles contained in this cluster decreases with time. After 200,000 iterations the largest cluster contains only 10% of all the particles. The resulting cluster, drawn in Figure 5.7b, has become more compact at small length scale, but has retained its percolative properties. From Figure 5.7a to Figure 5.7b the cluster has compactified significantly, leaving thin branched strands between larger voids.

We find that a greater well depth merely seems to speed up the processes described above. At high ε a percolated cluster is formed faster, but reorganisation is also faster (though not necessarily in the same proportion). At lower ε the clusters look less closely packed. At ε of order kT we observed no percolation in these systems.

For the percolated systems we have calculated the pressure in the system[20]. We found $(PV/NkT)-1$ typically to be of order -10^{-7}, implying a very small underpressure caused by the network pulling on itself. To investigate directional effects we calculated the stress tensor: the stress contribution of the non-diagonal terms was about 2% of the contribution of the diagonal terms, and positive. None of these results indicate percolation being an artefact of the simulation.

5.4.3 Lower volume fractions

For volume fraction 0.074 we both start and end up with loose, non-percolating clusters. At well depth $\varepsilon = 2$ one cluster was found with a linear shape, as given in Figure 5.8.

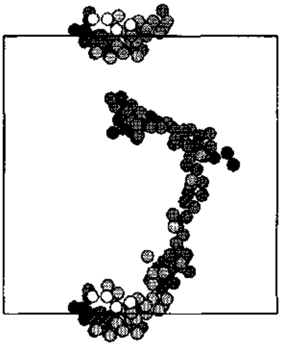

Figure 5.8: Largest cluster for $N = 1000$; φ=0.074; ε=2.

Closer inspection of the simulation data showed that this cluster was formed by aggregation of several smaller clusters. The formation of this strand-like cluster differs from that described in the previous section. Here the number of particles contained in the largest cluster increases with time.

Like in the previous section, a larger ε leads to more closely packed clusters. At $\varepsilon = 4$, we only find small compact clusters with a variety of elongated shapes, which are probably the effect of rotational diffusion.

5.5 Conclusions

For aggregating Lennard-Jones systems we find percolating networks at volume fractions above φ=0.07. These networks appear to be formed by reorganisation of large aggregates, during which branched strands are formed with voids in between. During this reorganisation, the number of particles in the largest cluster decreases. Fractal analysis gives non-universal results, which is not surprising as the mechanism of aggregation differs from CCA: both diffusion and reorganisation determine the aggregated structure. Still, scaling regions are found which may be of importance to experimentalists.

At lower volume fractions aggregation of clusters has been observed, but no percolating networks have been found. Apparently, the region in which percolating structures are formed as described is bounded by a lower volume fraction; below this bound there is a competition between cluster growth and cluster reorganisation, which the latter wins in most of the simulations. However, it is very likely that there is a region in which cluster growth prevails. If we denote such a region by CCA, the region of loose clusters by L and the percolated region by P we can sketch a diagram in parameter space, which is done in Figure 5.9:

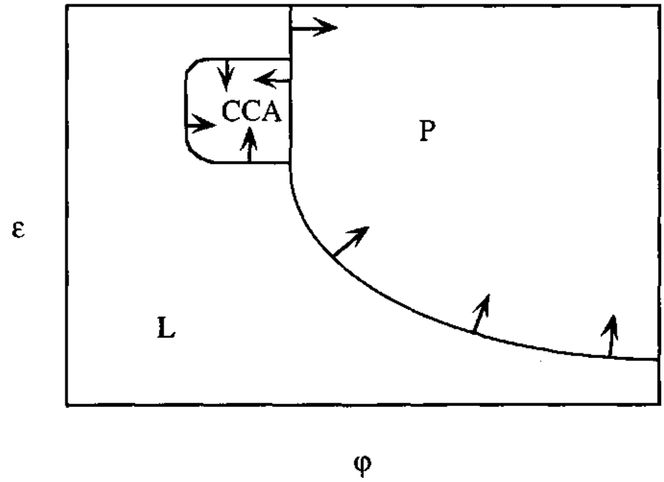

Figure 5.9: Regions in parameter space, all units arbitrary

The diagram drawn is not a phase diagram, as all structures are transient due to reorganisation. This is indicated by arrows showing how the "coexistence lines" will advance in time. In the P-region, the attractive interaction forces cause in time both formation and fracture of percolating clusters.

The Lennard-Jones potential strongly favours reorganisation, as it has a very broad interaction range. More realistic (*i.e.* short-range) interaction potentials will drastically alter the diagram. Also, in real systems, roughness of particles and sintering can freeze in structures. However, the notion of different mechanisms to obtain percolated structures (CCA and P) helps to understand the structures that can be expected at different volume fractions and interaction potentials. A computer simulation where particles are considered explicitly is necessary to sample other regions in the "phase diagram" than the CCA-region. Our next aim is to use Brownian Dynamics to simulate systems with short-range potentials, and to include effects of sintering.

Literature

[1] J. W. Cahn, *J. Chem. Phys.* **42,** 93 (1965).

[2] H. Löwen, *Phys. Rep.* **337,** 249 (1993).

[3] W. Li and J. C. Lee, *Physica A* **202,** 165 (1993).

[4] T. Vicsek, *Fractal growth phenomena*, second ed. (World Scientific, Singapore, 1992).

[5] P. Meakin, in *Phase transitions and critical phenomena*, Vol. 12, edited by C. Domb and J. L. Lebowitz (Academic Press, New York, 1987).

[6] P. Meakin, *J. Colloid Interface Sci.* **134,** 235 (1990).

[7] H. F. van Garderen, W. H. Dokter, T. P. M. Beelen, R. A. van Santen, E. Pantos, M. A. J. Michels, and P. A. J. Hilbers, *J. Chem. Phys.* **102,** 480 (1995).

[8] D. A. Weitz and M. Oliveira, *Phys. Rev. Lett.* **52,** 1433 (1984).

[9] G. Dietler, C. Aubert, and D. S. Cannell, *Phys. Rev. Lett.* **57,** 3117 (1986).

[10] P. W. Rouw and C. G. de Kruif, *Phys. Rev. A* **39,** 5399 (1989).

[11] L. G. B. Bremer, B. H. Bijsterbosch, P. Walstra, and T. van Vliet, *Adv. Coll. Interf. Sci.* **46,** 117 (1993).

[12] M. Carpinetti and M. Giglio, *Adv. Coll. Interf. Sci.* **46,** 73 (1993).

[13] P. W. Zhu and D. H. Napper, *Phys. Rev. E* **50,** 1360 (1994).

14 M. Kolb, *J. Phys. A: Math. Gen.* **19,** L263 (1986).

15 W. Y. Shih, I. A. Aksay, and R. Kikuchi, *Phys. Rev. A* **36,** 5015 (1987).

16 A. A. Potanin, *J. Chem. Phys.* **96,** 9191 (1992).

17 A. H. L. West, J. R. Melrose, and R. C. Ball, *Phys. Rev. E* **49,** 4237 (1994).

18 R. de Rooij, D. van den Ende, M. H. G. Duits, and J. Mellema, *Phys. Rev. E* **49,** 3039 (1994).

19 J. M. van der Veer, Ph.D. Thesis, University of Twente, The Netherlands, 1992.

20 M. P. Allen and D. J. Tildesley, *Computer simulation of liquids* (Oxford University Press, Oxford, 1993)

6. Brownian Dynamics simulation of aggregation in interacting systems: shorter ranged potentials

6.1 Introduction

In Chapter 2, we have developed a model describing particle gelation as a balance between phase separation and fractal cluster growth. A gel or a gelling system is described by the fractal dimensionality d_f, a number that characterises fractal growth, and the length scale r_0 up to which phase separation has succeeded. It is important to understand which characteristics of the aggregating system influence the "balance parameters" d_f and r_0 at a given time. In Chapter 5, Lennard-Jones particles at high volume fraction were studied. It was found that small length scale compactification in a percolated network caused an increasing r_0 and a decreasing d_f. The rate by which the two parameters change is determined by the LJ potential well depth ε.

This simple conclusion could be drawn because of the simplicity of the system. At high volume fractions a percolated network is formed rapidly. The long range of the Lennard-Jones potential favours percolation: when ε is large enough all particles are already within interaction range (attractive energy $\geq kT$) from the very beginning. Lennard-Jones particles can roll freely over each other's surfaces, causing small length scale compactification of clusters. Therefore the dominating process in these systems is small length scale compactification of a percolated network.

For other systems, other processes or a combination of processes may be relevant. In this chapter we will simulate systems that in terms of potential range are more related to aggregating colloids than the Lennard-Jones particles. For the latter the attraction range is approximately 2 particle diameters, which is rather uncommon for colloidal particles. We now perform a simulation with a shorter ranged potential, which is a step forward to more realistic, *i.e.* more complicated systems. We expect that a smaller potential range will decrease the reorganisation rate, so the balance between fractal growth and phase separation will be less dominated by the former. As a consequence, other processes than the reorganisation of an already formed network are possible.

We will assess the fractal parameters d_f and r_0 as a function of volume fraction φ and potential well depth ε. The simulation method used is Brownian Dynamics; for background information on this method and to the calculation of the fractal parameters we refer to Chapter 5 section 2. As a bridge with equilibrium thermodynamics we will also investigate the role of the well depth ε using perturbation theory.

6.2 Short range potential

In Brownian Dynamics, we displace a particle at random and calculate the interaction force afterwards. To prevent instabilities in this algorithm, it is favourable to use a continuous potential like the Lennard-Jones potential. Moreover, the r.m.s. displacement Δ, which limits the simulation speed, should be small enough to prevent the occurrence of very large forces. For the Lennard-Jones potential, Δ is tuned to the steepest part of the potential, which is the core repulsive part.

A short-range attractive potential U_{sr} will automatically lead to larger forces, and therefore the need to decrease Δ; the latter is obviously unfavourable in terms of simulation speed.We have chosen to maintain the Lennard-Jones potential up to its minimum ($r = 2^{1/6}\sigma$), and to maintain the value for Δ used in the Lennard-Jones systems. In this way we prevent the occurrence of very large repulsive forces. For larger distances, we use a different functionality to described short-ranged attraction. In doing so, the combined potential must be continuous up to its first derivative to prevent discontinuities in the interparticle force. The required potential must be $-\varepsilon$ at $r = 2^{1/6}\sigma$ and for larger distances increase to 0 at some tunable range. This can be achieved using the following potential:

$$\frac{U_{\mathrm{sr}}(r_{\mathrm{rel}})}{\varepsilon \cdot c_0} = c_1 + c_2 \cdot r_{\mathrm{rel}}^{-12} - c_3 \cdot r_{\mathrm{rel}}^{-2} + c_4 \cdot \exp(-r_{\mathrm{rel}}) \qquad (1)$$

with c_0 through c_4 dimensionless constants and r_{rel} a dimensionless distance. Although (1) is reminiscent of the DLVO-potential, the purpose of the potential (1) is not to reproduce DLVO-interactions between colloidal particles. The functionality is used merely because it allows us to design a potential without risk of instabilities from core repulsion forces. Using the following values for constants c_1 through c_4

$$c_1 = \frac{2047}{531441} \quad c_2 = 1 \quad c_3 = \frac{2048}{19683} \quad c_4 = \frac{4096}{531441} \cdot \exp(3) \qquad (2)$$

the potential (1) is always 0 for r_{rel}=3. To combine this potential with the Lennard-Jones potential, we define r_{rel} as follows:

$$r_{\mathrm{rel}} = k \cdot (\frac{r}{\sigma} - 1) \qquad (3)$$

The dimensionless parameter k in (3) now determines the range of the combined potential. Using the values $k = 13.605$ and $c_0 = 456.804$, which were determined numerically, we obtain a potential with a minimum of $-\varepsilon$ at $r = 2^{1/6}\sigma$. The combined potential and force are shown in Figure 6.1:

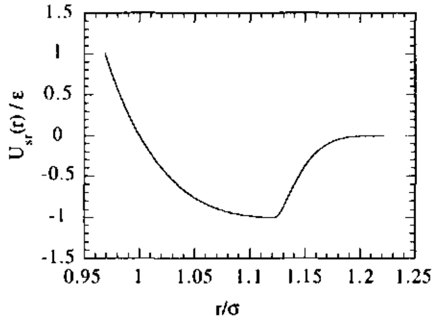

Figure 6.1a: Interaction potential

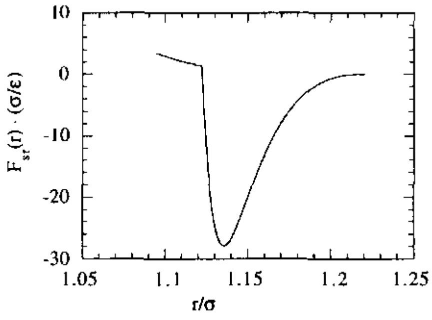

Figure 6.1b: Interaction force

The combined potential becomes 0 at $(r/\sigma) = (3/k) \approx 1.22$; for larger distances we simply set $U_{\rm sr}$=0. Some instabilities in attractive forces may arise, but, as can be seen in Figure 6.1b, the repulsive part of the potential will lead to a gentle relaxation of these forces.

A potential with an even shorter range, which we shall call $U_{\rm vsr}$, can be obtained by using a value of 100 for the range parameter k in (1). In order to obtain a continuous force, we must now shift the Lennard-Jones part of the potential. We define the "shift distance" $r_{\rm sh}$ as the distance at which $U_{\rm vsr}$ equals $-\varepsilon$. Numerically, we find $r_{\rm sh} \approx 1.01659\sigma$. The shifted Lennard-Jones potential then becomes:

$$U_{\rm LJs}(\frac{r}{\sigma}) = U_{\rm LJ}(\frac{r}{\sigma} + 1 - \frac{r_{\rm sh}}{\sigma}) + U_{\rm vsr}(\frac{r_{\rm sh}}{\sigma}) \tag{4}$$

The combined potential now becomes $U_{\rm LJs}$ up to $r_{\rm sh}$ and $U_{\rm vsr}$ at larger distances. $U_{\rm vsr}$ becomes 0 at $r = 1.03\sigma$; for larger distances the combined potential is set 0. The result is given in Figure 6.2:

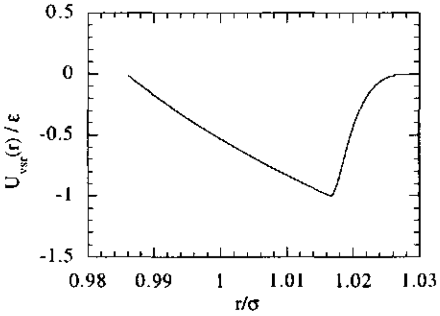

Figure 6.2a: Interaction potential

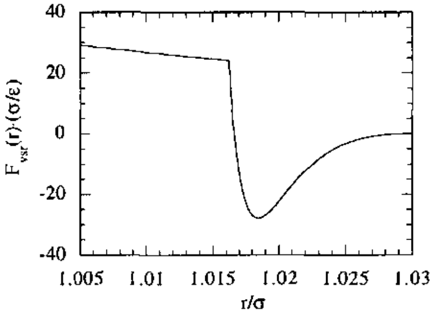

Figure 6.2b: Interaction force

It should be noted that r_{sh} does not represent the minimum of the combined potential, nor is the force $F_{\mathrm{vsr}}(r_{\mathrm{sh}})$ equal to 0. The true minimum lies at $r \approx 1.01666\sigma$ with an interaction potential of -1.0013ε. As these differences are very slight we take the potential well depth to be ε.

For all systems, the volume fractions φ are calculated by taking the position of the minimum in the interaction potential as the hard-sphere diameter.

6.3 Results and discussion

6.3.1 Short range potential

The development of the fractal parameters in time for all systems is given in Figures 6.3, 6.4 and 6.5. A vertical dotted line indicates the moment at which percolation was first detected.

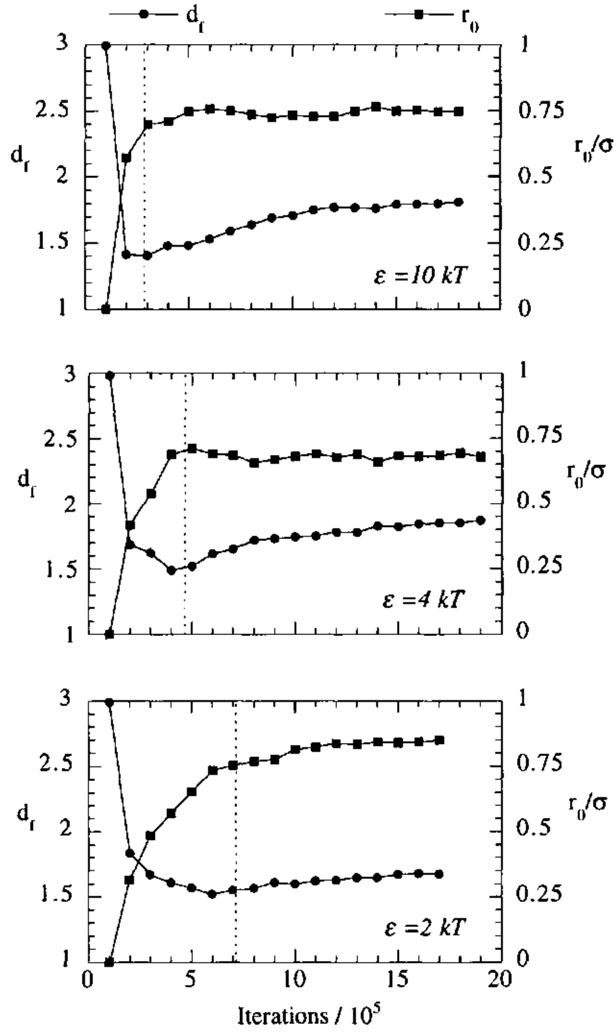

Figure 6.3: Fractal parameters for φ=0.074

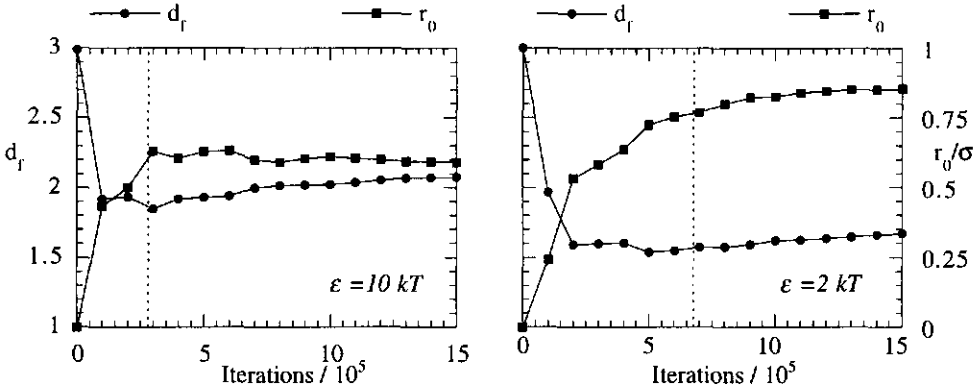

Figure 6.4: Fractal parameters for φ=0.11

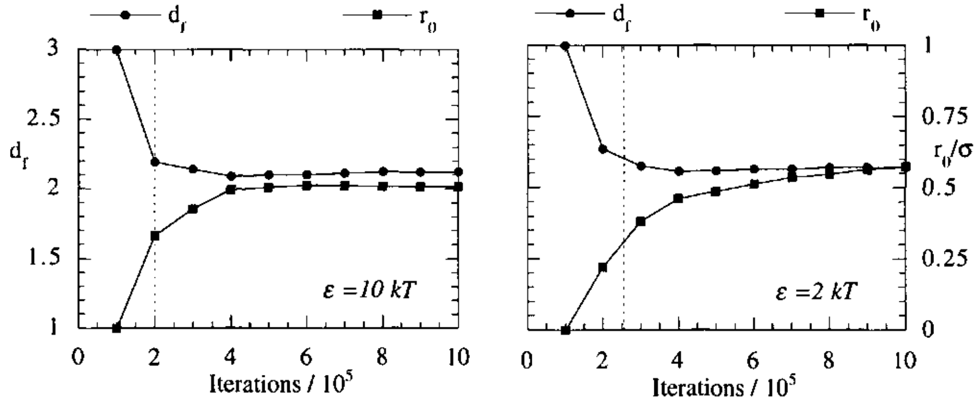

Figure 6.5: Fractal parameters for φ=0.15

From Figure 6.3 we see that the fractal dimensionality first decreases and then slowly increases. The value eventually reached here is close to the DLCA-limit, but the development in time shows that this value is not uniform for the whole aggregation process. The first part, where d_f decreases from 3 to a significantly lower value, is difficult to interpret; in this stage the fractal dimensionality describes a mixture of non-connected small clusters rather than a network. The low values reached near the percolation point, however, suggest that the final network is formed by aggregation of very ramified ($d_f \leq 1.5$) clusters.

Another observation is that in most systems and especially for large ε, a plateau value in both d_f and r_0 appears to be reached. This is in contrast with the results for the Lennard-Jones particles in Chapter 5. Generally, we can place the results in two categories. This can be done in two ways, either by using the plateau value of d_f and r_0 or by using their development in time.

For the plateau values we can distinguish between:

Ia. a small d_f (1.7) and a large r_0 (0.8σ) (φ=0.074; ε=2 kT for φ=0.11);

Ib. a large d_f (2.1) and a small r_0 (0.6σ) (φ=0.15; ε=10 kT for φ=0.11);

For the development in time we can distinguish between:

IIa. d_f increasing with time from the percolation point onwards (φ=0.074; φ=0.11);

IIb. d_f decreasing with time from the percolation point onwards (φ=0.15);

As the increase of d_f for the two systems at φ=0.11 is not very pronounced, we can merge the two categories. This results in the following rough distinction:

a. a small d_f (1.7), a large r_0 (0.8σ) and an increasing d_f (φ=0.074; ε=2 kT for φ=0.11);

b. a large d_f (2.1), a small r_0 (0.6σ) and a decreasing d_f (φ=0.15; ε=10 kT for φ=0.11);

These results can be explained in terms of aggregation pathways. An increase in d_f can be explained by interpenetration of clusters; a decrease in d_f, as in Chapter 5, can be explained by reorganisation of a connected network. In the first case, cluster interpenetration leads to a net transport of particles from the homogeneous region to the fractal scaling region. In the second case reorganisation (reflected in an increasing r_0) is obtained by transporting particles from the fractal scaling region to smaller length scales. An increase in d_f is possible when clusters are able to grow undisturbed by reorganisation, and then interpenetrate. For ramified clusters, interpenetration can also continue after percolation. It is not surprising that category a is found at lower φ (more room for cluster growth) and lower ε (more opportunity, yet a smaller driving force for reorganisation). At a large φ and large ε, percolation is obtained quickly, leaving the system no other option than reorganisation of a connected network, which amounts to category b.

The end values of d_f and r_0 are not easily explained. Both the strong initial decrease in d_f and the strong initial increase in r_0 occur before percolation, making it impossible to make a connection with the two described aggregation pathways. The large value of r_0 for category a can be explained by a pre-aggregation stage (see Chapter 4): in the time available for cluster growth, there is also some opportunity for reorganisation. The two pathways (interpenetration and reorganisation) can indeed occur in the same system on different timescales, which illustrates that it is very difficult to attribute a specific aggregation pathway to a value of d_f measured at a certain time.

6.3.2 Very short range potentials

In order to perform numerically stable simulations, the r.m.s. random displacement Δ had to be made ten times smaller for the U_{vsr}-systems. As these simulations require very much time to perform, only two preliminary results are shown in Figure 6.6, both at ε=10.

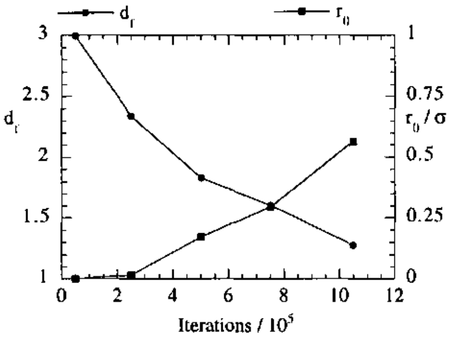

Figure 6.6a: Fractal parameters; φ=0.028

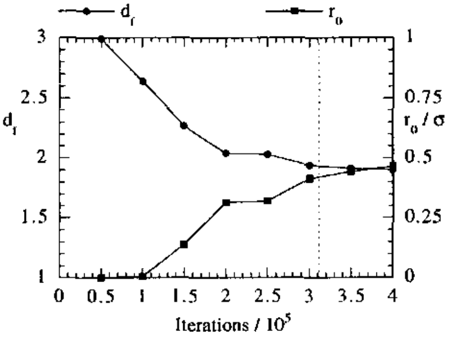

Figure 6.6b: Fractal parameters; φ=0.083

In Figure 6.6, the number of iterations has been scaled yielding a time scale comparable to that of all other systems in this chapter.

A low volume fraction, φ=0.028, showed a decreasing d_f accompanied by an increasing r_0. At the latest time simulated for this system, d_f=1.25 and percolation is not yet reached; this indicates loose and probably rather linear clusters. The development of the fractal parameters in time suggests, as in Chapter 5, that these clusters undergo reorganisation; apparently reorganisation still proceeds at a noticeable rate even though the range of the attractive potential is very small. This is a consequence of the particle smoothness: particles in the same cluster are always able to undergo lateral diffusion. Reorganisation caused by lateral diffusion is much slower than reorganisation caused by long range interactions (LJ systems) and is far more constrained than reversible aggregation (section 6.3.1, ε=2).

Following the aggregation pathway of cross-linking of section 6.3.1, the linear clusters may still aggregate to form a percolated network, but this may take much more simulated time.

A higher volume fraction, φ=0.083, did result in percolation. Here the results can be placed into category b of section 3.1, only with a smaller value for r_0.

6.4 Effect of potential range on critical well depth

The theory of Song and Mason[1] provides an equation of state for a molecular fluid relating the pressure (p) to the particle number density ρ ($=6\varphi/\pi\sigma^3$) and the interaction potential $U(r)$:

$$\frac{p}{\rho kT} = 1 + B\cdot\rho + \alpha\cdot\rho\cdot\left(\frac{8\cdot(8-b\cdot\rho)}{(4-b\cdot\rho)^3} - 1\right) \tag{5}$$

in which the coefficients B, α and b are given by:

$$B = 2\pi\cdot\int_0^\infty r^2(1-\exp[-U(r)/kT])\mathrm{d}r \tag{6}$$

$$\alpha = 2\pi\cdot\int_0^{r_\mathrm{m}} r^2(1-\exp[-U_0(r)/kT])\mathrm{d}r \tag{7a}$$

$$b = 2\pi\cdot\int_0^{r_\mathrm{m}} r^2\left(1-\left[(1+U_0(r)/kT)\cdot\exp[-U_0(r)/kT]\right]\right)\mathrm{d}r \tag{7b}$$

where r_m is the distance at which the potential U has its minimum ($U(r_\mathrm{m}) = -\varepsilon$) and $U_0(r)$ is defined as:

$$U_0(r) = \begin{cases} U(r)+\varepsilon & \text{for } r < r_\mathrm{m} \\ 0 & \text{for } r \geq r_\mathrm{m} \end{cases} \tag{8}$$

When the potential $U(r)$ is sufficiently attractive, a Van der Waals loop can be identified in (5) signifying a gas-liquid phase transition. For all three potentials used in this thesis (Lennard-Jones potential U_LJ, short range potential U_sr, very short range potential U_vsr) the occurrence of a Van der

Waals loop depends on the value of the potential well depth ε. The critical well depth for this phase separation ε_c, which is the minimal well depth to enable phase separation, can be calculated using:

$$\left.\frac{\mathrm{d}p}{\mathrm{d}\rho}\right|_{\varepsilon_c} = \left.\frac{\mathrm{d}^2 p}{\mathrm{d}\rho^2}\right|_{\varepsilon_c} = 0 \tag{9}$$

Equation (9) can be solved numerically for all three potentials yielding ε_c. The results are compiled in Table 6.1.

Table 6.1: critical well depths for different potentials

potential	ε_c
U_{LJ}	0.825
U_{sr}	2.262
U_{vsr}	6.497

Equation (5) only takes into account a gas-liquid phase transition. Even if ε is smaller than ε_c as calculated from (9), a gas-solid phase transition will occur at large enough volume fractions. We should therefore limit the discussion in this section to systems of volume fractions smaller than about 0.5. This still covers all systems studied in this thesis.

From Table 1 we see that when the potential range is decreased, ε_c shifts to larger values. This result can be expected: for a narrow-ranged potential, aggregation is entropically less favourable, which can only be compensated by a more favourable enthalpic (*i.e.* ε-) effect. This effect is also found experimentally for grafted silica particles in hexadecane^2: here no phase separation is detected until $\varepsilon \geq 4kT$.

For the LJ potential, ε_c is less than kT, which means that aggregation at a slightly larger ε can occur by a reversible pathway. For very narrow ranged potentials like U_{vsr}, however, ε_c is significantly larger than kT, which means that aggregation at a slightly larger ε will lead to the formation of clusters with a significant lifetime. Especially for these systems, ε will have the ambivalent role, as described earlier, of both promoting aggregation (*i.e.* the formation of more bonds) globally and inhibiting it locally by irreversible cluster formation. In other words, when one wants to inhibit reorganisation and promote cluster growth, one should use a colloid with strong, but very short ranged attractive interactions.

A number of systems in this chapter are indeed simulated using an ε smaller than ε_c. In these systems aggregation, but also reorganisation is clearly visible. It should be noted that Equation (5) can only be used to predict global stability or instability against phase separation. Local effects or kinetics are not taken into account. Nevertheless, in the simulations the effect of potential range on the observed aggregation pathways is considerable, as can be inferred from the differences between fractal results from Chapter 5 and Chapter 6.

6.5 Conclusions

Brownian dynamics simulations of interacting particles with a shorter potential range (as compared to the Lennard-Jones potential) enables a more complete study of aggregation pathways. The results are by no means universal: a time-dependency of the fractal parameters was found with both increasing and decreasing fractal dimensionalities. From these results two aggregation pathways are suggested: cross-linking (increasing d_f) and local compactification of a connected network (decreasing d_f). For the LJ potential, the aggregation was dominated by the latter; by decreasing the potential range this balance becomes more subtle. As the two pathways can occur in the same system on different timescales, it is very difficult to attribute a specific aggregation pathway to a value of d_f measured at a certain time. Studying the development in time is a more reliable method.

Reorganisation of clusters occurs at a lower rate when the potential range is decreased. A large potential well depth ε both promotes reorganisation and inhibits it because of irreversible clustering. A thermodynamical analysis shows that this effect will become more pronounced for shorter ranged potentials.

Literature

[1] Y. Song and E. A. Mason, J. Chem. Phys. **91**, 7840 (1989).

[2] P. W. Rouw, *Ph.D. Thesis*, University of Utrecht , The Netherlands, 1988.

7. General conclusions and outlook

7.1 Picture of a particle gel

For a suspension of particles, there are (amongst others) two physical pathways known from the literature that result in a connected network of particles. The first is given by the DLCA scheme and related schemes, the second is that of a dynamically congealed suspension, or a colloidal glass. The two pathways are extremes: DLCA can be regarded as the limit at small volume fractions (there needs to be enough space for successive cluster-cluster aggregation), formation of a colloidal glass is only relevant at very large volume fractions (a large volume fraction is needed for particles to obstruct their own dynamics). Both mechanisms are affected by any reorganisation before and after the formation of a network.

In this thesis we have studied gelation at volume fractions in between these two extremes where neither of them gives a complete description. Moreover, we have looked at various rates of reorganisation.

- Colloidal model systems with volume fractions between 0.01 and 0.1 and with reorganisation occurring in the early stage of aggregation (Chapter 4);

- Simulated model systems with volume fractions between 0.074 and 0.15 with reorganisation occurring at all stages (Lennard-Jones particles in Chapter 5, short range attractive particles in Chapter 6);

These systems all show some degree of fractal scaling like in DLCA-type models, but with different and varying scaling exponents d_f. When the clusters are studied more carefully at small length scales, we see that they are often built of units larger than a single particle.

Simulated Lennard-Jones particles quenched rapidly at strong attractive interactions do not readily phase separate, as is to be expected from the phase diagram; instead they form gels, possibly as a transient state. These "argon gels" exhibit fractal scaling, and look like frozen spinodal decomposition patterns.

This thesis has resulted in a modified physical picture of colloidal gelation, which has enabled us to understand complicated systems better. In this picture, colloidal gelation is the result of a competition between fractal cluster growth driven by Brownian motion and cluster compactification driven by attractive interactions between particles. For cluster compactification, we use the picture of colloidal phase separation where a suspension with strong attractive interactions can lower its free energy by forming zones of high volume fractions. The result has been applied directly in experiments: we have measured both d_f and the length scale r_0 up to which zones of high volume fraction are formed. We consider this an important step forward from only measuring scaling exponents; as shown in Chapter 4, an identical d_f does not necessarily mean an identical structure.

7.2 Confocal microscopy

We have used CSLM as a tool to study colloidal gels. Although processing of the structural data proved to be difficult, the method provides a very useful tool: without extensive preparation of a colloidal gel its 3D structure could be studied at room temperature. Imaging of complex structure with a microscope has the advantage that both the overall structure and the local details are accessible, and that pictures can be compared by eye. For comparison, information derived from light or x-ray scattering is available in the Fourier domain, which requires a more elaborate interpretation.

Confocal fluorescence microscopy requires a refractive index matched colloidal model system. In this thesis a new and very promising system of PFA teflon latex particles in water is used that fulfils this requirement. Further research on the synthesis of this model system, and on covalently binding fluorochromes to the particles, may well enhance its potential as a model system for CSLM.

Confocal microscopy is especially useful for measuring the parameter r_0. To correctly measure both d_f and r_0, it is essential that the effect of microscope resolution is treated properly. With the deconvolution procedure described in Chapters 3 and 4, this thesis presents a good method to do this. A new and simple way to calculate the 3D Point Spread Function from laser excitation, fluorochrome emission wavelength and lens aperture is presented in Chapter 3. The principle of deconvolution was published as early as 1962; yet its use for 3D CSLM has only become possible recently because of the large computing capacity required. Although the technique can be optimised further, the deconvolution has been successfully achieved. For further research, Chapter 4 can serve as a guideline for stepwise optimisation of the analysis path. As discussed in Chapter 4, the results from the colloidal model systems do not yet give a clear picture of the dependence of the gel structure on the physical parameters of the destabilised system; much more experimental work would need to be done in this field. To identify aggregation mechanisms, it would be particularly interesting if the structure could be studied as a function of time. Using a charge coupled device (CCD) camera[1], which is in essence an array of point detectors, a micrograph can be captured instantaneously; this is much faster than capturing a micrograph through mechanical scanning.

In this thesis, deconvolution comprises a reconstruction of one 2D micrograph from a 3D data set. For the determination of d_f and r_0 a 2D micrograph suffices assuming that the structure is isotropic; the 3D data set is needed merely for the deconvolution. Using this method, a fractal characterisation, may within a few years be possible on desktop computers instead of on powerful workstations. As the capacity and computing power of workstations also grows, optimised and full 3D deconvolutions or time-dependent measurements may also become possible within a few years. Because of the rapid developments in computer science at this moment, further research in this line may be rewarding.

7.3 Computer simulations: pathways for aggregation

Brownian Dynamics simulation has been shown to be a useful tool for studying mechanisms in aggregation. The method is most suitable for studying the relaxation of a quenched non-equilibrium system, unlike for instance Monte Carlo simulations, which simply aim at obtaining equilibrium. Molecular Dynamics simulations, normally used for simulating atomistic interactions, would be very inefficient for a colloidal system at low volume fractions, as by far most of the time needed for the calculation is spent on interactions between water molecules, not between particles.

Our aim in simulating was to identify general pathways for aggregation and gelation from the simulated configurations. This is possible, as all co-ordinates of particles are known exactly at any time of the simulation.

Generally, upon varying volume fractions and interactions, we have found the following.

For all systems, the fractal parameters d_f and r_0 are time dependent The values of the fractal parameters, their rate of change and the occurrence of a platform value depend on interaction potential and volume fraction. We have found two "scenarios" in the aggregation process with an opposite effect on d_f:

1. Non-reorganising clusters cross-link to form a network, mass is transported from the homogeneous region to the scaling region; d_f increases;

2. Clusters reorganise by compactification on small length scales, mass is transported from the scaling region to the close packed region; d_f decreases.

It should be noted that both scenarios can occur in the same system on different time scales.

If there is some flexibility in clusters, or if bonds between particles are in some way reversible, then there will be not just DLCA-like cluster growth driven by Brownian motion, but also a degree of reorganisation. A combination of interaction strength and geometrical constraints will determine the degree of reorganisation and the timescales involved, which gives a non-trivial dependence on volume fraction and interaction parameters.

A clear connection with the model systems could not be made; for these systems both d_f and r_0 were significantly larger than encountered in the simulations. As to d_f, the dependency on volume fraction seen in te simulations was not found for the model systems. Time dependent effects were not studied.

The simulation method neglects hydrodynamics and can handle only 10^3 to 10^4 particles. It seems unlikely, however, that this will change the notion of reorganisation and interpenetration, and their effects on the fractal parameters. To obtain a better connection with experimental values, we suggest that the same simulation scheme be used using more complicated interaction potentials: time-dependent potentials (modelling the hydrolysis of GDL) and potentials with a repulsive barrier. A repulsive barrier will considerably slow down the aggregation process, allowing more time for reorganisation, but simultaneously taking away the tendency of the system to phase separate (*i.e.* to increase r_0). Very possibly this is the "missing link" between the simulations and the colloidal model systems.

7.4 Suggestions for further research

Relevant phenomena like reorganisation and rotational diffusion, both not contained in the DLCA-scheme, complicate the simple picture of universal fractal scaling; therefore accepting DLCA as the standard for colloidal aggregation is incorrect. This work contributes to explaining less trivial experimental results, and there are many opportunities to continue this in further research projects. The main suggestions for further research are given in sections 2, 3 and 4 of this chapter, and range from optimising the synthesis of model colloids via optimising a CSLM analysis procedure to performing more computer simulations.

An especially challenging area for further research is simulating the aggregation of attractive particles with a potential energy barrier. Such a barrier is particularly relevant to charge stabilised colloids. A modified DLCA scheme named RLCA[2] has been used to describe aggregation in these systems, with the same disadvantages as DLCA: neither rotational diffusion nor cluster reorganisation is taken into account. We expect that a better knowledge of aggregation pathways for attractive particles with a potential energy barrier, identified using Brownian Dynamics, will enable a better link with experimental systems than achieved in this thesis. A Brownian Dynamics simulation of these systems will not be simple, however, as a potential energy barrier slows down the aggregation process considerably, so either more computing power or more efficient algorithms will be necessary.

The aggregation and gelation of colloidal particles is an intriguing problem which is by no means solved. To describe a particle gel, a non-equilibrium and almost irreversible aggregation has to be combined in some way with the thermodynamic minimum free energy prediction of a phase separated system. It is unclear how this combination should be made, as the latter may never, or at least not within human time scale be reached. This type of research may be difficult, but it is also very relevant, considering the wide application range of colloidal gels. Further investigators will be rewarded with the opportunity to combine the disciplines of colloid chemistry, physics and mathematics with technological aspects in one single project.

Literature

1 T. Wilson, *Confocal Microscopy* (Academic Press, London, 1990).

2 T. Vicsek, *Fractal growth phenomena* (World Scientific, Singapore, 1992).

Summary

This thesis contains the results of a PhD-study on the structure of particle gels. Part of it is directed at a quantification of this structure from measured data, part of it at modelling the aggregation processes that lead to particle gels. Chapter 1 of this thesis is a general introduction describing the aim of this study.

Chapter 2 introduces aggregation and gelation of particles. As to the modelling of aggregation we conclude that there are two types of approach: one based on thermodynamics and one based on fractal aggregation (Diffusion Limited Cluster Aggregation or DLCA). The former is appropriate for reversible aggregation, the latter for irreversible aggregation. For all types of colloidal aggregation which are in between these two extremes, an understanding based on both approaches is needed. We use fractal aggregation models as a starting point, but recognise the importance of cluster reorganisation, which will cause gels with structures different than predicted in DLCA. As to quantification of fractal structure, a lower cutoff length scale r_0 is suggested as a valuable addition to the fractal dimensionality d_f.

Chapter 3 describes Confocal Scanning Laser Microscopy (CSLM) as a tool to study the structure of various particle gels. An in-depth optical treatment of imaging in CSLM is presented, along with a new way of image enhancement using calculated three dimensional point spread functions. It is concluded that image enhancement is essential in order to get useful results from an analysis of CSLM micrographs.

Chapter 4 shows the results on the fractal structure of particle gels derived from CSLM micrographs of colloidal model systems. It explains thoroughly the details of the image analysis procedure and identifies possible problems, most notably background intensities. From the results it appears that all fractal dimensionalities are about equal, with values larger than the DLCA limit. The values of r_0 show that there are significant differences between gel structures despite the similarities in d_f. These differences are difficult to connect with properties of the colloidal model systems. A hypothesis about a "pre-aggregation stage" is formulated which might serve as a starting point for further research.

In Chapters 5 and 6 Brownian Dynamics simulations are used as a tool for forming a better connection between aggregation and gel structure. For aggregating Lennard-Jones systems (Chapter 5) we find percolating networks at high volume fractions; these appear to be formed by reorganisation of large aggregates, during which branched strands are formed with voids in between. The gel structure is influenced by both cluster growth and cluster reorganisation; fractal analysis gives non-universal, *i.e.* time dependent results. For the Lennard-Jones potential, the aggregation is dominated by cluster reorganisation. Aggregating particles with a shorter potential range (Chapter 6) also show time dependent fractal results, but by decreasing the potential range the balance between

cluster growth and cluster reorganisation becomes more subtle. Reorganisation of clusters occurs at a lower rate when the potential range is decreased. A large potential well depth ε both promotes reorganisation and inhibits it because of irreversible clustering. A thermodynamical analysis shows that this effect will become more pronounced for shorter ranged potentials.

Chapter 7 generalises the conclusions of all previous chapters and gives suggestions for further research. All results in this thesis have used available computing resources up to the maximum. Given the ever growing computing power, significantly more sophisticated techniques for simulation or image analysis will become available within years.

The work described in this thesis has led to the following publications:

J.H.J. van Opheusden, M.T.A. Bos, "Induced flocculation of casein micelles - a Brownian Dynamics simulation on the Parsytec Gcel MPP", Future. Gener. Comp. Sy. **11** 123-133, 1995

B.H. Bijsterbosch, M.T.A. Bos, E. Dickinson, J.H.J. van Opheusden, P. Walstra, "Brownian dynamics simulation of particle gel formation: From argon to yoghurt", Faraday Discuss. **101** 51-64, 1995

M.T.A.Bos, J.H.J van Opheusden, "Brownian dynamics simulation of gelation and aging in interacting colloidal systems", Phys Rev E **53** 5044-5050, 1996

Samenvatting voor niet-vakgenoten

Gelen

Gelen zijn stoffen die voor 90% of meer uit een vloeistof, bijvoorbeeld water, bestaan, maar in hun gedrag sterk van een vloeistof verschillen. Dit gedrag wordt duidelijk wanneer men een hoeveelheid haargel op de hand deponeert. In tegenstelling tot water loopt het gel niet tussen de vingers door weg, het is zelfs tot op zekere hoogte elastisch: als men de hand een klein beetje beweegt, trilt de hoeveelheid haargel nog na. Uit hoeveel water haargel ook bestaat, dit "niet vloeien" en "elastisch zijn" doet meer aan een vaste stof dan aan een vloeistof denken. Dat verandert als men het gel onder iets grotere druk zet, bijvoorbeeld door de hand samen te knijpen: dan blijkt dat het niet meer terugveert, maar dat het gel zwicht en weer gaat vloeien.

De verklaring van dit gedrag ligt verscholen in de kleine hoeveelheid niet-vloeibaar materiaal: die vormt namelijk een doorverbonden netwerk binnenin de watermassa en daarmee de fundering van het gel. Het gel staat of zwicht met dit netwerk: als het netwerk scheurt, dan zwicht het gel. Hoeveel kracht ervoor nodig is om dat te bereiken hangt af van de stuktuur van het netwerk: de bouwstenen waaruit het bestaat en op welke manier deze bouwstenen in de vloeistof zijn geplaatst.

Dit proefschrift gaat over de struktuur van gelen waarvan de fundering bestaat uit een netwerk van kleine deeltjes. Een voorbeeld van kleine deeltjes is te vinden in melk: melk is een vloeistof waarin onder andere eiwitrijke deeltjes van circa 50 nanometer ronddrijven. Bederf, maar ook het toevoegen van stremsel in de kaasmakerij, leiden ertoe dat deze deeltjes aan elkaar gaan (en blijven) kleven, het resultaat is een netwerk van deeltjes, een deeltjesgel, dat net als haargel in staat is om meer dan 90% water overeind te houden.

Aggregatie

In het algemeen wordt het proces waarbij deeltjes (of molekulen) aan elkaar gaan kleven aggregatie genoemd. Gelering is een bijzondere vorm van aggregatie met als eindresultaat een gel. Fysici en kolloïdchemici houden zich al enige tijd bezig met aggregatie en gelering van deeltjes. Het goed begrijpen van dit proces is nuttig bij het maken van kaas maar ook bij het maken van zeolieten (poreuze korrels die te vinden zijn in waspoeder), beton en chocolademelk. Hierbij helpt het als men zich iets bij gelering kan voorstellen; een mogelijke voorstelling van gelering wordt ook wel een model voor gelering genoemd. Eén model voor gelering luidt als volgt: losse deeltjes in een vloeistof bewegen, dit wordt ook wel Brownse beweging genoemd. De beweeglijke deeltjes kleven aaneen tot clusters van deeltjes en de beweeglijke clusters kleven op dezelfde wijze aaneen tot grotere clusters. Dit proces, schematisch weergegeven in de vorm van een "stripverhaal" op de volgende pagina, gaat door tot alle deeltjes aan elkaar vast zitten. Het "stripverhaal" beschrijft 125 aggregerende deeltjes in een vierkant gevuld met vloeistof. Het linkerplaatje geeft de beginsituatie van losse deeltjes; via twee tussenstadia wordt uiteindelijk een grote cluster gevormd die alle zijden van het vierkant raakt, met andere woorden: een doorverbonden netwerk.

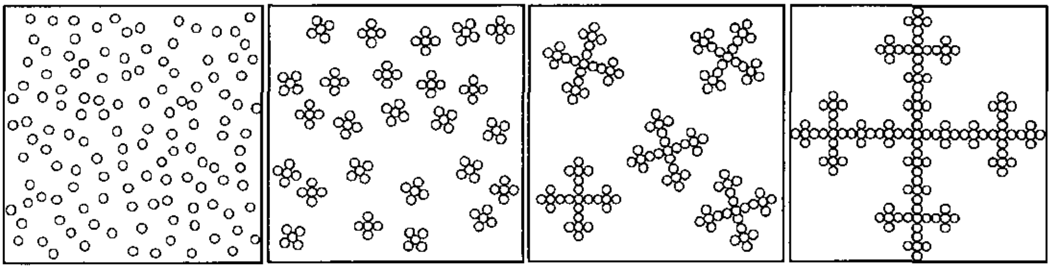

Het doorverbonden netwerk uit het laatste plaatje heeft een gelijkvormige of fractale struktuur. Dit model wordt daarom het fractale model genoemd: het heeft als groot voordeel dat het een duidelijke en kwantitatieve beschrijving geeft van zowel het aggregatieproces als de struktuur van deeltjesgelen.

Aggregatie hoeft niet altijd tot een gel te leiden. De "bouw" van een doorverbonden netwerk zoals beschreven in het fractale model kan misgaan als de deeltjes zó sterk kleven dat ze dikke klonten vormen in plaats van vertakte clusters als in bovenstaande figuur. Om een netwerk bestaande uit dit soort dikke klonten te voltooien is meer "bouwmateriaal" (lees: deeltjes) nodig; als dat niet beschikbaar is komt het netwerk niet af, of wordt het instabiel. In het geval van melk kan deze vorm van aggregatie leiden tot een ophoping van al het bouwmateriaal op de bodem van de beker melk. Men zegt dan dat fasenscheiding heeft plaatsgevonden; de beide "fasen" vloeistof en deeltjes zijn van elkaar gescheiden. Een groter contrast met een gel waarin beide elkaar overeind houden is moeilijk denkbaar.

Aggregatie kan dus leiden tot twee volstrekt verschillende resultaten: een gel of een fasenscheiding. Er bestaat een theorie op het gebied van aggregatie die ons voorrekent dat van deze twee fasenscheiding vaak de meest gunstige toestand is. Dit impliceert dus dat een gel, hoe het zich ook gevormd mag hebben, een tijdelijke constructie is die uiteindelijk wel in een fasenscheiding zal vervallen. De theorie spreekt zich alleen niet uit over hoe lang het duurt voordat "uiteindelijk" bereikt is. Het proces waarin een gel vervalt in fasenscheiding zal altijd een zekere tijd in beslag nemen. Ter vergelijking: er is een algemeen gerespecteerde theorie die voorspelt dat glazen ruiten uiteindelijk uit hun sponningen zullen druipen. De tijdsduur die hiermee gemoeid is loopt echter in de honderden jaren; slechts een enkeling zal zich daar in de praktijk druk om maken. Voor gelen is het belangrijk om te weten hoe, en hoe snel de effekten van fasenscheiding merkbaar beginnen te worden. Het fractale model houdt geen rekening met fasenscheiding en dat zou een tekortkoming van dit model kunnen zijn.

Dit proefschrift

Met welke voorstelling (gel met fractale struktuur, fasenscheiding of iets daar tussenin) een bepaald systeem van geaggregeerde deeltjes het beste overeenkomt, hangt onder meer af van de deeltjesgrootte, de hoeveelheid deeltjes per volume vloeistof en de wisselwerking tussen deeltjes. Dit proefschrift probeert hier een uitspraak over te doen. Eerder onderzoek heeft geleid tot een goede ontwikkeling van het fractale model toegepast op deeltjesgelen. Bijzonder aan dit proefschrift is dat het fractale model wordt gebruikt zonder effekten van fasenscheiding te verwaarlozen. Het houdt zich bezig met het meten van deze effekten uit verschillen tussen door het fractale model voorspelde gelstrukturen en gelstrukturen die in de praktijk gevonden worden. Bij het onderzoeken en kwantitatief maken van gelstrukturen staan twee onderzoeksmethoden centraal: confocale mikroskopie en computersimulaties. Deze worden hieronder toegelicht.

Confocale Mikroskopie

Deze vorm van mikroskopie is in het bijzonder geschikt om de driedimensionale struktuur van deeltjesgelen in kaart te brengen. Door een speciale stand van lenzen in het apparaat is het in staat om nauwkeurig scherp te stellen op instelbare diepte in het gel. De afbeelding die dan zichtbaar wordt laat alleen de deeltjes zien die zich op de ingestelde diepte bevinden, het maakt dus een dwarsdoorsnede van het gel zonder dat het gesneden hoeft te worden. Een stapel van foto's gemaakt op verschillende dieptes vormt de driedimensionale struktuur, althans in principe. Er moet namelijk wel rekening worden gehouden met het feit dat de deeltjes waaruit het gel bestaat, erg klein zijn, vaak kleiner dan wat de mikroskoop zichtbaar kan maken. Dit heeft tot gevolg dat de deeltjes als wazige vlekken op de foto verschijnen, en daardoor veel groter lijken dan ze in werkelijkheid zijn. Op die manier lijkt een gel vaak uit dikkere klonten te bestaan dan in werkelijkheid het geval is. Om de echte struktuur af te leiden uit de "wazige" struktuur moet een bewerking uitgevoerd worden die te vergelijken is met het ontcijferen van een geheimschrift: met de juiste sleutel wordt de boodschap ineens duidelijk. De "sleutel" is in dit geval de manier waarop de mikroskoop het beeld van een deeltje wazig maakt. In dit proefschrift wordt deze "sleutel" uitgerekend; vervolgens worden met wat wiskundige trucs de "wazige" foto's aanmerkelijk opgescherpt, waarna de gelstruktuur beter kan worden bepaald. Voor het inlezen, corrigeren en interpreteren van de stapel foto's, ofwel de beeldverwerking, is in dit promotieonderzoek nieuwe methodologie en programmatuur ontwikkeld. Er waren erg krachtige computers voor nodig.

Computersimulaties

Computersimulaties, zoals gebruikt in dit onderzoek, maken het mogelijk om een bepaalde wisselwerking tussen deeltjes in een computer te programmeren, en vervolgens te kijken of er wel het verwachte uitkomt. Met name onverwachte uitkomsten dwingen dan tot herformulering van veronderstelde ideeën. Een voorbeeld van een onverwachte uitkomst is de vorming van dikke klonten, dat tot het idee van fasenscheiding heeft geleid.

Modelsystemen

De metingen die in dit proefschrift beschreven worden zijn niet gedaan aan haargel. Deeltjesgelen zoals ze in het dagelijks leven worden gebruikt, zoals kaas, beton of chocolademelk, zijn om diverse redenen niet geschikt voor onderzoek met confocale mikroskopie. In dit proefschrift zijn drie soorten speciaal voor dit onderzoek geschikte deeltjes gebruikt, ook wel modelsystemen genoemd. De gebruikte modelsystemen zijn: kleine oliedruppeltjes in water (een emulsie), teflon bolletjes in water en kaaseiwit-bolletjes in water. De eerste twee modelsystemen zijn in dit promotieonderzoek ontwikkeld. Goede modelsystemen voor onderzoek zoals beschreven in dit proefschrift zijn schaars, daarom is deze ontwikkeling een nuttige bijdrage voor verder onderzoek.

Resultaten

In de computersimulaties is duidelijk te zien dat wisselwerking tussen de deeltjes zowel leidt tot groei van clusters (zoals voorspeld in het fractale model), als tot vorming van dikke klonten (fasenscheiding). Als er een gel is gevormd, stopt de groei van clusters - alles zit immers aan elkaar vast - maar de vorming van dikke klonten gaat door. Uit de simulaties volgt een betere voorstelling, zowel van de aard als van de snelheid van fasenscheiding in een gel. Dit heeft geleid tot een aanpassing van het fractale model en een begrijpelijker samenhang tussen gelstruktuur en de wisselwerking tussen deeltjes. Het blijkt dat fasenscheiding soms gelering kan voorkomen, dat altijd na gelering de structuur nog aanzienlijk verandert, en dat soms zelfs het gel weer kan "instorten". Al deze ingewikkelde verschijnselen waren al wel in experimenten gezien, maar de computersimulaties laten zien dat er mogelijk een eenvoudige verklaring aan ten grondslag ligt.

Voor de deeltjesgelen die bestudeerd zijn met de confocale mikroskoop waren deze effekten ook merkbaar en meetbaar, alleen was hier de samenhang tussen struktuur en wisselwerking aanmerkelijk moeilijker te duiden, vooral omdat die wisselwerking niet goed bekend is. Een vergelijking van de resultaten uit computersimulaties en mikroskopie geeft wel aanleiding tot suggesties over welk soort wisselwerking tot de waargenomen structuren in de modelsystemen zou kunnen leiden.

Voor confocale mikroskopie is de ontwikkeling van methodologie en programmatuur even belangrijk geweest als de uitkomsten ervan. Wanneer onderzoekers verder werken aan deze methodologie en kunnen beschikken over krachtiger computers voor beeldverwerking, zullen in dit proefschrift onbeantwoord gebleven vragen kunnen worden beantwoord.

De toekomst

Dit werk heeft geleid tot een aantal nieuwe kanttekeningen bij fractale modellen. Overname hiervan zal de toepasbaarheid van deze modellen uitbreiden tot meer ingewikkelde, dus meer interessante gevallen van aggregatie. Er is nog veel nieuw onderzoek te doen aan deeltjesgelen; de rek is er nog lang niet uit.

Levensloop

Martin Thomas Alexander Bos werd geboren op 11 maart 1967 te Utrecht. In 1985 behaalde hij het diploma ongedeeld VWO aan de "Werkplaats Kindergemeenschap" te Bilthoven, waarna hij een studie scheikunde aan de Universiteit Utrecht begon. In 1991 studeerde hij af. De doctoraalstudie omvatte de afstudeervakken kristallografie, moleculaire mechanica en colloïdchemie.

Tussen september 1991 en mei 1996 was hij werkzaam als Assistent in Opleiding bij de vakgroep Fysische- en Kolloïdchemie aan de Landbouwuniversiteit Wageningen. Hieruit is dit proefschrift voortgekomen.

Sinds juni 1996 is hij werkzaam bij Unilever Research in Port Sunlight, Merseyside, Groot Brittannië.

Nawoord

De tijd waarin dit proefschrift tot stand gekomen is, is voor mij een bijzondere geweest. Ik heb de gelegenheid gekregen om een intensief leerproces te mogen doorlopen en daar heb ik meer van opgestoken dan hetgene waarover in dit boekje wordt geschreven. Veel heb ik daarbij aan anderen te danken, waarvoor ik hen in dit gedeelte mijn dank wil betuigen.

Mijn promotoren, Bert Bijsterbosch en Pieter Walstra, bedankt voor jullie intensieve begeleiding, die me veel inspiratie en richting heeft gegeven. Jullie zorgvuldig schaafwerk aan de vele versies van dit proefschrift heeft me uit vele linguistische en wetenschappelijke valkuilen gered. Bert, met plezier denk ik terug aan onze discussies over de wiskundige achtergonden van dit proefschrift. Ook al beweerde je telkens dat je hier geen expert in was, jouw kritische ondervragingen dwongen me wel na te denken over de betekenis van al die formules. Dat heeft tot belangrijke doorbraken geleid, zoals bijvoorbeeld de betekenis van de voorfactor in fractale schalingswetten. Allebei hebben jullie me de vrijheid gegeven om me naast experimenten ook met simulaties en theorie bezig te houden. Het kostte extra moeite om dat allemaal te combineren in één onderzoek, maar voor mij is het die moeite dubbel en dwars waard geweest.
De maandelijkse bijeenkomsten van het "plenum" (Bert, Pieter, Joost van Opheusden, Ton van Vliet en ik) waren altijd spannend en dynamisch. Er is wetenschappelijk enorm veel overhoop gehaald en dat was een verrijkende ervaring. Ton, bedankt voor jouw bijdrage in deze discussies en voor je correcties op artikelen en hoofdstukken.
Beste Joost, jouw toetreden tot het "plenum" heeft ontzettend veel bijgedragen aan de kwaliteit van dit onderzoek en niet minder aan mijn eigen ontwikkeling. In jouw genuanceerde en heldere kijk op dit onderzoek heb je barrières tussen schijnbaar onverenigbare theorieën weggenomen, evenals barrières tussen "experimentalisten", "theoreten" en "simulanten". Je bent mijn mentor geworden en hebt me intensief en vooral opbouwend begeleid in het schrijven. Met veel plezier denk ik terug aan discussies over clusters, stijgende multifractale spectra, het expanderende heelal en het opvoeden van kinderen.

Op de vakgroep Fysische- en Kolloïdchemie hebben slechts weinigen mij zien werken aan de experimenten die toch wel degelijk in mijn proefschrift vermeld staan. Dat heeft de volgende oorzaak. Toen ik ongeveer een jaar bezig was, werd duidelijk dat de confocale mikroskoop, waarvan ik tot op dat moment gebruik had gemaakt, wegens reorganisatie naar Lelystad werd verplaatst. Medewerkers van de vakgroep Plantencytologie en -Morfologie hebben mij uit deze moeilijke situatie gered door mij hun mikroskoop te laten gebruiken. Alle mikroskoopfoto's in dit proefschrift zijn daar genomen en ik heb er met veel plezier gewerkt. Ik zou met name Wim van Veenendaal, Norbert de Ruijter, André van Lammeren en Jaques van Went hartelijk willen danken, alsmede degenen die mij op 5 december 1995 in de mikroskoopkamer trakteerden op bisschopswijn en pepernoten, precies waar ik op dat moment behoefte aan had.

De grote groep mensen die samen de Vakgroep Fysische- en Kolloïdchemie vormt ben ik veel dank verschuldigd. Het was een voorrecht om aan deze vakgroep te mogen werken, ik heb vier jaar dicht bij een wetenschappelijk, maar ook een sociaal vuur gezeten. Beste FysKo'ers, jullie hebben voor dit boekje, maar ook voor mijzelf veel betekend. Op veel gebieden hebben jullie me ondersteund. Jullie hebben me geholpen aan voor onderzoek onontbeerlijke dingen als koffie, drop, chemicaliën, glaswerk, computers, bier, papier, spuitflessen en pluche dieren. Met veel genoegen heb ik met jullie gediscussieerd over het leven, de wetenschap en de zoutsterkte van de soep in de kantine. De sfeer werd gekenmerkt door gezelligheid, humor en relativering; zowel promotieplechtigheden als conferenties waren sociale evenementen. Mijn werkplek op FysKo, de experimentele zitkamer k021, heb ik met veel plezier gedeeld met Ronald, Katinka en Jacomien. Beste kamergenoten, jullie maakten het daar tot een bruisende sfeer waarvan ik heb genoten, en die veel tegenwicht bood aan de introverte kanten van het onderzoek. Fysko'ers, bedankt voor jullie gezelschap!

De personen die het meeste tot dit proefschrift hebben bijgedragen zijn de mensen die ervoor gezorgd hebben dat ik dat proefschrift schrijven kon. Hierom bedank ik mijn ouders, die me hebben laten studeren en die me altijd gestimuleerd hebben om alles te onderzoeken en het goede te behouden. Vrienden en familie hebben met me meegeleefd, wat een grote steun was. Jullie vormden voor mij de wereld die tijdens het werken aan een proefschrift gewoon doordraaide. Zonder jullie had ik veel van die wereld gemist en dan had ik de wetenschappelijke wereld ook niet aangekund.
Hanneke, mijn levensgezellin, jou wil ik bedanken voor het in alle facetten willen delen van mijn promoveren. Samen hebben we over elke denkstap en elk voorval tijdens mijn promotie van gedachten kunnen wisselen. Je hebt mijn enthousiasme aangewakkerd en me moed ingeblazen als ik uitgeblust was. Het boekje is ook jouw boekje geworden, het einde van een lange klus en het gelegenheid om te feesten!